Supernova Rates, Rise-Times, and their Relations to Progenitors

by

Santiago González Gaitán

A thesis submitted in conformity with the requirements
for the degree of Doctor of Philosophy

Graduate Department of Astronomy and Astrophysics
University of Toronto

Abstract

Supernova Rates, Rise-Times, and their Relations to Progenitors

Santiago González Gaitán
Doctor of Philosophy
Graduate Department of Astronomy and Astrophysics
University of Toronto
2011

Supernovae are fundamental in astronomy: they inject high mass elements into the interstellar medium enriching the chemistry of galaxies, they feed processes of star formation and active galactic nuclei, and they have been a key for the developments in cosmology of the past decades.

This dissertation presents a set of subluminous type Ia supernovae (SNe Ia) at $z > 0.1$ from the Supernova Legacy Survey (SNLS). These faint and short-lived transients are found in massive and passive host galaxies. We measure a volumetric rate as a function of redshift that is different from the normal SN Ia population. The observations point towards a long delay time since the birth of the progenitors systems and argue for progenitor stars of initial low mass.

We calculate a stretch-corrected rise-time since explosion to maximum brightness for different sets of SNe Ia. We find that a fiducial 17 day quadratic rise is sufficient to explain all SNe Ia, including subluminous ones, arguing for their homogeneity throughout the entire light-curve. Subluminous SNe Ia are powered by as little as 0.05 $\mathrm{M}_{\odot}$of ^{56}Ni synthesized in the explosion. Theoretical models need to explain these challenging weak explosions within the framework of SNe Ia.

Finally, we develop one of the first robust automated techniques to identify plateau supernovae (SNe IIP) in large photometric transient surveys. This simple method was tested with a variety of real and simulated SN samples and proved to be effective across different redshifts. Such a photometric typing will be of great power for coming surveys and will allow numerous scientific studies of SNe IIP.

Acknowledgements

I am very thankful to my supervisor, Ray Carlberg, for a healthy work balance, providing support when needed but also trust and freedom to advance as a scientist and allowing me to keep priorities in place. To the Toronto-based SNLS collaboration, Alex, Mark, Kathy and Andy, I am extremely grateful for your incredible help, patience and advice, but especially for your coolness. I thank the whole SNLS team for making this survey a success and this thesis possible. To Dae-Sik Moon, Marten van Kerkwijk and Bob Abraham for very helpful discussions and tips, and to Brian Schmidt for insightful comments that improved this thesis. I thank Andrea Pastorello for the use of unpublishded supernova data.

I would like to thank the constant support of my family, particularly my mother, and of the Toronto family, i. e. all my friends: you are the ones that make life a happy adventure! Almost no et al.'s here: Dani, Erinilla, Pollote, Nixon, Sherrylein, Zaki, Marcoño, Pookie, Vietta, Marija, Preethi, Nandao, Bananne, Majid, Azin, Harui, Laura, Ricardinho and Yu-Min, Justin and Johanna, Fedex, Cata y Caja, Kai, Lauretta, Benkelein, Patrick, Kev, Ivana, Saša, Kora, Mariangela, Fer (special thanks for super useful discussions!), Moni y Sebas, Fermín y Ana, Iñigo, Alexis, Aleks, Pooh, Benito y Caterina, Tomek, Oliver C., Jeanine, Tony, Lucie et Mika, Renbin, Summer and Willy, Mikhael and Tracey, Bindo, Alex, Darrell, Mimi, and many more... (et. al., after all).

At last, I thank all the great beings working for a better tomorrow. They remind me of what is important and all that remains to be done. To God.

Contents

List of Tables

List of Figures

Chapter 1

Introduction

Supernovae are among the brightest objects in the universe. In AD 1054, Chinese and Arab astronomers discovered a "new star" that was more luminous than other ones for a period of several months to later fade back out of sight to what today is known as the Crab nebula. Other such historical supernovae include Tycho Brahe's discovery in 1572 in Cassiopeia and Johannes Kepler's 1604 observation in the constellation Ophiuchus.

The advent of photographic plates in the last century, CCDs[1] and especially big CCD cameras more recently, enabled more discoveries of such objects. When Edwin Hubble's studies in the 1920's led to the recognition that spiral nebulae were huge stellar agglomerations outside of our own galaxy, the new objects known as "novae", that were found to explode within them, had to be further away and more luminous than previously thought. They were given the name of "supernovae" (SNe, hereafter) by Baade & Zwicky (1934). Since then many SNe have been discovered and observed.

Supernovae are the final stages of some stars, big explosions releasing enormous quantities of energy capable of outshining the entire host galaxy. After the initial rapid material ejection, a supernova remnant develops consisting of an expanding shock wave that interacts with the interstellar medium and enriches it with heavier elements formed in the original star and during the explosion. Supernovae are essential to understand the life cycle of stars and the chemical enrichment of galaxies. Their use as extragalactic distance estimators makes them a fundamental tool for cosmological studies of our universe.

1.1 SN classification

Minkowski (1941) recognized that SNe fall into two main categories based on their spectral

[1] A Charged Coupled Device or CCD allows electrical charge from a photoelectric device to be transformed into a digital signal

characteristics: Type I with broad emission lines but no hydrogen (H) lines, and Type II consisting of strong H emission lines. In the 1980's, further early time spectroscopy and the construction of synthetic spectra providing better line identification, together with the study of the optical lightcurve evolution led to further sub-classifications recognized today:

Table 1.1: Supernova classification

Type		Observed Characteristics
I	Ia	No hydrogen, and srong presence of ionized silicon
	Ibc { Ib	No hydrogen, no silicon and abundant helium
	Ibc { Ic	No hydrogen, no silicon, no or very weak helium
II	IIP	Long lightcurve "plateau" of nearly constant luminosity after maximum
	IIL	Linear lightcurve decrease in luminosity after maximum
	IIb	Similar photometric behavior to SNe Ibc but with hydrogen in the spectra early after explosion, and late helium lines as SNe Ib
	IIn	Slowly declining lightcurves and no broad P-Cygni profiles* but narrow emission lines

*The P-Cygni profile contains strong emission lines and blueshifted absorption lines, and is characteristic of an expanding shell.

This simplified table shows the general observational classification scheme for SNe. However, a variety of peculiar objects have been found that cannot be unambiguously placed in a particular category. The family of SNe IIb represents a clear case where the characteristics of different SNe overlap, namely the early type II behavior followed by a type Ib transition. Furthermore, some particular objects such as SN1997cy, SN2002ic (Hamuy et al. 2003) or SN2005gj (Aldering et al. 2006), seem to be transitional objects between clearly distinct physical categories (see next section), SNe Ia and H-rich type IIn SNe. The picture of SNe with the different subtypes is evolving and will improve substantially with current and future technologies in transient searches. Fainter and rarer unknown explosions are being discovered (e. g. Prieto et al. 2009; Kawabata et al. 2010; Poznanski et al. 2010; Kasliwal et al. 2010), expanding the sample and testing our understanding of SNe and their physics.

Table 1.1 summarizes the most studied SN categories, but it does not directly reveal any information about their nature. As early as 1934, (Baade & Zwicky 1934) suggested that SNe came from ordinary stars collapsing into neutron stars, although Type Ia could not fall into this description. Found in star forming environments, it is currently believed that Type II and Type Ibc all come from the collapse of the core of massive young stars at the end of their lives (see section 1.3 and Burrows 2000; Woosley & Bloom 2006; Smartt 2009 for a review). Type Ia, on the other hand, can be found in old stellar populations and their lack of H suggest that they

come from lower-mass stars that turn into white dwarfs (WDs). These WDs, if in binaries, can accrete mass that can lead to an explosive thermonuclear runaway (see section 1.2 and Howell 2010 for a review).

1.2 Supernovae Type Ia

1.2.1 Observational characteristics

In the past decade, SNe Ia have become a favorite topic of research since they were used as standardized candles to reveal the existence of an energy component of the universe determining its evolution (Riess et al. 1998; Perlmutter et al. 1999).

SNe Ia are extremely bright, i. e. $M \sim -19.5$, and have very homogenous lightcurve properties. Phillips (1993) showed that the luminosity at peak was directly related to the lightcurve shape, i. e. brighter SNe Ia decline more slowly and fainter SNe Ia evolve faster (see Figure 1.1). Brighter SNe Ia are also bluer at peak than their fainter counterpart (Riess et al. 1996; Tripp 1998). The spectra of SNe Ia lack H and He lines but have abundant intermediate mass elements (elements from Si to Ca) like Si II, S II, O I and Ca II (and sometimes C and O) and at later times in their evolution, they develop metal lines, like Fe and Co. Finally at nebular phases, they show [Fe II] and [Fe III].

Despite forming quite a continuous set, several peculiar objects with considerable differences have been found in the past. On the bright extreme, there is the group of slow declining objects similar to SN1991T (Filippenko et al. 1992a; Ruiz-Lapuente et al. 1992; Phillips et al. 1992; Jeffery et al. 1992; Spyromilio et al. 1992). On the faint end, the group of intrinsically red and fast decliners like SN1991bg (Leibundgut et al. 1993; Filippenko et al. 1992b; Turatto et al. 1996) have strong Ti II and enhanced Si II lines in their spectra. Other atypical SNe Ia consist of SN2000cx (Li et al. 2001b; Candia et al. 2003) and SN2002cx-like objects (Li et al. 2003), similar in the pre-maximum spectra to SN1991T but evolving fast, and as faint as SN1991bg.

SNe Ia are found in every type of galaxy, in spirals and ellipticals, and are therefore not uniquely associated with star forming regions. Interestingly, the stellar environment of SNe Ia is related to their intrinsic properties. Bright and slow decliners occur in regions associated with star formation, where they are more common (Mannucci et al. 2005; Sullivan et al. 2006b), while fainter and faster SNe Ia prefer passive or elliptical host galaxies (Hamuy et al. 1995, 1996c; Riess et al. 1999a; Hamuy et al. 2000; Sullivan et al. 2006b; Aubourg et al. 2008). These environmental effects are reproduced in the spectra as well: SNe Ia in late-type galaxies show weaker lines of intermediate mass elements than in early-type galaxies (Bronder et al. 2008; Balland et al. 2009; Sullivan et al. 2009). Studies of the metallicity environment of SN Ia reveals

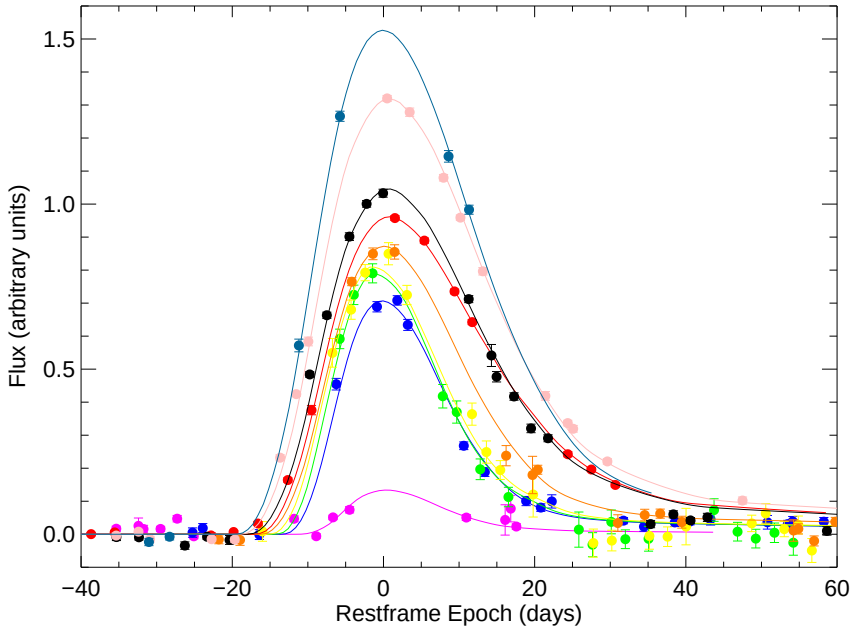

Figure 1.1: r_M-band lightcurves of 8 SNe Ia from the Supernova Legacy Survey with different lightcurve-widths (stretches in the range $0.65 < s < 1.2$). The epochs are corrected to restframe for each respective redshift and the fluxes are normalized relative to the absolute restframe peak magnitude of a $s = 1$ SN Ia. The best SiFTO (Conley et al. 2008) fit for each SN is shown in solid lines.

a much weaker relation with SN properties than the stellar age (Gallagher et al. 2008; Howell et al. 2009).

As will be shown in next section, different progenitor scenarios predict different delay times from the birth of the binary system to the explosion of a SN Ia. Exploring the delay time distribution (DTD) of SNe Ia helps constraining progenitors. This has been done comparing the SN Ia birthrate to the cosmic star formation (e. g. Gal-Yam & Maoz 2004; Strolger et al. 2004; Scannapieco & Bildsten 2005; Mannucci et al. 2006; Pritchet et al. 2008; Maoz et al. 2011), or directly constructing it from the age of the stellar populations through detailed host galaxy photometry and spectroscopy (Totani et al. 2008). Furthermore, as SNe Ia are a source of iron-peak elements[2] into the intergalactic medium, the SN Ia birthrate is related to the cluster iron abundance (e. g. Matteucci et al. 2006) and the latter can be used as an additional constraint to normalize DTDs (Maoz et al. 2010). The latest DTD results, including estimates from the rate of SN Ia remnants (Maoz & Badenes 2010), are converging to a power-law DTD that scales inversely with cosmic time, t^{-1}.

[2]Elements and isotopes close to the iron nuclear binding energy peak: vanadium, chromium, manganese, iron, cobalt, and nickel

1.2.2 Explosion and Progenitor scenarios

Due to their occurrence in every galaxy –particularly in old stellar populations– and the absence of hydrogen and helium in their spectra, SNe Ia are believed to originate from long-lived low-mass stars, $M_{\rm ZAMS} < 8{\rm M}_{\odot}$[3], that end up their lives as carbon-oxygen white dwarfs (CO-WDs), with a mass distribution peaking at $M \simeq 0.6 M_{\odot}$, well below the Chandrasekhar limit[4]. If they happen to be in a binary system, where mass can be accreted into the WD nearing the Chandrasekhar limit or causing enough compressional heating, then the C/O material can be ignited. As the WD is degenerate, this burning becomes explosive and rapidly disrupts the entire star. Iron-peak and intermediate-mass elements synthesized in the process are ejected at high velocities to space and no compact remnant is left behind. The kinetic energy of a SN Ia is approximately equal to the difference of the thermonuclear burning of a WD and its binding energy.

The lightcurve of a SN Ia is powered by the radioactive beta decay of ^{56}Ni to ^{56}Co and then to ^{56}Fe (Truran et al. 1967; Colgate & McKee 1969; Arnett 1982), which releases large quantities of gamma rays thermalized to the optical regime. At peak, most of the light is in the visible and some in the near-ultraviolet (NUV) and near-infrared (NIR). The rise to peak lasts 10-24 days depending on the SN Ia and, once the radioactive energy released equals the radiated luminosity, the luminosity starts decreasing. Due to a long diffusion time of photons, at early times the outer layers of the SN are seen, while the inner products of the explosion appear in the spectra later in time, as the photosphere recedes. Near peak, the spectra show P-Cygni profiles, weeks later they show scattering lines, and finally emission lines in the nebular phase[5], as the photosphere becomes optically thin (Branch et al. 2006). Much later (hundreds of days), gamma rays from the decay of ^{56}Co can freely escape and the lightcurve slope resembles the radioactive decay, as long as positrons are trapped (Lair et al. 2006), and spectral lines show iron-peak elements from the innermost parts of the explosion.

Although consensus exists on the general features, the exact details of the WD progenitor, especially the companion, as well as the detailed physics of the explosion are subject to vigorous debate. The theoretical models need to explain the abundant observations of SNe Ia and the relations binding these together. Currently, three main progenitor scenarios are discussed:

Single Degenerate: The single degenerate (SD) scenario, a favored scenario in the past, suggests an evolved or main sequence companion (Whelan & Iben 1973) donating material

[3]The zero age main sequence mass, $M_{\rm ZAMS}$ refers to the mass of a star at the onset of H core fusion in the main sequence

[4]The Chandrasekhar limit (Chandrasekhar 1931) refers to the maximum mass above which a white dwarf's electron degeneracy pressure is unable to sustain the self-gravity of the star. It is close to 1.4M$_{\odot}$.

[5]The nebular phase occurs when the ejecta is optically thin to continuum photons. These come from converted gamma rays of ^{56}Co decay and are seen as emission lines in the spectra

to the WD nearing the Chandrasekhar limit. The rate of the accretion needs to be steady, between $10^{-7} - 10^{-8} \mathrm{M}_{\odot} \mathrm{yr}^{-1}$ (Nomoto 1982) to avoid novae and mass loss (slower accretion), or expansion into a giant envelope (higher accretion). The most viable candidates of such binary systems are supersoft X-ray sources (Rappaport et al. 1994), although their observed rate in the Milky Way and other galaxies seem to account for only $\sim 5\%$ of the SN Ia rate (Di Stefano 2010a; Gilfanov & Bogdán 2010).

The main argument against the accretion from a non-degenerate companion is the lack of hydrogen seen in SNe Ia (Leonard 2007). The outer layers of the companion during Roche lobe overflow are stripped and become part of the SN ejecta, making them visible. Symbiotic channels (e. g. Hachisu et al. 1996), where the WD accretes mass from the stellar wind of the companion, try to bypass this issue, but the absence of radio signatures for SNe Ia sets a limit of steady mass loss prior to the SN that disfavors such mechanisms (Panagia et al. 2006).

Moreover, the occurrence of super-Chandrasekhar SNe Ia, explosions that seem to require WDs of masses exceeding the Chandrasekhar limit (e. g. Howell et al. 2006; Hicken et al. 2007; Scalzo et al. 2010; Yuan et al. 2010), are also at odds with the slow accretion near M_{Ch} required by the SD scenario (although see Hachisu et al. 2011).

Additionally, although the number of WDs in close binaries with non-degenerate companions is sufficient to explain the SN Ia birthrate, the predicted DTDs (Yungelson & Livio 2000; Greggio 2005; Mennekens et al. 2010) do not agree with the recent empirical DTDs (Totani et al. 2008; Maoz et al. 2010; Graur et al. 2011), i. e. they do not have a power-law with steeper index than -1.

Furthermore, a red giant companion as the main channel is currently disfavored as recent well sampled early lightcurves (Hayden et al. 2010a; Bianco et al. 2011) do not show any evidence for a hole left by the companion in the early-time supernova ejecta (Kasen 2010).

Some of these criticisms, like lack of H and no signature of a companion during the rise, have been addressed with more exotic SD theories, like the scenario proposed by Justham (2011), where the WD gains angular momentum that stabilizes it and prevents ignition until the H-rich envelope of the donor is exhausted and contracts, leaving the WD in a wide orbit binary before explosion.

Double Degenerate: The double degenerate (DD) scenario consists of two CO-WDs that merge together to reach the Chandrasekhar mass (Iben & Tutukov 1984; Webbink 1984). An accretion disk from the disrupted WD forms around the more massive primary and carbon is ignited on the surface.

One of the main drawbacks of the DD scenario is that such a burning is non-explosive and will lead to a ONe-WD that ultimately collapses to a neutron star (Saio & Nomoto 1985), although this might be prevented under some assumptions (Yoon et al. 2007). Current models of WD mergers are able to produce only subluminous SNe Ia (Pakmor et al. 2010) and more three-dimensional simulations need to investigate this intricate process further. The DD scenario also suffers from a lower observed rate of X-ray emission in nearby galaxies compared to predictions of supersoft X-ray binaries, supposed transition states of DD progenitors (Di Stefano 2010b), but this discrepancy is lower than for the SD scenario.

On the other hand, the DD channel naturally explains the absence of H, it agrees well with the empirical relative DTDs obtained from the SN Ia birthrates (Totani et al. 2008; Maoz et al. 2011; Graur et al. 2011), it satisfies the non-observation of a companion signature in early rise-time studies, and it can also better account for super-Chandrasekhar SNe Ia from the merger of two WDs whose total mass exceeds the limit.

Additionally, in this framework, the relation between SN Ia properties and stellar environments seems naturally explained: brighter SNe Ia occur in younger populations where more massive WDs merge, whereas fainter SNe Ia come from less massive WD progenitors, characteristic of older populations.

The only observational weakness is that the predicted rate (or absolute DTDs) is higher than the observed one (Maoz et al. 2010), that is, there are not enough WD binary systems exceeding the Chandrasekhar limit.

Sub-Chandrasekhar: Explosions of WDs below the Chandrasekhar mass have recently been revived. In the previous two scenarios, the WD explodes near the Chandrasekhar mass. Such an explosion cannot be explained by a pure detonation[6] since the high density of the burning produces too many iron-peak elements and few intermediate mass elements (Arnett 1969). A pure deflagration[7], on the other hand, cannot account for the high velocities of the outer ejecta (Mazzali et al. 2005). The favored mechanism is therefore a transitional combustion starting with a subsonic deflagration leading to a supersonic detonation (Khokhlov 1991). The physics of the transition are not well understood but the lightcurve, spectra, and lightcurve width-luminosity relation of SNe Ia are well recreated (Kasen et al. 2009).

Instead of adding a somewhat unnatural deflagration-to-detonation transition, a sub-Chandrasekhar detonation of a WD with lower mass and density can naturally produce

[6] A detonation is a supersonic combustion propagating through shock compression
[7] A deflagration is a subsonic combustion propagating though the transfer of thermal energy

the right mix of iron peak and intermediate mass elements. Furthermore, it could also explain the lower empirical ejecta masses of some SNe Ia (Stritzinger et al. 2006). Simulations (Sim et al. 2010) show that the detonations of sub-Chandrasekhar mass WDs can reproduce lightcurves and spectra of SNe Ia.

The problem lies in the right trigger for carbon ignition. The original models (Woosley & Weaver 1986) had an initial layer of accreted helium detonating and creating a shock wave towards the core of the WD that would generate a second detonation propagating outwards and disrupting the WD. These models were rejected because of the large amount of ^{56}Ni generated in the early portion of the lightcurve from the He-burning, which is inconsistent with observations (Nugent et al. 1997). Nowadays. indications exist that He can detonate in a much thinner layer (Shen et al. 2010), allowing the possibility for such a double detonation. This channel requires further theoretical development to explore if it can confirm diverse aspects of SNe Ia observables.

Of particular interest in sub-Chandrasekhar models are the merger of CO-WDs below the Chandrasekhar limit. All the benefits of the DD scenario, such as the lack of H, the relative DTD and the early rise time behavior, are inherited. Additionally, the proper fraction of binary systems leading to explosions, and with it the absolute DTD, are obtained, since lower-mass WDs, which are more frequent, can merge and explode as SNe Ia. However, Lorén-Aguilar et al. (2009) and Pakmor et al. (2010) show that the merger of two CO-WDs of equal mass below $\sim 0.9\mathrm{M}_{\odot}$ are not hot enough to ignite C in the core. Moreover, due to the low central density of the WD, the only successful explosions that are achieved are subluminous ones. Ideas to circumvent this are compressional heating from a thick accretion disk around the rotating WD after the merger (van Kerkwijk et al. 2010), although full simulations are required to test the viability of this channel. If some sort of heating mechanism extends over all WD mass ranges, super-Chandrasekhar models could also be explained, as in the regular DD scenario.

The last years of SN Ia science has led to a shift in the favored progenitor channel away from the SD scenario. The DD channel and the recently revived sub-Chandrasekhar models are promising candidates, although clearly more extensive multi-dimensional simulations are required to test how feasible they are. Evidently, SNe Ia can originate via multiple channels, and the different scenarios could each play a contributing role.

1.2.3 SNe Ia as distance indicators

Correcting for the empirical relations of lightcurve width-luminosity and color-luminosity makes SNe Ia good standard candles, providing direct evidence for an unknown dark energy

driving the accelerated expansion of the universe (Riess et al. 1998; Perlmutter et al. 1999). Additional relations with luminosity have been searched for to further improve SNe Ia as distance rulers. A third parameter has recently been introduced relating luminosity to host environment, i. e. brighter SNe Ia occur in more massive host galaxies (Sullivan et al. 2010; Kelly et al. 2010; Lampeitl et al. 2010). Other possible corrections include metallicity (e. g. Timmes et al. 2003; Gallagher et al. 2005; Howell et al. 2009; Yasuda & Fukugita 2010), spectral features such as high-velocity lines (Wang et al. 2009a) or flux ratios (Bailey et al. 2009; Yu et al. 2009).

Current SN Ia cosmological studies (e. g. Kessler et al. 2009; Conley et al. 2011) (see Figure 1.2) have reached a mature state where the systematic uncertainties are comparable to statistical uncertainties directly affecting the measurement of the dark energy's equation of state, w. The present and future challenges of supernova cosmology thus reside in understanding and diminishing those systematic biases. Here is a brief summary of those (for a more complete description, see Conley et al. 2011).

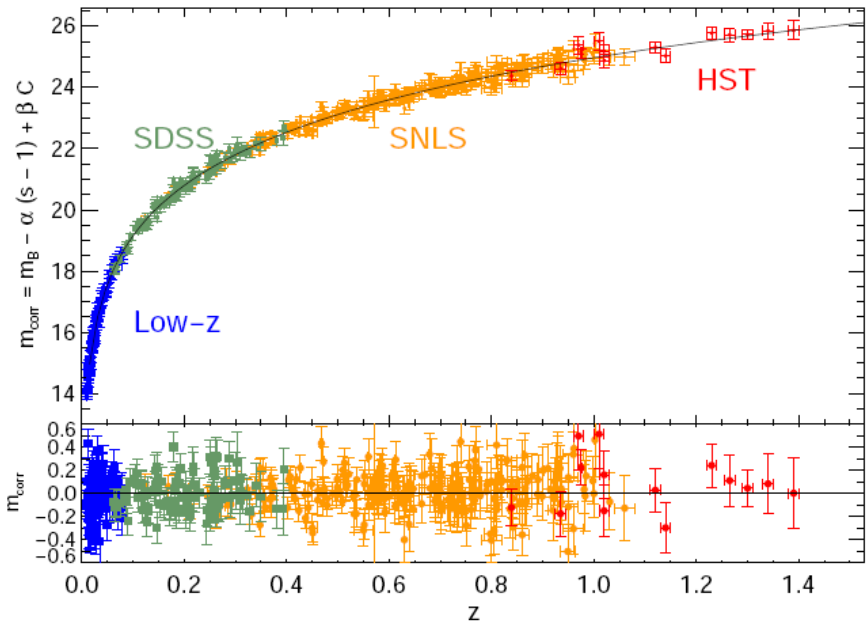

Figure 1.2: Hubble diagram of combined SNe from different samples (low-z, SDSS, SNLS and HST). The bottom plot shows the residuals from the best fit for a falt universe: $\Omega_m = 0.18 \pm 0.10$ and $w = -0.91^{+0.17}_{-0.24}$. *From Conley et al. (2011)*

Calibration: The current most important systematic by far is the calibration across SN samples at different redshifts. As SNe at higher-z are redshifted and other bandpass filter are used, different samples need to be converted to a common standard photometric system, and relative fluxes need to be calculated. This permits the direct comparison of

SNe at different redshifts. Most of the low-z dataset is currently on the Landolt system (Landolt 1992), which is not well understood. Thus, the calibration systematic will be substantially reduced once different high-z SN samples are cross calibrated to the low-z SN sample, or new low-z data in better understood systems become available (like the SNfactory –Bailey et al. 2009, CSP –Folatelli et al. 2010 and more SDSS-II –Kessler et al. 2009).

Lightcurve-fitter: Another smaller systematic arises from the fitter used to parameterize the SN lightcurve shape, that serves later to correct each SN's luminosity. There are clear differences in the SN color treatment of fitters like SALT2 (Guy et al. 2007) and SiFTO (Conley et al. 2008) versus fitters like MLCS2k2 (Jha et al. 2007). Particularly, fitters trained with low-z data exclusively, like MLCS2k2, suffer from missing rest-frame U-band data which becomes important at high-z, where redshifted SNe are probed in that wavelength regime. Differences from various fitters represent another relevant systematic contributing to SN cosmology (Guy et al. 2010).

Reddening: An important systematic and elusive concern in SN Ia cosmology has been the color/dust degeneracy. Corrected for in the color-luminosity relation entering the residuals of the Hubble diagram, the SN color has been difficult to disentangle from dust in the line of sight. The reddening law inferred from SNe is significantly different from the Milky Way dust (lower R_V[8]). This may be due to the mix of intrinsic SN reddening and dust, or alternatively it can be caused by a different dust in the line of sight to SNe Ia or scattering effects from circumstellar material (Wang 2005; Goobar 2008).

Local NIR observations benefit from less sensitivity to dust and help characterize the intrinsic colors of SNe Ia. Although with low statistics, using ratios of color excesses in the optical and NIR, Folatelli et al. (2010) find an indication that low-extincted SNe Ia have a reddening law like the Milky Way's, while redder objects follow a different one (lower R_V). Furthermore, spectral studies show that SNe Ia of different velocity gradients may have varying colors and R_V (Pignata et al. 2008; Wang et al. 2009a). This would mean that there is an intrinsic color variation of SNe Ia that correlates with luminosity but independent of the SN properties, such as lightcurve-shape. This could imply different progenitor scenarios leading to SNe of different velocities and different color properties. Observations of the correlation of the late nebular emission lines with SN color suggest that this diversity of SNe Ia could come from varying observing angles of asymmetric explosions (Maeda et al. 2011).

[8] R_V is a parameter describing the extinction curve of interstellar dust and is defined as A_V/E_{B-V}, with $E_{B-V} = A_B - A_V$, where A_B and A_V are the total extinctions in B and V bands.

In the latter cases, the need for a separate correction for intrinsic SN color and dust reddening for cosmological studies seems necessary. Some attempts to account for this have been made (Sullivan et al. 2010; Lampeitl et al. 2010) by dividing the SN set according to their host properties, like star formation, and applying an independent reddening correction for each subset. Such exercises reveal differences in the reddening laws: a lower R_V is found for hosts with lower star formation.

Finally, in contrast to the traditional B-band Hubble diagrams, the restframe IR Hubble diagrams (Krisciunas et al. 2004a; Wood-Vasey et al. 2008; Freedman et al. 2009) offer an interesting new approach to cosmology with SNe Ia that has less reddening bias and a tighter dispersion, even without a lightcurve shape correction.

Evolution: A long lasting concern for cosmology resides in the possible evolution of SNe Ia and SN Ia populations as a function of cosmic time. This is an extremely important matter that suffers from a poor understanding of the physics of the progenitors and explosions of SNe Ia. The evolution of the demographics of SNe Ia is a known effect seen to $z \simeq 1$ (Howell et al. 2007). Since brighter SNe Ia occur only in late-type galaxies whereas fainter ones are found in both, elliptical and spiral galaxies, the population of SNe Ia observed at different lookback times will change as the cosmic star formation increases with redshift. This change in population does not affect the cosmological studies since SNe Ia are corrected for the lightcurve-width relation to the same absolute magnitude. On the other hand, evolutionary changes in this relation itself (through changes in the α parameter) will be of greater concern, but studies show no conclusive evolution (Guy et al. 2010).

Moreover, claims of an evolving intergalactic gray dust making SNe fainter without reddening them, have stood in opposition to the acceleration of the universe since its proposal (Aguirre 1999) and continue today (Corasaniti 2006; Bogomazov & Tutukov 2011). Regular intergalactic dust evolution (Ménard et al. 2010) has been shown to represent only a small systematic, and reddening evolution remains marginal (studied through changes in the β parameter of the luminosity-color relation) (Guy et al. 2010; Conley et al. 2011), despite some claims (Kessler et al. 2009).

Others: Additional systematic uncertainties affecting cosmological studies to a lesser extent include uncertainties in the Malmquist bias corrections[9]; uncertainties in the Milky Way extinction correction (Schlegel et al. 1998); the adopted local flow model, or nearby peculiar velocities; contamination from non-Ia SNe; and gravitational lensing effects (Holz

[9]The Malmquist bias is a selection bias to preferentially detect brighter objects

& Linder 2005; Jönsson et al. 2010).

1.3 Core-collapse supernovae

1.3.1 Observational characteristics

Core-collapse SNe are a heterogeneous set with different spectral and lightcurve features. SNe of type Ib/c lack hydrogen in their spectra. SNe Ib do not possess Si II lines but have He I, whereas SNe Ic do not show helium either. Both, SNe Ib and SNe Ic, show lines of Ca II, O I, Na I, Fe II, Ti II in photospheric phase and [O I] and [Ca II] in the nebular phase (Millard et al. 1999; Matheson et al. 2001; Branch et al. 2002). SNe Ibc are on average fainter than SNe Ia, i. e. $M_B \sim -18$ at peak with a larger dispersion (Richardson et al. 2002).

SNe II are characterized by the presence of hydrogen lines in their spectra. The observed lightcurve display varies widely. Plateau supernovae (IIP) show a plateau phase after maximum, where the luminosity remains almost constant for 80-150 days. The peak brightness is on average $M_B \sim -17$ with a large dispersion (Richardson et al. 2002). Type II linear SNe (IIL) are brighter than SNe IIP (similar to the brightness of SNe Ibc) and show a steady decline in luminosity after maximum. Narrow-lined SNe (IIn) have dominant narrow emission lines (Schlegel 1990) from interaction of the ejecta with circumstellar material (CSM). They also show He I emission lines, Balmer and Na I absorption lines. The CSM creates inner and outer shocks as the ejecta interacts with it and makes the lightcurve very bright for several years. Variations in the amount and density of the CSM give rise to quite a heterogeneous sample. Finally, SNe IIb are a transitional case, in which spectra resemble SNe II at early times but later evolve SN Ibc features (Filippenko et al. 1990).

The tail of the lightcurve of CC SNe is powered by the radioactive decay of $0.1\mathrm{M}_\odot$ of ^{56}Ni synthesized and ejected by the explosion, as it transitions first to ^{56}Co and then to ^{56}Fe . In type Ib/c, where the H-envelope is absent, the ^{56}Co decay powers almost the entire display and no plateau is seen. In SNe IIL, where a good portion of the H-envelope was lost but not all, a small plateau merges into the ^{56}Co powered tail so that a "linear" decline is observed.

CC SNe are characterized by their occurrence in regions of active star formation. They have been mainly observed in disks and spiral structures of late-type galaxies (e. g. Johnson & MacLeod 1963; Maza & van den Bergh 1976; Barbon et al. 1999), they are commonly found in OB-associations and H II regions (Bartunov et al. 1994; van Dyk et al. 1996; Tsvetkov et al. 2001), and they follow the radial distribution of Hα emission (Anderson & James 2009). Additionally, the CC-SN rate traces the cosmic star formation rate (Cappellaro et al. 1999; Mannucci et al. 2005; Dahlen et al. 2004; Botticella et al. 2008; Bazin et al. 2009; Graur et al. 2011). More-

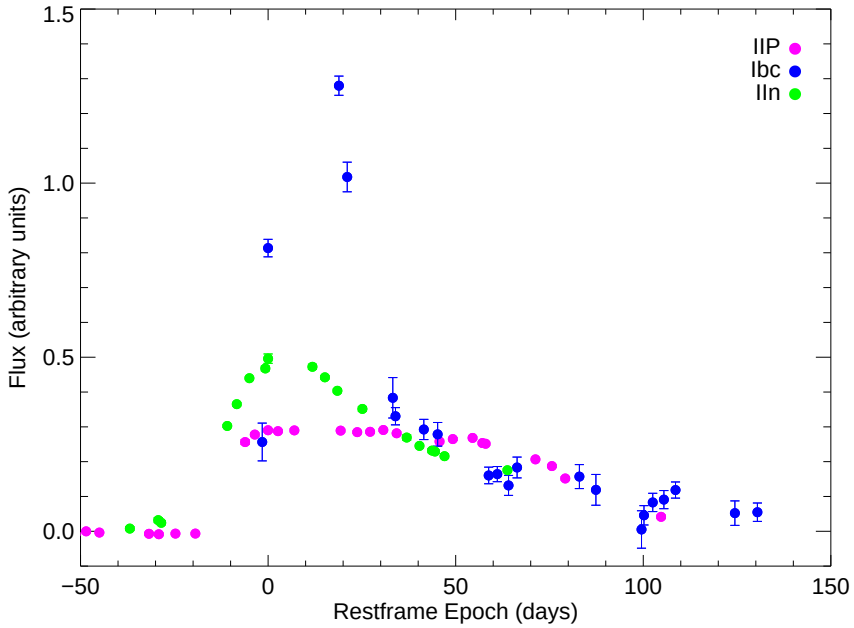

Figure 1.3: r_M-band lightcurves of 3 CC SNe from the Supernova Legacy Survey: IIP (pink dots), IIn (green dots) and Ibc (blue dots). The epochs are corrected to restframe for each respective redshift and the fluxes are normalized relative to an absolute magnitude of -16.0.

over, differences in the radial distributions and concentrations among the SN subtypes point towards a progenitor mass and metallicity dependence (Anderson & James 2008; Kelly et al. 2008; Prieto et al. 2008; Hakobyan et al. 2009; Boissier & Prantzos 2009; Habergham et al. 2010; Modjaz et al. 2011): SNe Ibc are more related to the bright, metal-rich regions of their host galaxies and follow the H II regions more closely than SNe II, and SNe Ic even more so than Ib.

The study of the copious neutrino emission of CC SNe, as seen for SN1987A (Bionta et al. 1987; Hirata et al. 1987), is of great importance for understanding the explosion mechanism and has opened up exciting possibilities for promising underground observatories (e. g. Koshiba 1992; Ewan 1992). Also, the study of the compact remnants left after the explosion, i. e., the neutron stars (NS), gives valuable insight into the physics of the explosion. Their velocities, or "kicks", for instance reveal that the explosion is asymmetrical (Cordes et al. 1993; Lyne & Lorimer 1994). The shape of supernova remnants, line profile studies (Wooden et al. 1993) and polarization measurements (Wang et al. 1997) confirm this.

1.3.2 Theory of explosion

Core-collapse SNe originate from massive stars ($M_{\mathrm{ZAMS}} \gtrsim 8\mathrm{M}_{\odot}$) that undergo core collapse after they have exhausted their iron fusion supply, only a 4-40 million years after being born. Massive stars have a complex evolution (see Woosley et al. 2002 for a review) where nuclear

fusion of higher mass elements occurs one after the other until a final iron core is produced. At this stage, no net energy can be produced and an electron degeneracy builds up that cannot halt the implosion as the mass of the iron core reaches the Chandrasekhar limit. The outer part of the core collapses rapidly (23% of light velocity in some milliseconds) due to its own gravity producing high-energy gamma rays that photo-dissociate iron nuclei into neutrons and α particles. Further neutrons and neutrinos are created as the core density increases and electrons are captured. The collapse is eventually stopped by neutron degeneracy and matter rebounds in a shock wave propagating outwards (Bethe et al. 1979). The shock wave dissociates elements in the core losing energy and starts to stall. At this point, a new energy source, like escaping neutrinos for example, is believed to power the explosion and blast the outer layers away. The collapse results in a compact object such as a neutron star or a black hole, depending on the initial mass of the star (Baade & Zwicky 1934). The rapidly expanding ejecta form then a supernova remnant that enriches the interstellar medium with heavy elements produced in the star and the explosion. This will later be used for a new generation of young stars that have more metals shaping ultimately the chemical evolution of galaxies.

This summarized picture of a core-collapse triggering a SN does not describe the detailed mechanism of the explosion. As a matter of fact, the initial shock needs to propagate through infalling material. The energy loss through dissociation of heavy nuclei and enormous neutrino luminosities created by electron capture stalls the shock, as shown in multiple simulations (e. g. Bruenn 1985; Wilson et al. 1986; Myra & Bludman 1989; Mezzacappa et al. 2001; Liebendörfer et al. 2001; Buras et al. 2003; Janka et al. 2004). This important issue is solved via the favorite mechanism of neutrino heating (e. g. Bethe & Wilson 1985; Wilson & Mayle 1988; Herant et al. 1994), in which neutrinos of all flavours from the nascent accreting neutron star in the center, that were initially trapped (due to mean free paths shorter that the star radius) diffuse out in a split second (Burrows 1990), and release their high degeneracy energy into thermal energy (Burrows & Lattimer 1986; Burrows 1988). In this way, the stalled shock gains energy deposited by a fraction of the escaping neutrinos in the region between the proto-neutron star and the stalled shock (Mayle & Wilson 1988; Burrows & Goshy 1993; Janka 2001). In multiple dimensions, simulations of the neutrino-driven explosion are accomplished with help of the advective-acoustic Standing-Accretion-Shock-Instability (SASI) (Foglizzo & Tagger 2000; Blondin et al. 2003). Alternative mechanisms to revive the stalled shock exist and include the acoustic power generated by core pulsations, proposed by Burrows et al. (2006).

The total energy liberated by the explosion is around 10^{53}ergs, most of it as neutrinos. The shock wave generated in the collapse is visible in UV after a few hours, once it reaches the surface of the star. The energy deposited by the shock in the envelope powers the lightcurve after peak maximum (and some decay energy of ^{56}Ni). This energy diffuses out and keeps the

envelope hot and the Hydrogen ionized. Depending on the envelope, a Hydrogen recombination wave propagates inward in mass (and velocity). The plateau of SNe IIP is explained by such hydrogen recombination of a large envelope at around $T \simeq 5500K$ that releases trapped radiation. Other CC SNe have less or no hydrogen layers, reducing the optical display. The decay of ^{56}Ni synthesized in the explosion powers the late time SN lightcurve. This exponential decline can be affected by dust formation that absorbs and re-emits light in the IR, so that the optical lightcurve decreases more rapidly. In some cases, the late recombination of ionized elements in the explosion can occur at epochs longer than the time of expansion of the SN (Leibundgut & Suntzeff 2003).

1.3.3 Progenitor scenarios

The wide variety of CC SNe, including radiated energy, chemical composition and kinetic energy, reflects a diverse range of progenitor properties affecting the output: mass, metallicity, binarity, mass-loss rate, rotation and magnetic activity (Podsiadlowski et al. 1992; Heger & Langer 2000; Hirschi et al. 2004; Yoon & Langer 2005).

According to theoretical models, the progenitors of SNe II are massive stars that retain the hydrogen envelopes (e. g. Woosley & Weaver 1986; Hamuy 2003). SNe IIP are believed to come from red supergiants (RSG) in the lower mass range of CC SNe ($8 - 20\mathrm{M}_{\odot}$). SNe IIL have lost some of their H-envelope (they have less than $\sim 2\mathrm{M}_{\odot}$ of H) and have higher mass progenitors, possibly early B stars (or alternatively are the result of a collapsing $8\mathrm{M}_{\odot} < M < 10\mathrm{M}_{\odot}$ ONeMg-WD). SNe IIb have even less hydrogen and presumably more massive progenitors.

SNe Ibc originate either from massive O stars that lose their hydrogen layers (and helium in some cases) by strong stellar winds, as predicted for Wolf-Rayet stars (WR) (SNe Ib would come from WN stars, WR stars with strong nitrogen emission lines, and SNe Ic from WC/WO stars, WR stars with dominant carbon/oxygen emission lines from the inner parts of a stripped star) with main sequence masses of $\gtrsim 25 - 30\mathrm{M}_{\odot}$ (e. g. Woosley et al. 1993; Heger et al. 2003; Maeder & Meynet 2004), or they come from lower mass stars that lose their envelopes though stripping from mass transfer in a binary system (e. g. Podsiadlowski et al. 2004a; Eldridge & Tout 2004), or a combination of both processes.

Therefore, the sequence of increasing hydrogen abundance and decreasing mass stripping for CC SNe is: Ic-Ib-IIb-IIL-IIP. Understanding the origin of this sequence is a key feature to progenitors. The other important element is the presence of circumstellar material interacting with the SN ejecta. The clearest of these is the SN IIn category, but objects of other types also show evidence of some interaction, like SNe IIL and IIP, and even possibly SNe Ia (e. g. Benetti et al. 1998; Sollerman et al. 1998; Turatto et al. 2000; Hamuy et al. 2003). Depending on the

CSM density, its location and extent, as well as the velocity of the ejecta, the interaction will be different and the lightcurve as well. The CSM will often come from previous episodes of mass loss of the progenitor stars.

The most direct way to probe progenitors is to look for them in pre-explosion images (e. g. Van Dyk et al. 2003; Smartt et al. 2004; Maund & Smartt 2005; Li et al. 2006b; Mattila et al. 2008; Leonard et al. 2008). Smartt et al. (2009) group those observations into a volume-limited sample and conclude with a maximum likelihood analysis that, for a Salpeter IMF[10], the progenitors of SNe IIP have a minimum mass of $8.5 \pm 1 M_{\odot}$ and a maximum allowed mass of $\sim 16 M_{\odot}$. The lack of progenitors with larger masses, beyond $17 M_{\odot}$, poses a challenge to previous theoretical models and suggest that these stars explode in other forms: IIL, IIn and Ibc SNe. This could mean that mass loss is more important than previously thought or that stellar metallicities were underestimated. Alternatively, RSG stars above this mass could end their lives in a direct black hole formation with extremely weak explosions (Fryer 1999; Heger et al. 2003).

The discovery of SNe Ibc progenitors through pre-explosion images has been inconclusive despite different attempts (e. g. Maund & Smartt 2005; Crockett et al. 2007). The non-detection however argues for another progenitor channel besides the WR stars, lower mass stars in interacting binaries (Smartt 2009). Furthermore, WR stars have masses larger than $\gtrsim 25 M_{\odot}$ (Massey 2003; Crowther 2007), which is not enough to account for the high estimated Ibc fractions (Smartt et al. 2009; Li et al. 2010a). Additionally, the observed ratio of WC/WN, which ranges between $\sim 0.1 - 1.2$ for different metallicities, as compared to the Ic/Ib ratio of ~ 2, suggests that binary interactions play a significant role (or that the WN stage is only a momentary phase in the evolution of WR stars). Finally, some SNe Ic of low energy have Carbon and Oxygen remnant masses that are much smaller than the observed masses of CO cores of WC stars (Crowther et al. 2002), an observation that argues that these stars are the outcome of interactions of lower mass stars in binary systems.

On the contrary, comprehensive recent environmental studies mentioned in § 1.3.1 indicate a sequence in the progenitor masses of CC SNe: II-Ib-Ic. This supports the idea that strong stellar winds strip the envelopes of massive single stars that collapse later in big SN displays. Nonetheless, the regions of high SN Ibc concentration also show a higher stellar density (Clark et al. 2008), and therefore a higher binary fraction, possibly leading to more frequent binary interactions and mergers that could contribute to this enhancement (Portegies Zwart et al. 2010). The most probable explanation is that both channels, single and binaries, contribute to SNe Ibc, although the exact fraction and extent of each remain to be found.

[10]The Initial Mass Function (IMF) is the empirical distribution of initial star masses. The Salpeter IMF (Salpeter 1955) has the shape $M^{-\alpha}$ with slope $\alpha = 2.35$.

Lastly, it is worth to mention that some SNe Ic have also been associated to long-duration Gamma Ray Bursts (LGRBs) (e. g. Mazzali et al. 2006; Valenti et al. 2008). These SNe Ic have broad line widths ($\sim 30000\mathrm{km/s}$) (e. g. Galama et al. 1998; Patat et al. 2001; Pian et al. 2006). The energetic jets may be powered by a central engine such as the newly formed and highly magnetized neutron star (magnetar) (e. g. Wheeler et al. 2000; Lyutikov & Blackman 2001; Drenkhahn & Spruit 2002) or a black hole with a rapidly rotating disk (collapsar) (Woosley 1993; MacFadyen & Woosley 1999). Not all WR stars (with $M_{\mathrm{ZAMS}} > 40\mathrm{M}_{\odot}$) produce broad-line SNe Ic since their fraction is much larger than the rate of broad-line SNe Ic (Podsiadlowski et al. 2004b). There is evidence that broad-line SNe Ic have different metallicities than normal SNe Ic arguing for a different progenitor (Modjaz 2011).

1.3.4 SNe IIP as distance indicators

Although they are intrinsically fainter than SNe Ia, SNe IIP represent the most homogeneous set of core-collapse SNe (Hamuy 2003) and their use as independent cosmological distance indicators has been demonstrated. There exist some theoretical-driven methods to calculate the distance such as the expanding photosphere method (Kirshner & Kwan 1974; Schmidt et al. 1994a; Hamuy et al. 2001) or the synthetic spectral fitting expanding atmosphere method (Baron et al. 2004; Dessart et al. 2008). An empirical simpler method, the standardized candle method, relies on the correlation between the expansion velocity and the brightness of SNe IIP during their plateau phase (Hamuy & Pinto 2002). The origin of this relation can be physically explained by the fact that more luminous SNe will have a hydrogen recombination wave at larger radii than fainter SNe, so that the velocity of the photosphere will also be greater (in a homologous expansion: $v \propto r$). Nugent et al. (2006) improved this method to moderate redshifts ($z \sim 0.3$) by adding an extinction correction based on the $V - I$ colors at day 50 after maximum. Other nearby studies of the standardized candle method for SNe IIP like Poznanski et al. (2009); Olivares (2008) and D'Andrea et al. (2010) for the SDSS, have increased the sample testing the validity of the method for a larger number of objects. The distance scatter oscillates between 10 and 18%.

Furthermore, NIR photometry can potentially improve the use of SNe IIP as standardizable candles. As dust causes less extinction in these bands, one should expect more precise Hubble diagrams. Maguire et al. (2010) present a local NIR Hubble diagram for SNe IIP with lower scatter than for optical bands (for the same SNe) although a larger sample is needed to confirm their results. Further studies of SNe IIP at low-z (ideally with IR data) should help understand the SN IIP properties and their standardizable capabilities better, so that future facilities can use the information to the SN IIP datasets that will be discovered at cosmological redshifts. SNe IIP have different and better understood progenitors than SNe Ia, and provide

a promising independent cosmological probe.

1.4 Motivation for this dissertation

The development of more powerful technologies to discover and characterize supernovae in the past years has revolutionized the field. The Supernova Legacy Survey (SNLS) has been fundamental in expanding our understanding of supernovae and their use for cosmology. With the aim of pinpointing the dark energy of the universe with greater accuracy, its rolling search strategy discovered more than ~ 500 spectroscopically confirmed SNe Ia in the intermediate redshift regime of $0.1 < z < 1.1$, during its five years of activity.

The SNLS has been incredibly successful at its goal (Astier et al. 2006; Guy et al. 2010; Conley et al. 2011; Sullivan et al. 2011a) and has contributed to achieve a new era of SN cosmology in which systematic errors are of the order of statistical errors. A real further improvement can only be attained by fully understanding the nature and extent of these systematic effects. In this process, the real challenge resides in finally grasping the nature of SN Ia progenitors and explosions. As long as the fundamental answers of SNe Ia remain elusive to us, the quest for the essence of the dark energy will not be satisfied. Currently, as previously shown, the largest systematic are the ones that we understand best and that are associated to observational effects. It is possible that as we find out more about SNe Ia, the main systematics may shift towards yet unknown biases of their explosions and evolution.

Numerous scientific studies of the SNLS, which are not directly related to cosmology, have explored these open questions on explosion and progenitors. These include environmental studies (Sullivan et al. 2006b; Howell et al. 2007) and the discovery of peculiar objects (Howell et al. 2006). Extreme cases like super-Chandrasekhar objects are an important test of the common SN Ia scenarios. In this thesis, we complement the studies to understand the nature of SNe Ia by analyzing another kind of weird SN Ia explosions that are very faint and short-lived: "subluminous" SNe Ia. Their explosions are a challenge for theorists, yet their fraction sufficiently high to represent an important piece of the SN Ia puzzle. With different environments, the SN Ia population mix may evolve with time and represent a potential concern for cosmology. The search for subluminous SNe Ia in the SNLS, the study of their properties and environments, as well as a rate evolution, are presented in Chapter 2.

Another important element in SN Ia studies, but not sufficiently analyzed, is the lightcurve rise-time. The SNLS possesses very well sampled lightcurves and provides a good opportunity to perform such analysis. Rise-time studies can directly probe some progenitor channels, and can give indications on the outer layers of the explosion. Furthermore, they provide an estimate of the amount of ^{56}Ni synthesized in the explosion and powering the lightcurve.

Differences in rise-time and ^{56}Ni mass can strongly vary among SNe Ia explosions, from subluminous to super-Chandra, and are hard to explain within the same theoretical framework. Finally, secondary lightcurve parameters besides the lightcurve-width relation, can directly affect the cosmological studies. We present a SNLS study of rise-time behavior across the SN Ia sample, including subluminous objects, in Chapter 3.

Besides its incredible utility for SNe Ia, the SNLS has discovered thousands of other transients that, excepting a CC rate measurement by Bazin et al. (2009), remain mostly unanalyzed in the database. This survey, however, offers the unique possibility to study large SN samples that will be characteristic in the future. Particularly, a current concern is the proper and efficient photometric typing of multiple SNe for large surveys. These will discover thousands of transients in short times and the spectroscopic follow-up of these will be impossible. With the increasing transient zoo, reliable photometric typing techniques are indispensable. We present in Chapter 4 an easy and effective SN IIP typing methodology, apt for large current and future surveys. Finally, we present the conclusions of this work in the final Chapter 5.

Chapter 2

Subluminous SNe Ia at High-z from the SNLS

2.1 Introduction

While it is commonly agreed that Type Ia Supernovae (SNe Ia) are thermonuclear disruptions of mass accreting C-O white dwarfs (WDs) in a binary system (Hoyle & Fowler 1960), the physics of the explosion and the nature of the companion are still under discussion. The study of the properties and environments of SNe Ia can help us solve the progenitor question. Successful progenitor and explosion models need to explain the variety in light-curve shape and spectra of SNe Ia. Recent multi-dimensional simulations of the explosion (Gamezo et al. 2005; Livne et al. 2005; Kuhlen et al. 2006; Kasen et al. 2009) show the asymmetric character of the delayed detonation and succeed to explain the scatter in the width-luminosity relation of the normal SNe Ia, although complications for the extreme SNe Ia still exist. In particular, subluminous SNe Ia – a group of objects considerably fainter at peak (up to 2 mag), with faster light-curves, redder at early phases, with distinct spectral characteristics such as Ti 2 and enhanced Si 2 – pose a challenge to any successful progenitor and explosion theory.

The prototypical example of a subluminous SN Ia is SN1991bg (e.g. Filippenko et al. 1992b) but many other examples have been discovered and studies of their properties relative to the bulk sample have been undertaken (Garnavich et al. 2004; Taubenberger et al. 2008; Kasliwal et al. 2008; Hicken et al. 2009). Subluminous SNe Ia are predominantly found in galaxies with older stellar populations, such as ellipticals and early-type spirals (Howell 2001), in contrast to the preference for the late-type, star forming hosts favored by bright, slow declining SNe Ia (Hamuy et al. 1996a, 2000). Subluminous SNe Ia also occur exclusively in massive galaxies whereas the normal sample spans a wider host stellar mass range (Neill et al. 2009). These observations set constraints on the delay-time – the time between the formation of the

binary system and subsequent SN explosion – ranging from < 1 Gyr for SNe occurring in star-forming regions to several Gyrs for SNe in quiescent environments. They could as well hint at differences in the metallicity abundance of the progenitors, due to the mass-metallicity relation (Tremonti et al. 2004), i. e., subluminous SNe Ia happen in more metal-rich environments.

Based on a sample from the Lick Observatory Supernova Search (LOSS) and the Beijing Astronomical Observatory Supernova Survey (BAOSS), Li et al. (2001a, 2010a) found that $17.9^{+7.2}_{-6.2}\%$ of all local SNe Ia are 1991bg-like, a possible overestimation as these surveys were host-targeted and could have systematically sampled brighter and more massive galaxies. The current observed subluminous sample remains a small fraction of the overall SN Ia population, although new and recent surveys are actively looking for them (Hicken et al. 2009). At high redshift, they are challenging to identify spectroscopically, and the current high-z SN surveys usually preferentially target normal SNe Ia for cosmological purposes. As a result, no 91bg-like SNe have been located at $z > 0.1$. For example, both, the Supernova Legacy Survey (SNLS) and the ESSENCE survey, report no spectra of 91bg-like objects at $z > 0.1$, although this is consistent with their selection effects (Bronder et al. 2008; Foley et al. 2009).

This raises an obvious question: is this non detection simply due to the difficulty of detecting and classifying these objects, or is the relative frequency actually lower at high redshift because there has not been enough time for them to explode as SNe Ia (Howell 2001)? Problems in the detection and classification arise from their intrinsic faintness, their rapidly evolving light-curves (which cause them to spend less time above the detection threshold for the same brightness), and their tendency to occur in brighter galaxies where the low contrast between the SN and host makes spectroscopy difficult. In this paper, we look for the fastest (and therefore faintest) SNe Ia at $z > 0.1$ in the Supernova Legacy Survey (SNLS) (Astier et al. 2006). Even without spectroscopic follow-up, we can use the excellent multi-band light-curves of the SNLS to look for subluminous SN Ia candidates by fitting subluminous SN Ia LC templates to the photometric data.

Beyond a simple detection, even more enlightening would be a measurement of the evolution in the volumetric rate of these objects. As it is a convolution of the star-formation history and the delay-time distribution, the SN Ia rate, in particular for sub-samples of SNe Ia, can test different progenitor scenarios. Rates for SNe Ia have been measured by several groups (e.g. Pain et al. 1996, 2002; Cappellaro et al. 1999; Dahlen et al. 2004, 2008; Neill et al. 2006; Dilday et al. 2008, 2010; Perrett et al. 2011; Li et al. 2010b). Combining the results one finds an increase with redshift up to $z \simeq 1.0$, although with large spread among surveys. If the rate evolution for the individual SN Ia populations differ, their delay-times must consequently vary and imply different conditions for the progenitors. As we probe higher redshifts, the SN Ia environments will differ from the local sample, and will be reflected in the rates. If the fraction of high-mass

(and high-metallicity) hosts was lower in the past, we would expect a similar behavior for the rate of subluminous SNe Ia.

By constraining the delay-time distribution, we seek to improve our understanding of the progenitors of subluminous SNe Ia. One can attempt to explain their progenitors in the SN Ia progenitor framework, where two main scenarios have been envisaged: the single-degenerate (SD) model, in which a non-degenerate companion donates H/He-rich material to a WD near the Chandrasekhar mass (Whelan & Iben 1973; Nomoto et al. 1984), and the double-degenerate scenario of two WDs coalescing (Iben & Tutukov 1984; Webbink 1984). In the SD scenario the delay-time is set by the age of the donor while in the DD model it depends on the age of the secondary and the merging time of the two WDs through gravitational wave radiation. The merging of two WDs has recently shown to be a viable mechanism, under certain conditions, for a successful subluminous explosion (Pakmor et al. 2010), although see a critique of their initial conditions in the work by Dan et al. (2011).

There is also a variety of independent mechanisms for subluminous explosions that explain the faintness by requiring a smaller burned mass of ^{56}Ni. Instead of a common explosion model for the whole range of SNe Ia, the delayed detonation (Mazzali et al. 2007) and other mechanisms like pure deflagrations or sub-Chandrasekhar CO or O-Ne-Mg WD off-center detonations (e.g. Livne 1990; Woosley & Weaver 1994; Filippenko et al. 1992b; Isern et al. 1991) provide less luminosity although with some observational discrepancies (Hoeflich & Khokhlov 1996). A failed neutron star model, in which C-O is accreted rapidly and ignited on the surface of the WD also leads to a faint SN Ia (Nomoto & Iben 1985). Recently proposed models of WD collisions in dense environments could potentially lead to subluminous explosions (Raskin et al. 2009b; Rosswog et al. 2009). Finally, a theoretically-motivated group of unusual objects, the so called SNe .Ia ("dot Ia") introduced by Bildsten et al. (2007), are the final helium shell flashes of AM CVn binaries. These are too dim and evolving too rapidly to be classical subluminous SNe Ia, but possible candidates are starting to appear (Poznanski et al. 2010; Kasliwal et al. 2010).

With a detection of subluminous SNe Ia at $z > 0.1$, the measurement of the rate evolution and study of their host environments, we can start setting constraints on the evolution of these objects and their properties, their delay-times and progenitors. This paper is a companion to Perrett et al. (2011), who have carried out a rate study of normal SN Ia sub-samples using the same SNLS data sample. We complement that study for the faint and short-lived SN Ia population up to $z = 0.6$. We use "stretch" as a LC-shape parameter (Perlmutter et al. 1997; Goldhaber et al. 2001; Conley et al. 2008) and define hereafter subluminous objects as SNe Ia with $s \leq 0.8$, inspired by the behavior of the color-stretch and magnitude-stretch relations (§2.2.1). This value is higher than the ones inferred from other studies (e.g. Taubenberger et al.

2008; Li et al. 2010a), as will be shown later. We emphasize therefore that our sample is less extreme and call it hereafter "low-stretch" (low-s) sample.

A brief outline of the paper follows. In §4.2 we investigate the nearby training sample of low-s SNe Ia and find the necessary LC relations for creating a template. §2.3 highlights the observations and candidate selection of the SNLS. With this, we measure the rate as a function of redshift in §2.4, taking into account systematic effects from possible errors in the estimated LC parameters and contamination from core-collapse supernovae (CC-SNe). The discussion of the rate measurements together with the investigation of the host galaxy properties of the candidates follow in §2.5 and we conclude in §3.6. We use a flat cosmology with $(\Omega_m, \Omega_\Lambda) = (0.27, 0.73)$ and $h = 0.7$.

2.2 Local relations for low-stretch SNe Ia

As shown by Garnavich et al. (2004); Taubenberger et al. (2008); Kasliwal et al. (2008) and Hicken et al. (2009), subluminous SNe Ia have clear photometric characteristics: red colors, a faint peak brightness, and a steeper relationship between LC shape and peak magnitude. In this section we derive new parameter relations based on a training sample of subluminous objects at low redshift. These relations will be of great importance to define proper low-s SN Ia LC templates and to correctly calculate the SNLS survey efficiency.

We use a local training sample from the literature (the low-z Constitution set and low-s, Table 2.1) that spans the stretch range, $0.45 < s < 1.30$, so that the behavior of low-s SNe can be compared with the normal population. We ensure adequate light-curve phase coverage, particularly at early epochs, by requiring observations in at least two filters between -15 and +8 (and between +5 and +25) effective days (corrected for stretch and redshift) after maximum brightness in B-band. Normally the local sample has enough post-maximum data whereas pre-maximum is scarce, so that many more points are included. We also include a sample at higher redshift from the SNLS consisting of spectroscopically-confirmed SNe Ia over $0.3 < z < 0.6$, which provides wider wavelength coverage compared to the low-z sample.

We perform SN Ia light curve fits to the entire sample with a modified version of the SiFTO algorithm (Conley et al. 2008). SiFTO manipulates spectral energy distribution (SED) templates to model SN Ia LCs. It has a wavelength-stretch dependence derived from strictly normal SNe Ia, which was removed for the modified version used here. Although SiFTO was built with a training sample that excluded peculiar objects like SN1991bg, we obtain very good fits to subluminous data down to $s \simeq 0.65$ and reasonable fits to lower stretch SNe (see Figure 2.1). Surprisingly, this template performs better than those built purely from subluminous objects like SN1991bg, which may have extreme features not suitable for all $s \leq 0.8$ objects. The suc-

cess of the fitting is partly because SiFTO fits each band independently without imposing any color-stretch relation, and so the unusual colors of subluminous SNe Ia do not pose a problem. The algorithm provides the LC parameters such as stretch and peak magnitudes to get colors at maximum B-band brightness with their respective errors, as well as quality-of-fit parameters.

We use a reduced overall goodness-of-fit $\chi^2_\nu < 5$ cut for normal and a higher $\chi^2_\nu < 11$ for low-s objects to account for the poorer fits of the more extreme objects. The final training set consists of: 207 low-z SNe Ia, of which 44 are low-s (see Table 2.1) with s down to $s = 0.45$, and 106 SNLS spectroscopic SNe Ia of which 3 are low-s. A list of all culls is shown in Table 2.3. We note that not all of the low-s SNe Ia listed by Neill et al. (2009) (Table 1) pass our selection criteria. Also, their stretch values for low-s objects are in average lower than ours. This is due to the modified version of SiFTO we use, which assumes a common single stretch independent of wavelength and which has been more extensively tested for low-s SNe Ia. Additionally, despite our light curve coverage criteria, one low-s candidate (SN2001da) does not have many data points and results in very different stretch ($s = 0.89$) when fit through the method of Neill et al. (2009). We take this supernova out of our analysis.

In order to develop tools to photometrically identify low-s SNe Ia and distinguish them from other transients, we also include a nearby and a high-z SNLS sample of spectroscopically-identified non-type Ia supernovae. 14 nearby and 21 SNLS CC-SNe are properly fit to a SN Ia SiFTO template, and 10 of those are assigned a $s \leq 0.8$ stretch (6 of which are low-z, see Table 2.2). This set of contaminants will give us an idea of the systematic uncertainties (more in §2.4.3).

Our limiting definition of low-s objects at $s = 0.8$ is inspired by the color-stretch and magnitude-color-stretch relations and is different from the "subluminous" definition studied in other surveys. We can compare it to the SALT2 LC-fitter (Guy et al. 2007) using similar equations to Eq. 6 in Guy et al. (2010), obtaining that $s = 0.8$ for our modified SiFTO version corresponds to $X_1 \simeq -1.85$. By directly matching subluminous SNe of Taubenberger et al. (2008) and fitting a linear relation between their $\Delta m_{15}(B)$ parameter (the amount of B-band magnitudes the SN has declined 15 days after maximum) and our SiFTO stretch, we obtain a corresponding value of $\Delta m_{15}(B) \simeq 1.54$. This value is lower than the one they find to separate their sample ($\simeq 1.70$, which would correspond to $s \simeq 0.72$) and confirms again that our sample is not as extreme.

2.2.1 Color-stretch relations

Modeling the colors of SNe Ia is fundamental for the LC fit and candidate selection of §2.3, as well as for the study of the recovery efficiency needed for the rate calculation of §2.4. The

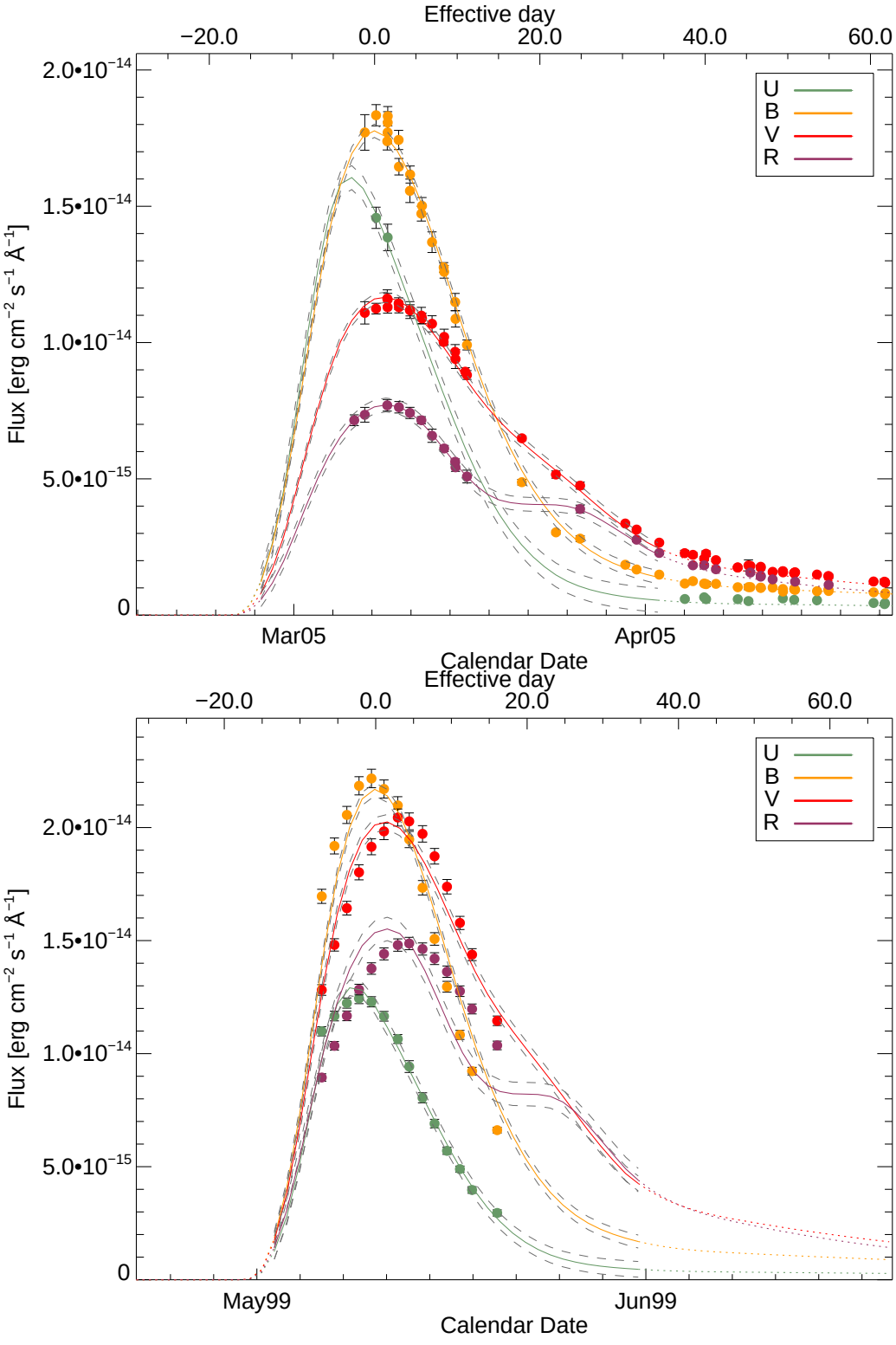

Figure 2.1: Example SiFTO LC fits of low-s SN2005am (Hicken et al. 2009; Li et al. 2006a) with stretch 0.71 and overall $\chi^2_\nu = 0.6$ and SN1999by (*lower*) with stretch 0.61 and $\chi^2_\nu = 8.5$. The fit is done for all points between -15 and 35 days in restframe.

challenge in modeling SN Ia colors resides in the difficulty of disentangling intrinsic and extrinsic colors, the latter coming mainly from reddening of the host galaxy. As explained in Conley et al. (2008), the SiFTO method does not impose a single color model across all filters, which would probably not encompass the whole range of SN Ia variability; rather the SED is adjusted to match the observed colors in each filter.

We first remove highly reddened objects by the foreground Milky Way using the Schlegel et al. (1998) dust maps and a cut of $E(B-V)_{\rm MW} < 0.15$. To get an idea of the intrinsic color-stretch relation of the objects, we take the transients that are hosted in less extincted passive galaxies, i.e. in galaxies catalogued as E/S0 for the nearby sample from the NED database[1] and in galaxies with no star formation for the SNLS (Sullivan et al. 2006b). A color similar to $B-V$ at B-band maximum brightness, c, as a function of stretch for these objects is shown in Figure 2.2 (filled circles and squares).

We create a "low-extinction sample" by taking all SNe, regardless of their hosts, with a color below the upper limit from the maximum found for the SNe in only quiescent environments, $c < 0.37$. This is only done for normal-s SNe Ia, i. e. $s > 0.8$, which have a relatively flat color-stretch relation. Low-stretch SNe Ia become redder at a steeper rate with decreasing stretch and are hosted in less dusty environments, so we do not use such a maximum color cut, although we remove known extremely extincted objects (e.g. SN1986G, SN2006br and SN2007ax). The fit to this larger sample (open and filled circles and squares) in Figure 2.2 is well represented by a piecewise linear model with a break at $s = 0.77$ (solid line):

$$c(s) = \begin{cases} C_0 + \gamma_1\,(s-1) & (s > 0.77) \\ C_0 + \gamma_2\,(s-1) + C_{\rm match} & (s \leq 0.77) \end{cases} \tag{2.1}$$

The fit parameters are $C_0 = 0.08 \pm 0.02$, $\gamma_1 = -0.06 \pm 0.02$, $\gamma_2 = -2.79 \pm 0.07$ and the transition stretch value $s = 0.77 \pm 0.01$. $C_{\rm match} = -0.23(\gamma_1 - \gamma_2)$ is a correction factor to unite both lines at $s = 0.77$. The transition value for stretch ($s = 0.77$), together with the one found for the magnitude-color-stretch relation in next section ($s = 0.82$), argues for our chosen limiting value of $s \simeq 0.8$ between low-s and normal-s. The piecewise linear model has the best fit (reduced χ^2_ν of 23.4) among other models (e. g. exponential with $\chi^2_\nu = 25.0$ or power law with $\chi^2_\nu = 25.9$), although there is a significant scatter in the objects. The figure shows that low-stretch SNe Ia are not only redder but their color-stretch relation is much steeper than for normal SNe Ia. Errors in stretch and color were propagated in the fits. Allowing a fit to all objects, also extincted ones, provides consistent results (with a transition stretch at $s = 0.83$)

[1]The NASA/IPAC Extragalactic Database (NED) is operated by the Jet Propulsion Laboratory, California Institute of Technology, under contract with the National Aeronautics and Space Administration

and is also shown in Figure 2.2. It is worth to mention that if we force a piecewise linear model with a fixed lower transition value of $s = 0.7$, more similar to characteristic "subluminous" surveys (Taubenberger et al. 2008), the fit is slightly worse ($\chi^2_\nu = 24.6$) and the slopes steeper. Due to the large scatter of colors at low-s, a range of consistent models (with $\chi^2 < \chi^2_{min} + 2$) is obtained for transition values of $0.69 - 0.87$.

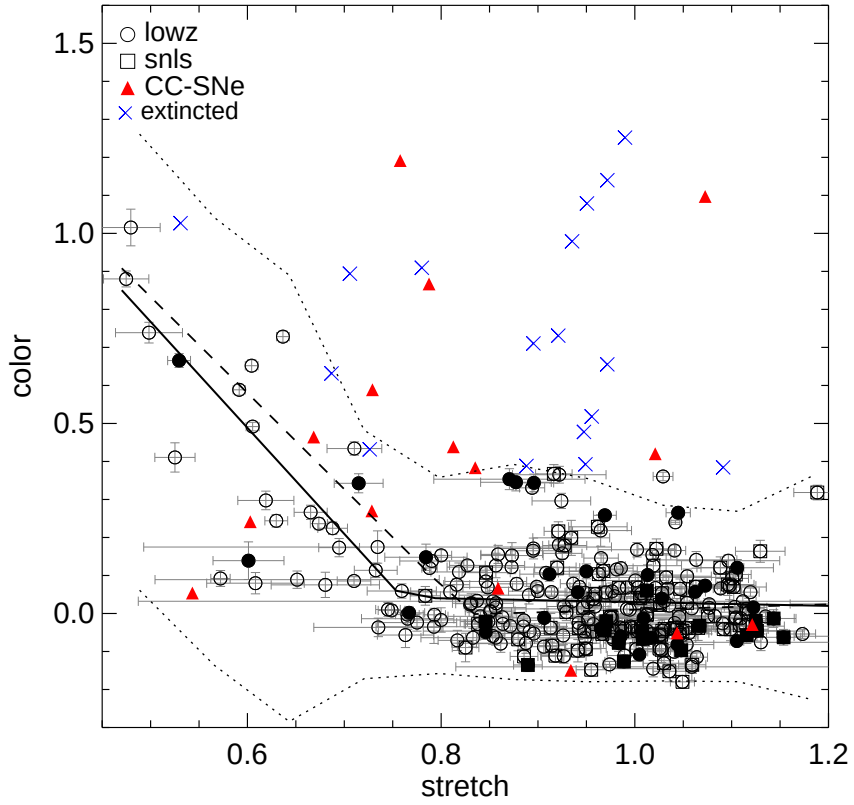

Figure 2.2: Color as a function of stretch for the local SN Ia sample (circles) and $0.3 < z < 0.6$ SNLS sample (squares). The filled points represent SNe in passive galaxies and the fit to exclusively those objects is the dashed line, a two-piece linear model changing at $s \simeq 0.8$. The "low-extinction" sample (open and filled black points) represent all objects with $c < 0.37$ regardless of the host galaxy. The solid line is the best two-piece linear fit to this sample and the dotted lines are the the $2 \times 2\sigma$ error-snakes. High-extinction SNe (blue crosses) are above the maximum possible intrinsic colors calculated from the SNe in passive galaxies and were not included in the fits. CC-SNe (red triangles) are also shown.

2.2.2 Luminosity-color-stretch

We next derive a relation between the absolute peak magnitude as a function of stretch and color. To limit the effects of peculiar velocities, we require SNe in our training sample to have either $z_{\rm CMB} > 0.01$ (CMB frame redshift) or a known distance to the host taken from the NED

database[2].

We fit simultaneously magnitude, stretch and color to different models. The best one is again bilinear in both, stretch and color. The absolute magnitude shows a steeper slope as a function of color for redder objects changing at $c \simeq 0.07$ (upper panel, Figure 2.3). Against stretch, the magnitude values (lower panel, Figure 2.3) are also well fit by a bilinear model with a shallower slope for the low-s stretch range. The effects in the differing slopes are not as strong as for the color-stretch relation but they will make the posterior analysis more precise. The errors in the absolute magnitude (from the apparent magnitude and redshift errors) and in the stretch and color are included in the fit. The magnitude-stretch-color relation can be summarized as follows:

$$M_B = M + \alpha_{[1,2]}\,(s-1) + \beta_{[a,b]}\,c + M^{match}_{[2,b]} \tag{2.2}$$

with $M = -19.11 \pm 0.01$, and where $\alpha_1 = -1.19 \pm 0.03$ and $\alpha_2 = -0.54 \pm 0.09$ are respectively used for stretch values greater and lower than the transition value of $s = 0.82 \pm 0.02$. $\beta_a = 3.00 \pm 0.02$ and $\beta_b = 2.15 \pm 0.05$ are used for values of c greater and lower than 0.07 ± 0.01, respectively. $M_2^{match} = -0.18(\alpha_1 - \alpha_2)$ and $M_b^{match} = 0.07(\beta_a - \beta_b)$ unite the fit at the changing values. This model results in a slightly better fit ($\chi^2_\nu = 19.6$) than other models (e. g. exponential –in stretch and color– with $\chi^2_\nu = 19.9$).

We include an asymmetric error-snake on these relations, shown by the dotted lines in Figures 2.2 and 2.3. These delimit (twice) the region within which 95% of all SNe Ia in each bin of 0.1 in color and 0.07 in stretch are found around the best model. The width of the region has been doubled to allow for the larger photometric scatter of the high-z SNe, which will be important later in §2.3.2. This region also covers any uncertainties in the relations modeled in this section and allows for scatter in the color of the SNe. Requiring all objects to be inside those error-snakes, i.e. color-stretch, magnitude-color and magnitude-stretch, we find that $\simeq 90\%$ of the normal and low-s SNe Ia pass the cut (see Table 2.3). However, only 2 contaminants (all SNe Ib/c) survive the same cull, a $\simeq 6\%$ of the total of contaminants (or "contamination rate"). We find this tradeoff to be beneficial. Reducing the contamination is useful when limiting the systematic errors as discussed in §2.4.3.

[2]The distance to a galaxy provided by NED is a mean of different available distance measurements from the literature such as Cepheids, RR Lyrae stars, Tully-Fisher, Surface Brightness Fluctuations, etc. It depends on the chosen Hubble constant modified by local flow parameters. The error corresponds to the standard deviation of these measurements.

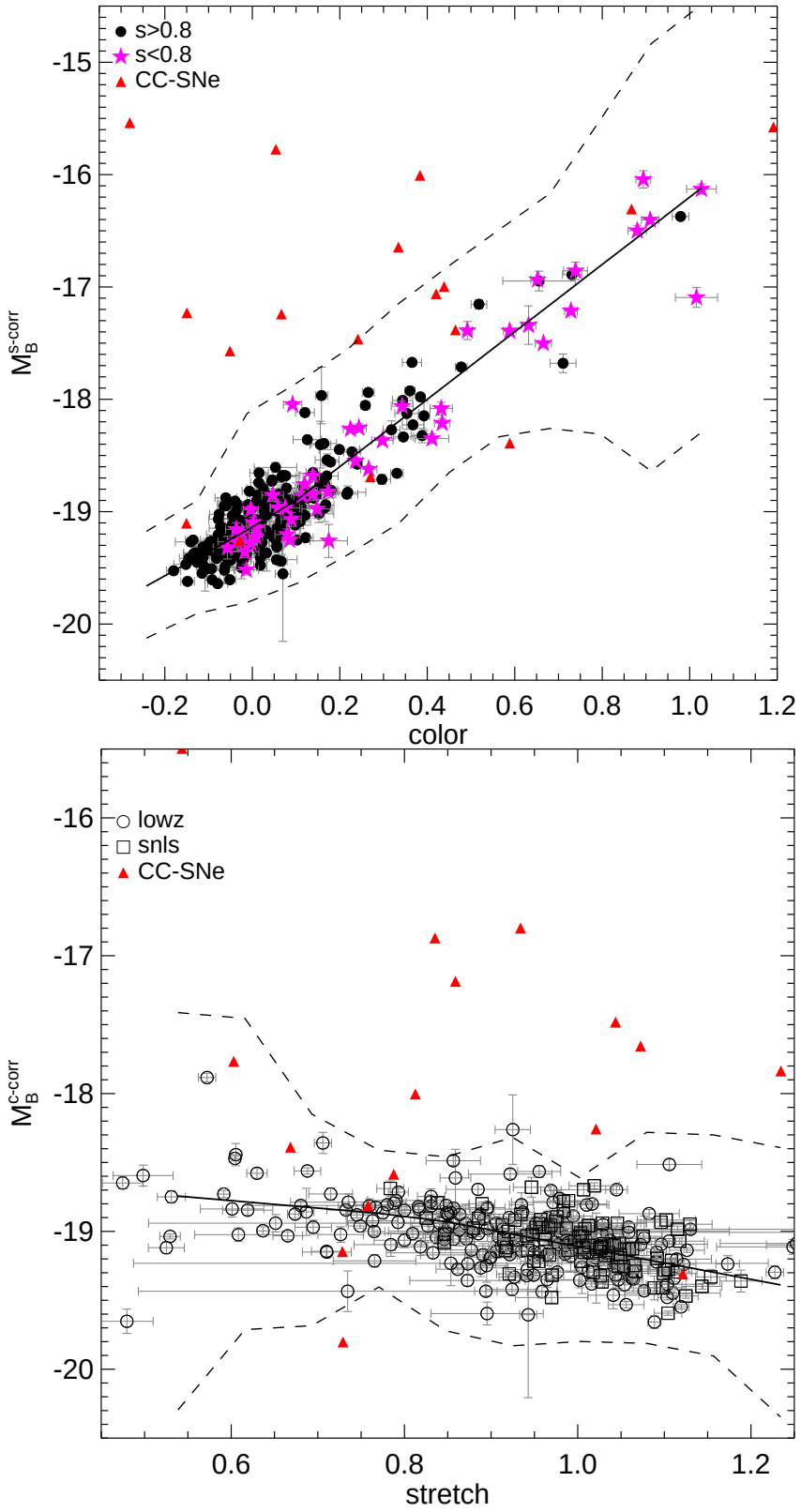

Figure 2.3: Absolute magnitude (corrected for stretch from Eq. 2.2, i. e. $M_B^{s-\mathrm{corr}} = M_B - \alpha_{[1,2]}(s-1) - M_2^{match}$) vs color (*upper*) and absolute magnitude (corrected for color, i. e. $M_B^{c-\mathrm{corr}} = M_B - \beta_{[a,b]}c - M_b^{match}$) vs stretch (*lower*) for the training sample. The solid lines represent the best fit model, a two-piece linear model for each case. The dashed lines are respectively the $2 \times 2\sigma$ error-snakes. CC-SNe (red triangles) are also shown.

2.3 High-z low-stretch candidate selection

The search component of the SNLS, carried out using the Canada-France-Hawaii Telescope (CFHT), is a wide field imaging survey well-suited to the detection of SNe Ia in the redshift range $0.1 \leq z \lesssim 1.0$ (Astier et al. 2006). It is a rolling search where four $1^\circ \times 1^\circ$ fields (D1 to D4) are imaged every few days, so that a well sampled LC is obtained in four filters ($g_M r_M i_M z_M$) for each discovered supernova (see Perrett et al. 2010 for a review). Good candidates are followed-up spectroscopically. Because they are faint, less frequent, and not vital for cosmological studies, typical subluminous SNe Ia are not prioritized in the spectroscopic follow-up (Sullivan et al. 2006a; Perrett et al. 2010). We can still use the well-sampled SNLS multi-wavelength LCs to photometrically identify these objects. The method used resembles the one for the normal-stretch population of Perrett et al. (2011, hereafter P11), although with appropriate adjustments for the low-s objects. This makes a direct comparison with the different stretch populations possible.

During the first 4 years of operation, up to July 2007, the candidate database consists of more than 5000 photometric transients including AGN, non-SNe and CC-SNe. As in P11, candidates in masked areas of the deep stacks are removed, as well as objects that lack the necessary LC coverage for a good photometric identification and parameterization. These observational criteria reduce the sample to half and are the same ones used for the SNLS training sample in §4.2: at least one g_M observation between -15 and 5 days of maximum, at least one r_M and one i_M observations between -15 and $+2.5$ days of maximum, at least one r_M and one i_M observations between -9 and $+7$ days of maximum, and at least one r_M or one i_M observation between $+5$ and $+20$ days of maximum.

2.3.1 Redshift estimation and LC fit

In P11, accurate photometric redshifts from the SNe were obtained with the use of two normal SN Ia LC fitters. Their approach requires a good spectroscopic sample for testing the method and the precision of the final photometric redshifts. We do not possess any 91bg-like SN Ia spectrum at high redshift with clear Ti 2 features, only 3 low-s objects at the border of our defintion, $s \lesssim 0.8$, that have spectra of rather normal SNe Ia. The high degree of degeneracy in the LC fits, particularly with stretch and redshift, which compete to make an object appear faint, demand an unbiased redshift estimate that will lead to appropriate LC parameters like stretch and color.

Several hundred objects of the 4-year dataset possess spectroscopic redshifts (spec-z) from either the SN or from the host galaxy. For the SN-derived redshifts, the SN type has been determined from the spectra in the majority of cases (Howell et al. 2005; Bronder et al. 2008;

Ellis et al. 2008; Balland et al. 2009; Walker et al. 2010). Most of these are normal SNe Ia (413), although a good sample of CC objects is also available (78). The host spec-z include data from DEEP/DEEP2 (Davis et al. 2003), VVDS (Le Fèvre et al. 2005), zCOSMOS (Lilly et al. 2007) and VIMOS (Jönsson et al. 2011). Many candidates without spectroscopic redshifts have host photometric redshifts from the SNLS broad-band photometry either using the spectral connectivity analysis method of Freeman et al. (2009), or, when no match is found, through fits to spectral energy distributions as in Sullivan et al. (2006b). The resulting host photo-z, $z_{\rm hostphot}$, are very good to $z \simeq 0.75$ with $\frac{|\Delta z|}{(1+z_{spec})} = 0.042$ and a low ($\sim 5\%$) catastrophic failure rate ($\frac{|z_{\rm spec}-z_{\rm hostphot}|}{(1+z_{\rm spec})} > 0.15$).

Fortunately, some of those SNe Ia with catastrophic redshifts can be identified with the help of the two LC fitters of P11 adjusted for low-s SN: `estimate_sn` (Sullivan et al. 2006a) and the aforementioned modified version of SiFTO (see §4.2). Their use in the multi-step process explained below provides good quality-of-fit parameters capable of distinguishing SNe Ia from CC-SNe, but also offer an independent mechanism for obtaining photometric redshifts using the SN, $z_{\rm SNphot}$, in cases where host redshifts are lacking.

Once the redshift is known, SiFTO is used to obtain the stretch and color of each SN. Tests on the local sample (§4.2) show that it works well without imposing any stretch-color model. As shown in Figure 2 of P11, the derived stretch is largely independent of the redshift because the rise and fall of SNe Ia are faster at shorter wavelengths, which largely compensates for redshift uncertainties. In Figure 2.4, we demonstrate that this behavior extends to low-s objects. Shifting the redshift –either photometric or spectroscopic– for each SN in our final low-s sample (see §2.3.2) by as much as $\Delta z = \pm 0.3$, we obtain a stretch variation lower than $\sim s \pm 0.1$. While this shows more dependence on redshift than the normal-stretch population, it still allows us to obtain accurate stretch estimates even in the presence of moderate redshift uncertainties.

The `estimate_sn` routine is described in more detail in Sullivan et al. (2006a). It performs a grid search on the χ^2 of a fit to SN photometry in flux space to a five-parameter model, including redshift. For this analysis, we modified it to include low-s objects using the color-stretch relations of Eq. 2.1, and the magnitude relation of Eq. 2.2. This fit depends on the assumed values of the cosmological parameters.

We calculated the SN photo-z for all objects in a similar fashion to P11 using the following multi-step process: First, we use `estimate_sn` to get a preliminary redshift estimate. We then use this redshift as a fixed input to a SiFTO fit to obtain an improved stretch measurement. Finally, we feed back this stretch to a final `estimate_sn` fit as a fixed parameter to obtain a more accurate $z_{\rm SNphot}$. We use this SN photo-z for SNe that do not have any other redshift (spectroscopic or host photometric).

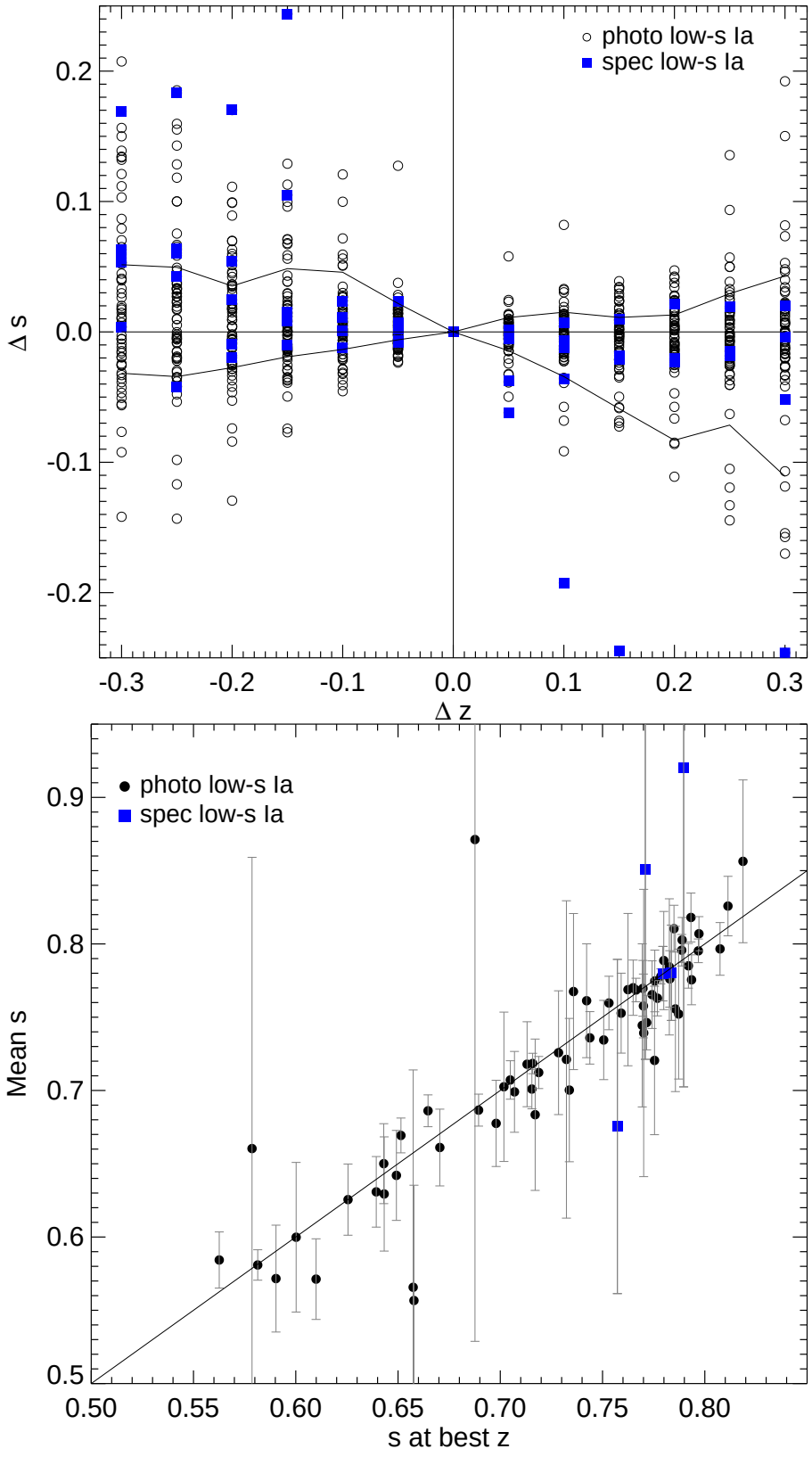

Figure 2.4: *Upper:* The change in fit stretch due to the deliberate variation in redshift for the low-s final sample of §2.3.2. The blue squares represent the spectroscopically-confirmed low-s SNe Ia. The solid black lines are the standard deviation above the median Δs. *Lower:* The average output stretch for each SN Ia as a function of its stretch (at zero redshift offset). The error bars are the change due to the variation in redshift for each SN Ia.

Objects with $z_{\rm hostphot}$ that have "bad fits", i.e. that do not pass all cuts of §2.3.2, are not discarded, but instead the cuts are re-applied using $z_{\rm SNphot}$. If this also fails, then the object is rejected. This offers some protection against catastrophic host photo-z failures. This recovers 29 confirmed SNe Ia. All known contaminants fail with both photo-z values, so we are confident that this procedure still rejects non-Ias. This process is summarized in a flow diagram (Figure 2.5).

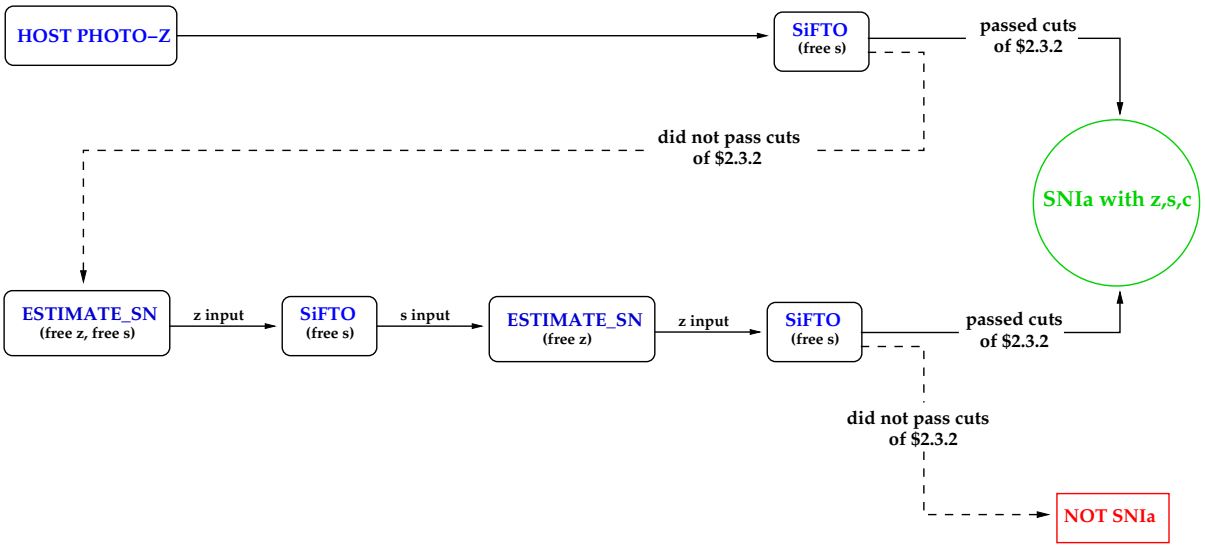

Figure 2.5: Flow diagram showing how SN Ia candidates without spectroscopic redshift are selected and how their photometric redshift is measured. If the objects do not have a photometric redshift estimate from the host or they fail to pass the selection cuts with that redshift, then the two LC fitters, `estimate_sn` and SiFTO are used to estimate a SN photo-z.

2.3.2 Final candidates

We perform final SiFTO (and low-s-modified `estimate_sn`) fits to each object to obtain the parameters of each SN and quality-of-fit values. A series of cuts are then applied to screen out objects with poorly estimated parameters or those unlikely to be SNe Ia. A summary of the applied culls and the number of objects surviving each of them can be found in Table 2.4. The χ^2 culls are similar to those of P11, although we weaken the requirements slightly for $s \leq 0.8$ objects based on the study of the low-z sample: reduced χ^2s of $\chi^2_{\rm estimate\_sn} < 13$ for the overall fit, and for individual passbands $\chi^2_{\rm estimate\_sn}(r_M) < 11$ and $\chi^2_{\rm estimate\_sn}(i_M) < 16$, and a SiFTO cull of $\chi^2_{\rm SiFTO} < 11$. Additionally, we require the objects to be inside the error-snakes trained in §4.2 with low-z low-s SNe in order to constrain their parameters (Figure 2.7). These cut values are derived empirically by trying to minimize the number of known contaminants that pass and minimize the number of rejected confirmed SNe Ia.

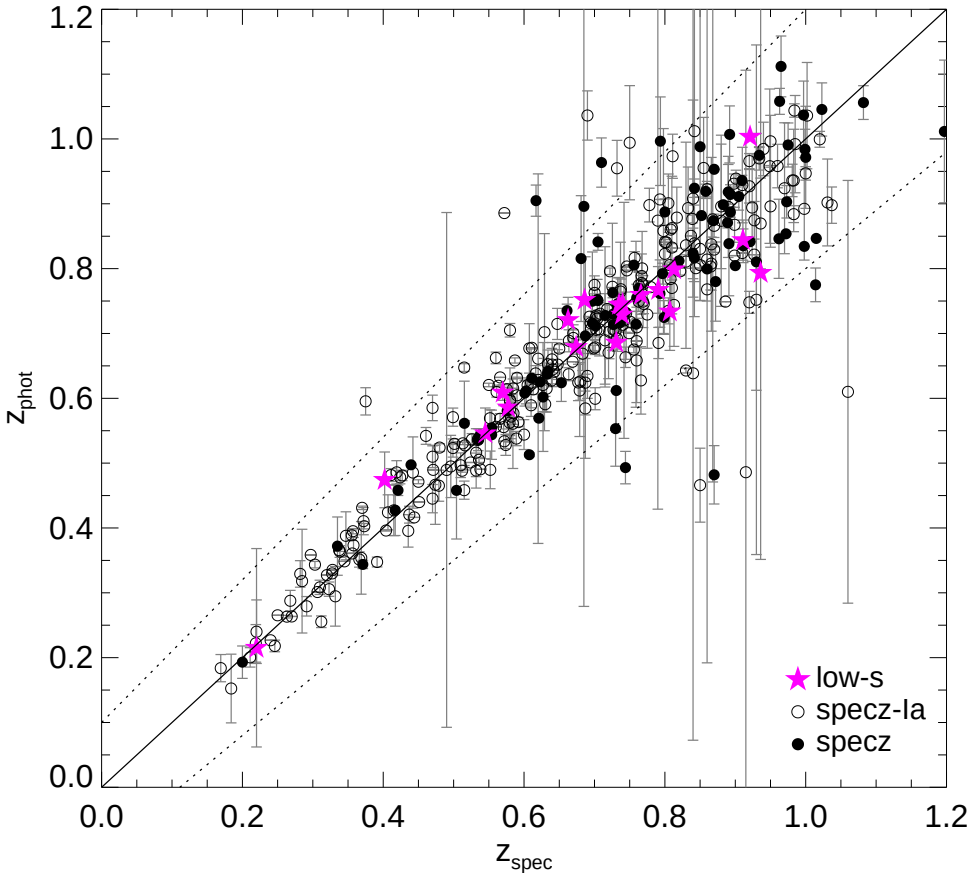

Figure 2.6: Photometric redshifts obtained from the host or from the LC fits compared to spectroscopic redshifts from the SN (open circles) or the host (filled circles). Purple stars represent $s \leq 0.8$ objects. The solid line shows 1:1 agreement and dashed lines a 10% uncertainty in $(1 + z_{\rm spec})$. The photo-z errors are either from the host or from `estimate_sn`.

At $z \leq 0.6$

Up to $z = 0.6$, the final sample contains 161 objects, of which 126 have spectroscopic redshifts. They span the stretch range $0.6 < s < 1.2$, of which 18 have $s \leq 0.8$ (see Table 2.5). Six of these have known spectroscopic redshifts: three are confirmed SNe Ia with $s \sim 0.8$ with no outstanding 91bg-like feature in their spectra, and the other three have spectroscopic redshifts but have too low of a contrast with the underlying host galaxy to conclusively establish the spectroscopic SN type. The final parameter distributions are shown in Figure 2.8 and Figure 2.9. The low-s photometric sample has median stretch and color of $\langle s \rangle = 0.74$ and $\langle c \rangle = 0.24$ (as compared to $\langle s \rangle = 1.00$ and $\langle c \rangle = 0.00$ for the normal-s population). The mean $\langle \Delta\mathrm{mag} \rangle = 0.76 \pm 0.69$ clearly shows that our low-s sample is not as extreme as the characteristic 91bg of $\Delta\mathrm{mag} \sim 2$mag.

The complete final set of photo-z contains 82% with host photo-z and 18% with SN photo-z. Figure 2.6 shows the comparison of photometric and spectroscopic redshifts for all SN Ia candidates with spectroscopic redshift either from the SN or the host. The median precision is $\frac{|\Delta z|}{(1+z_{spec})} = 0.030$. The photo-$z$ are more accurate to $z \simeq 0.6$ ($|\Delta z|/(1 + z_{spec}) = 0.025$), where our rate study will concentrate.

The final errors in photo-z are obtained from Figure 2.6 by taking the standard deviation around the median as a function of z. The stretch and color errors are provided by SiFTO, which requires a known redshift input. Stretch and color variations due to redshift uncertainties will be taken into account with a Monte Carlo simulation in § 2.4.2.

At $z > 0.6$

The detection incompleteness at $0.6 < z < 1.0$ increases rapidly for low-s SNe Ia, as will be shown in next section. We still find a significant population of 44 candidates (11 with spec-z from the host and 5 with low signal-to-noise spec-z from the SN, 2 of which are confirmed SNe Ia of $s \sim 0.8$ and no 91bg features) with median stretch, $\langle s \rangle = 0.76$, and color, $\langle c \rangle = -0.02$. The average color is extremely blue compared to the median color at $z < 0.6$ of 0.24 confirming that we are only observing the blue tail of the low-s distribution. This can be seen in Figure 2.10. They are not very faint objects, even for low-stretch, as shown in Figure 2.9. The lack of characteristic low-s red objects makes it difficult to reliably estimate the low-s rate at $z > 0.6$ and proper corrections need to be made (see § 2.4.2).

Additionally, we do find a presence of blue low-s candidates at high-z which are absent at lower-z. Such blue objects with $c < -0.05$ are neither found in the nearby nor in the $z < 0.6$ SNLS samples, but represent $\sim 30\%$ (14) of all $z > 0.6$ low-s objects. We do not expect all of these objects to be CC-SNe, which could potentially contaminate the low-s sample with their

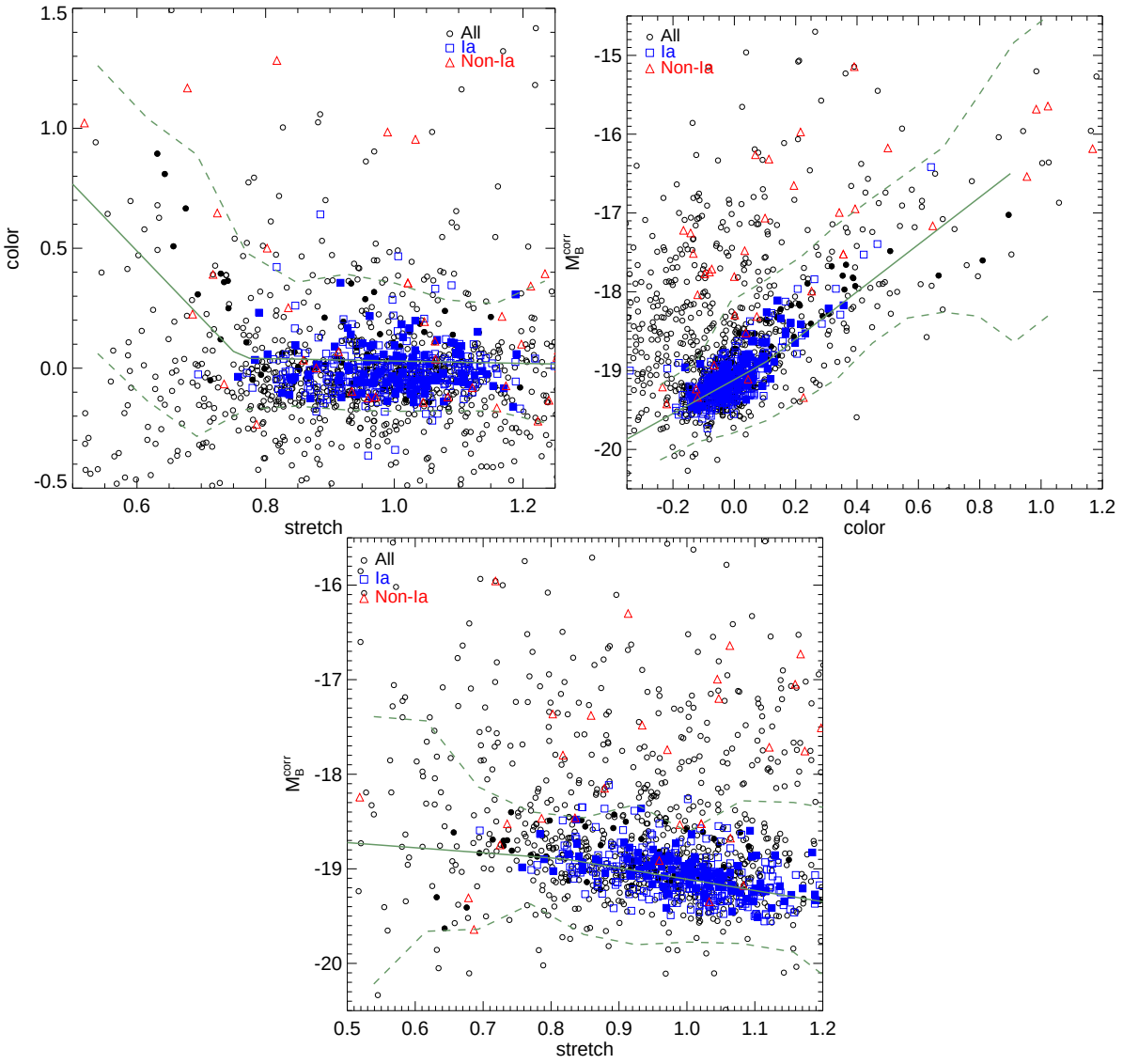

Figure 2.7: Color-stretch (*left*), magnitude-color (*middle*) and magnitude-stretch (*right*) for all SNLS objects passing the observation criteria (open points) and the final SN Ia photometric $z < 0.6$ sample after all cuts of Table 2.4 (filled points). Spectroscopically-confirmed SNe Ia (blue squares) and non-Ia (red triangles) are shown. The lines are the best-fit relations and error-snakes found in §4.2 for the local training sample, and served as additional cuts.

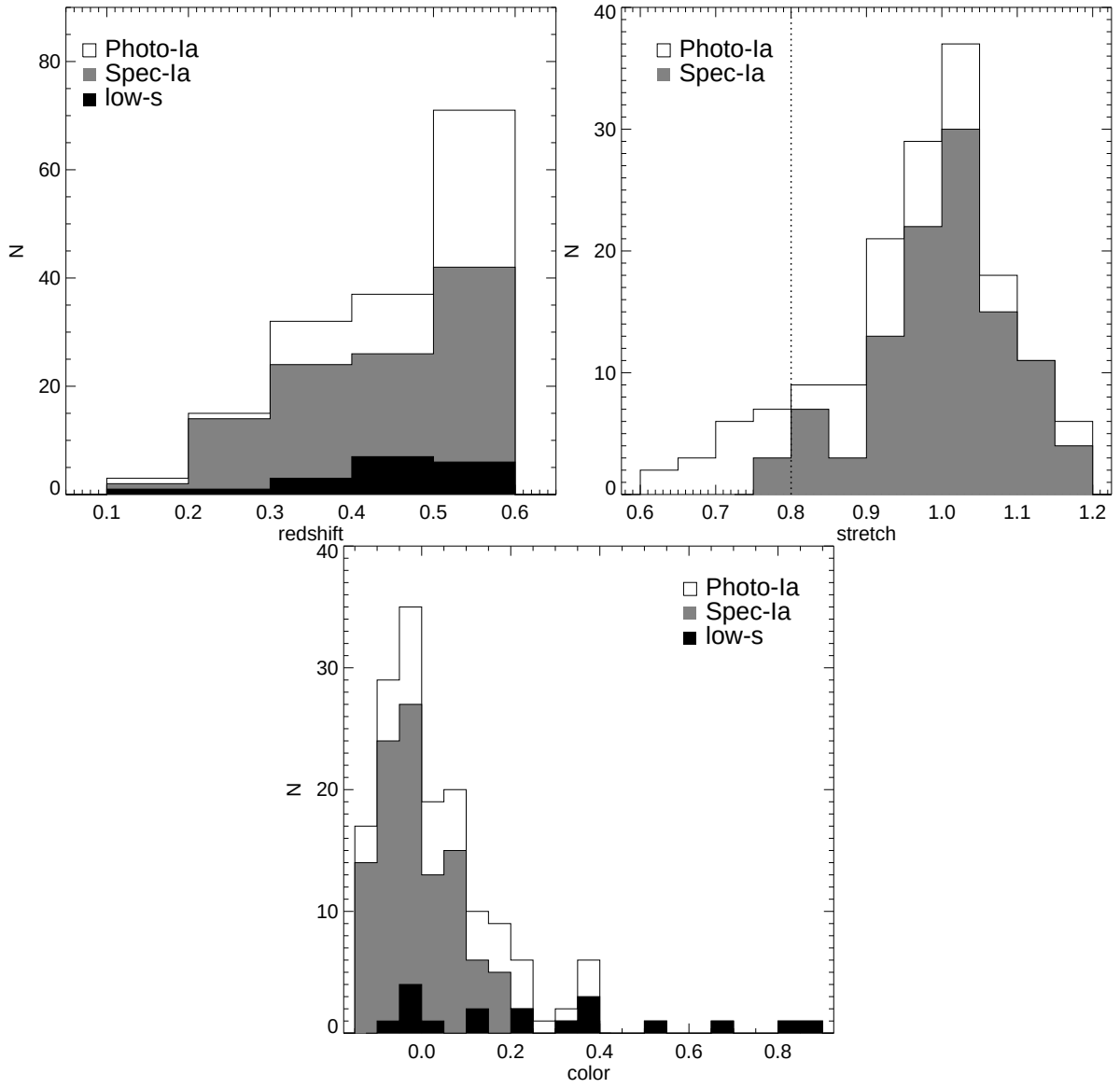

Figure 2.8: Final distributions in redshift (left), stretch (center) and color (right) of the $z < 0.6$ SN Ia photometric sample including low-s. The white histogram is the whole population, the gray is the spectroscopically-confirmed SNe Ia and the black the low-s candidates.

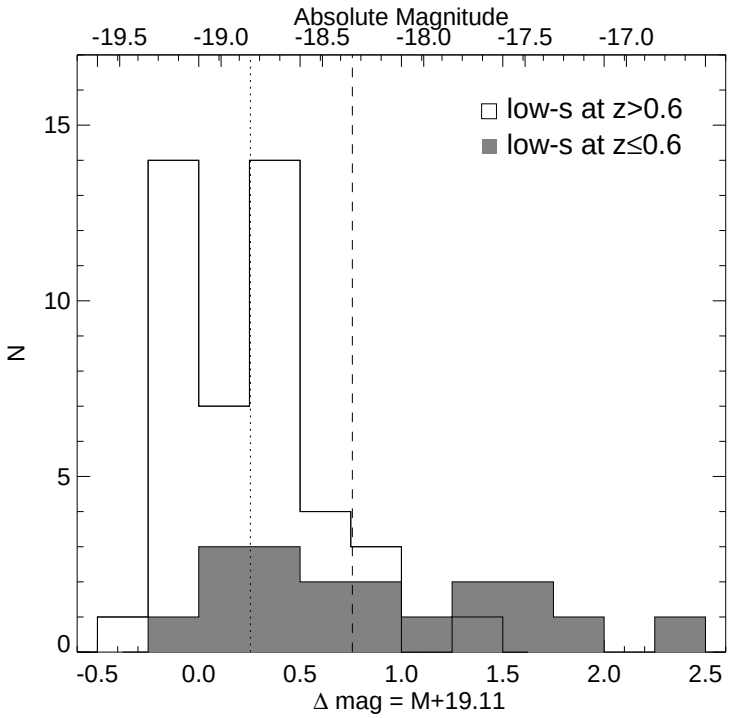

Figure 2.9: Distribution in Δmag of the final low-s candidate sample. $\Delta mag = M + 19.11$ is the difference between the absolute magnitude of each SN compared to the magnitude -19.11mag of a "standard" SN Ia at $s = 1$ and $c = 0$ according to eq. 2.2. The shaded histogram shows only the low-s SNe Ia at $z < 0.6$.

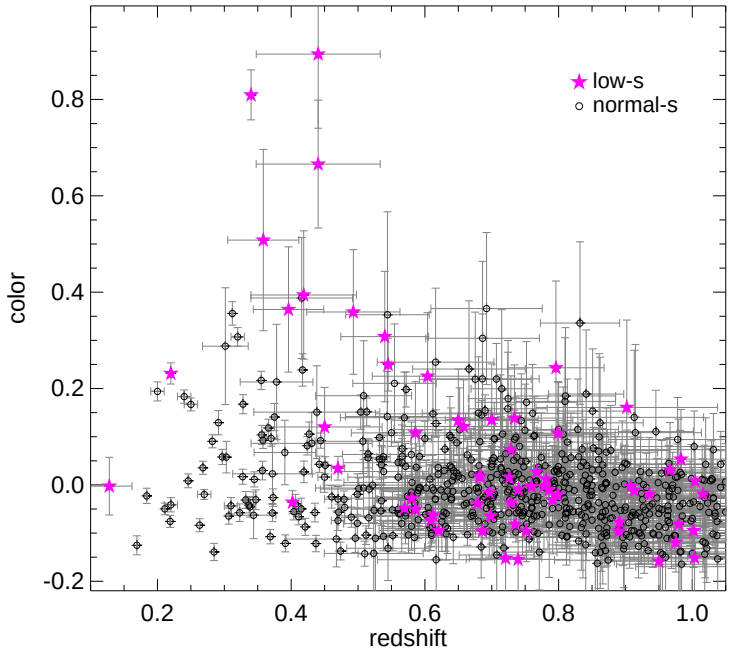

Figure 2.10: Color as a function of redshift for the final photometric SN Ia sample. Normal-s (black circles) and low-s (purple stars) are highlighted.

characteristic bluer colors. As will be shown later, besides going through our SN Ia pipeline, the environment of these candidates is not characteristic of CC-SNe.

A second possibility is that this group represents another class of transients that are fast and blue. The object found by Perets et al. (2010) is faint and fast-evolving but with clear different spectroscopic features and bluer colors than 91bg-like objects. It is hosted in an old stellar population as well as most of our candidates. However, our objects are not as faint (Figure 2.9). On the other hand, the transients found by Poznanski et al. (2010) and Kasliwal et al. (2010), suggested SN .Ia-like helium detonations of a WD, are blue and of similar brightness than ours, but evolve faster. When fit with our templates, we obtain very poor fits with $s = 0.44$ and $s = 0.33$, respectively, lower than our lower stretch limit for subluminous SNe Ia.

A tempting explanation is that the input photometric redshift for the LC fit is consistently wrong and affects the obtained color and stretch. This hypothesis is ruled out because 7 of these objects have spectroscopic redshift and the rest (except one) have photometric redshift from the host (with mean photo-z error of ~ 0.08), which do not show any significant systematic. We have seen the small effect in the measured stretch when the redshift is varied (Figure 2.4). We now show the effect in the magnitude and color of photometric candidates in Figure 2.11. Their variation due to changes in photo-z cannot account for all the bluer colors but for some of them –only if the redshifts were all consistently overestimated by $+0.05$, the colors would be redder by $+0.08$ (and magnitudes fainter by $+0.17$, whereas stretches would only change by -0.004).

Photometric errors in stretch and color get larger as we probe higher redshifts. Most of the candidates found at these redshifts have stretch close to the limiting definition of $s = 0.8$, so that they are consistent with being fast normal-s SNe Ia. Only 3 candidates have $s+s_{\rm error} < 0.8$, one of them with $s < 0.6$. Of these,two also have $c + c_{\rm error} < -0.05$, inconsistent with typical low-s colors, and will be further discussed in 2.4.3. The rest can therefore be explained as the blue tail of $s \sim 0.8$ objects while the redder counterpart remains unseen due to selection effects. In the remainder of this work, we treat this group as such and correct for this selection bias when calculating the rates.

2.4 Low-stretch SN Ia rate evolution

With a set of low-s candidates, we proceed to calculate a volumetric rate as a function of redshift. As in P11, the volumetric rate, $r_b(z_b)$, for a given redshift bin, represented here by the middle of the redshift bin, z_b, is given by the sum over all N_b candidates inside the bin:

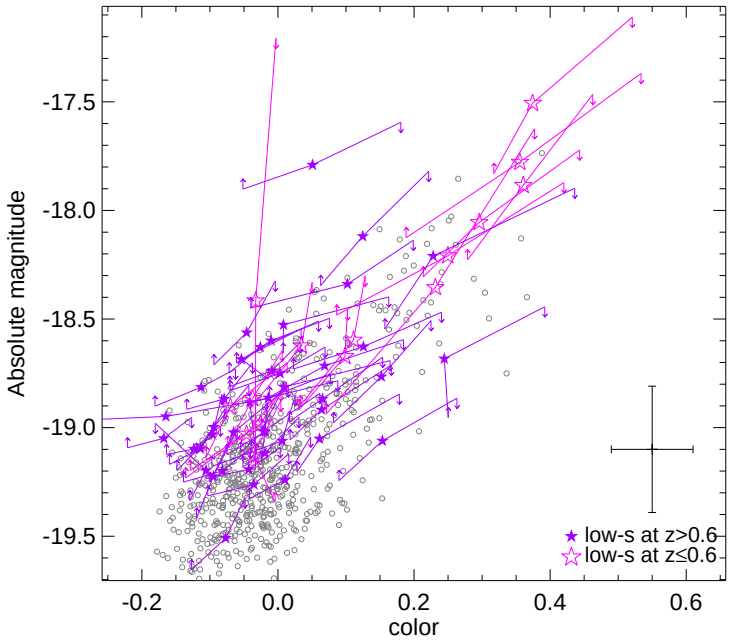

Figure 2.11: Absolute magnitude vs color for the low-s SN Ia sample with photo-z at $z < 0.6$ (big open pink stars) and at $z > 0.6$ (small filled purple stars). The dots show the normal-s sample. The upward and downward arrows show the new magnitudes and colors when varying the photo-z by $+0.05$ and -0.05 respectively. The lines unite the same object at the three redshifts. The lower right error bars represent the typical (mean) photometric errors.

$$r_b(z_b) = \frac{1}{V_b} \sum_{i=1}^{N_b} \frac{(1+z_i)}{\epsilon_i \Delta T_i}, \tag{2.3}$$

where ϵ is the individual SN detection efficiency depending on the characteristics of each object (like redshift, stretch and color) and ΔT is the sampling time accessible to find the object, divided by $(1+z)$ to account for time dilation. V_b is the comoving volume contained in the redshift range of the bin.

2.4.1 Detection efficiencies

The detection efficiencies ϵ_i account for observing biases measuring the rate. They depend on numerous factors and are specified as a function of the SN characteristics such as redshift, stretch and color (along with field and year of observation). The efficiencies used here are described in P11 and Perrett et al. (2010), and are based on a Monte-Carlo study of 2.4 million artificial SNe Ia injected into the actual SNLS images. This approach avoids the need to make assumptions about temporal and spatial data coverage.

The artificial SNe are generated using uniform distributions of redshift and stretch (down to $s = 0.5$), and the color is determined using a relation like Eq. 2.1, including an intrinsic scat-

ter around the stretch-color relation (a Gaussian noise with dispersion $\sigma = 0.04$ added independently to U and V). The peak magnitudes are generated from the luminosity-stretch-color relation, as in Eq. 2.2, and the redshift and assumed cosmology, plus an additional unmodeled magnitude dispersion from a Gaussian distribution with an intrinsic scatter of $\sigma_{int} = 0.15$. The LC is generated from integrating, at a given epoch and through the filter functions, the SN Ia spectral templates scaled for the B-magnitude and corrected for $U - B$ and $B - V$ colors, Milky Way and host extinction. The artificial SN is then inserted into each i_M image obtained by the SNLS. The images are then processed through the same pipeline used in the real-time SN discovery, and the recovered fraction is used to derive the efficiency as a function of various parameters, including redshift, stretch, color, observing season and field (see a more detailed description in Perrett et al. 2010). The low-s candidates, which are faint, red and have a rapid rise and fall, are more difficult to detect and therefore have a lower efficiency, so are accordingly given a higher weight when calculating the rates.

The efficiencies are calculated in bins of width $\Delta z = \Delta s = \Delta c = 0.1$. The measured efficiencies, linearly interpolated according to each SN, are shown in Figure 2.12. It can be seen that the mean efficiencies are lower for the low-s sample up to $z \sim 0.6$. Above $z = 0.6$, the mean efficiencies seem to approach the normal-s sample. At these redshifts they become low for all but the bluest low-s objects. This leads to a higher fraction of low-s blue objects with very few red ones recovered, as found in § 2.3.2. We show the expected efficiency distribution for the missing red, low-s SNe Ia of an unevolving color distribution as green squares in Figure 2.12 based on the observed low-s color distribution at low redshift from §2.8. The rates at $z > 0.6$ will need to be corrected for these missing objects (see next section). We note that the efficiencies shown in Figure 2.12 are the raw efficiencies –the recovery fraction from the simulated SNe– without the observational constraints of section § 2.3 nor the sampling time correction that depends on each field and season. These corrections can make the actual efficiencies much lower (see P11). For instance, one of our low-s candidates at high-z with $z = 0.80$, $s = 0.63$ and $c = 0.24$ has a raw efficiency of 0.54 but with observational constraints and sampling time this efficiency is only 0.18, which explains why these objects are hard to observe.

2.4.2 SN Ia Rates and Monte-Carlo simulations

We calculate a rate evolution, $r_{\rm meas}$, shown in Column 5 of Table 2.6 solely based on Eq. 2.3 and with the efficiencies from § 2.4.1. We use bins of $\Delta z = 0.2$ due to the low sample statistics (the last z-bin is only 0.1 wide as no low-s candidate exists beyond $z = 1$). The measured errors in stretch and color from the LC fit, and especially the errors in the photometric redshift of each candidate, can lead to uncertainties in the rate measurement. We account for these

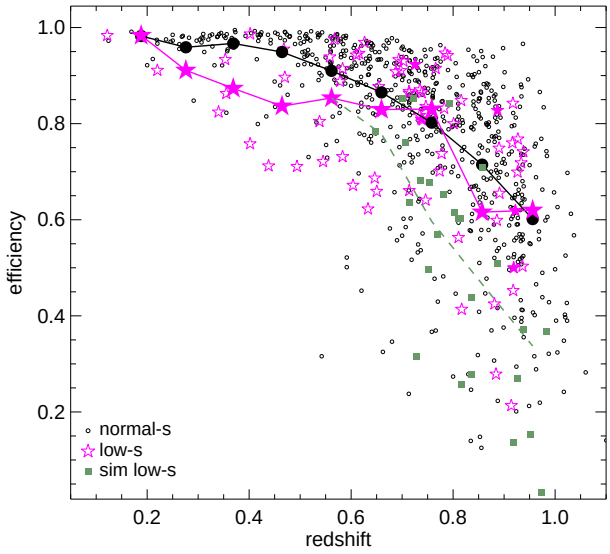

Figure 2.12: Efficiencies calculated by P11 for the SN Ia photometric sample for normal-s (black circles) and low-s (purple stars) populations. For objects where no direct efficiency was found (small filled stars), the closest match in color was used. Mean values in redshift bins for normal-s and low-s populations (big filled circles and stars) are shown. Additionally, simulated low-s objects for $z > 0.6$ bins (green squares) based on the $z < 0.6$ color distribution and respective mean (green dashed line) are shown for comparison. Note that these efficiencies do not include the observation criteria of section § 2.3 and sampling time correction of the different fields observed.

via a Monte-Carlo (MC) simulation that randomly shifts the photometric redshift according to its error (for those SNe Ia with photo-z). For each redshift, a corresponding LC fit provides new parameters and its covariance matrix. This latter is used to generate a new random set of stretch and color using standard techniques (James & Roos 1975). We recalculate the rates from Eq. 2.3 for each iteration based on the randomized values, and use the median value over the 1000 realizations to determine the final rate, $r_{\rm MC}$. We estimate the error from the variance of the rates in each bin (and call them "MC" errors shown in Column 6 of Table 2.6 and Figure 2.13) and add it in quadrature to the weighted 1σ Poisson statistical errors in Figure 2.13 (confidence levels calculated using the Clopper-Pearson method used for example in Gehrels 1986). The error simulation differs from P11, as the SNLS does not possess a known spectroscopic sample of low-s SNe Ia from which we could obtain parameter distributions. Instead, we treat each SN individually by randomly drawing parameters according to its errors and covariances. Although the precise details of our simulation differ from P11, a SN Ia rate evolution within the errors is obtained. It is worthwile to mention that this MC approach handles interlopers from the $s > 0.8$ population leaking into the low-s sample (and vice-versa) by taking into account the stretch uncertainties in the simulation.

Additionally, we have seen in the previous section that we do not find red objects in the

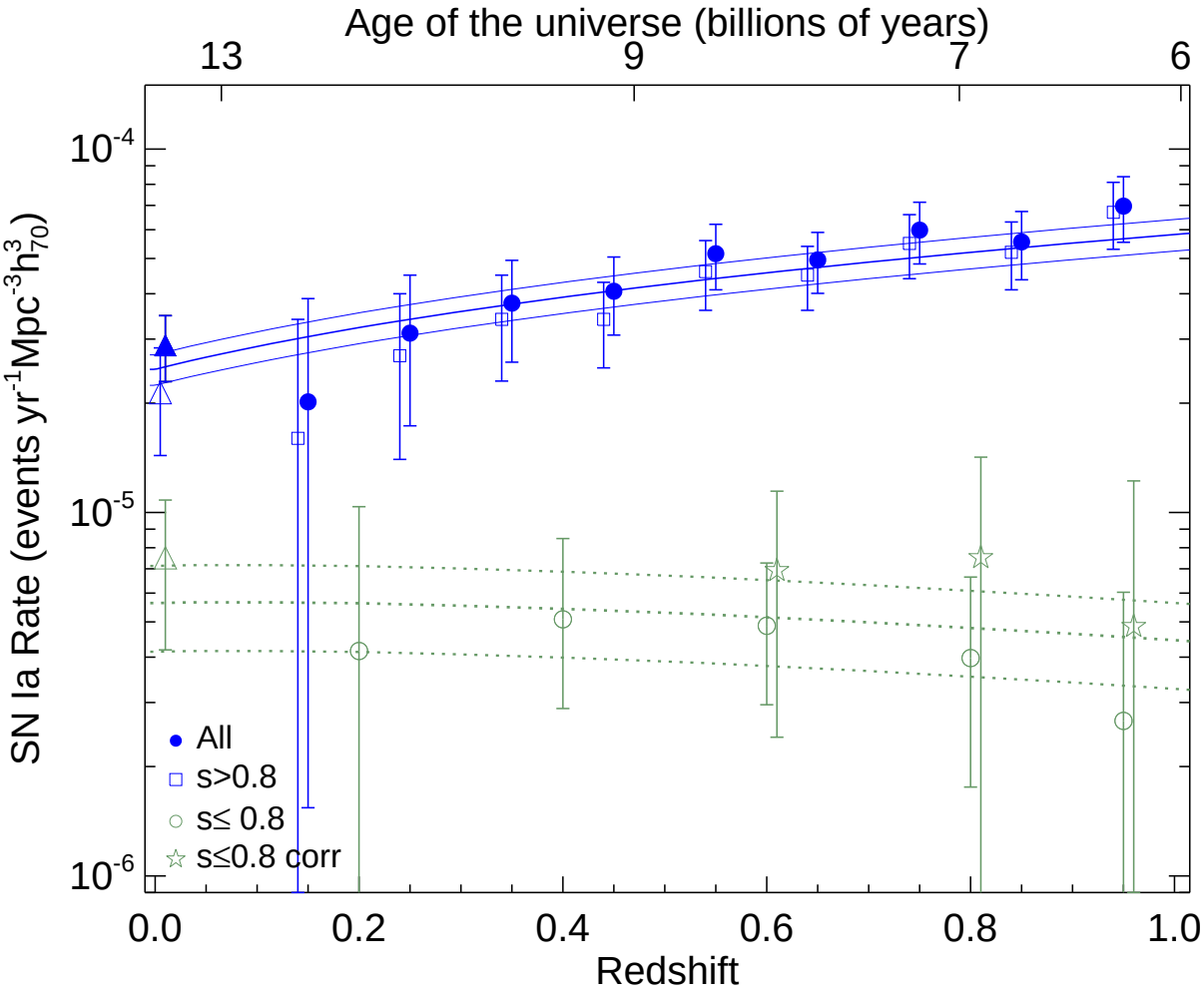

Figure 2.13: Volumetric rate of low-s SNe Ia as a function of redshift (green open points) compared to the normal-s rate (blue squared points) of P11. The total summed rate (blue filled points) is shown with a little z-offset for clarity. The stars represent the corrected high-z low-s rate calculated from real and simulated objects drawn from a distribution scaled to the $z < 0.6$ color distribution. The filled triangle is the total nearby SN Ia rate from Li et al. (2010b) and the open triangle is the low-s rate estimated from a $s \leq 0.8$ fraction of it. The solid lines are the best $A + B$ model and uncertainties found in P11. The dashed lines are the best A-model and uncertainties found in this study through a fit of only SNLS $z < 0.6$ bins: $A = (1.05 \pm 0.28) \times 10^{-14}\,\mathrm{SNe\,yr^{-1}}M_{\odot}^{-1}$.

higher-z bins. This selection bias results in underestimated rate values at high-z, which are not corrected in the MC by the efficiencies of the bluer objects found. There is a lack of objects in certain red color bins, so that no efficiency can account for them. To measure this effect, we take the low-s distribution of color in an underestimated high-z bin (for each MC iteration), we normalize this distribution to the known color distribution at $z < 0.6$ (right Figure 2.8), which has already been corrected for the efficiencies of each SN, and then generate fake SNe in the missing color bins. The normalization is done with the two bluest matching bins. Figure 2.14 shows an example for $0.7 < z < 0.9$. The green open histogram is the final corrected histogram from the initial observed diagonal-shaded distribution. The correcting factor for this case is $f_{b,\mathrm{corr}} = 1 + \frac{N_b(\mathrm{fake})}{N_b} = 1.9$, where N_b(fake) is the number of generated SNe in the bin and N_b is the observed number, so that the corrected rate is $r_{b,\mathrm{corr}} = r_b \times f_{b,\mathrm{corr}}$. The final correcting factors from the median of all MC iterations, summed Poisson (from the number of objects used in the bins used to normalize both distributions) and MC errors, as well as the resulting corrected rates are shown in the last two columns of Table 2.6. In Figure 2.13, the corrected rates are shown as stars.

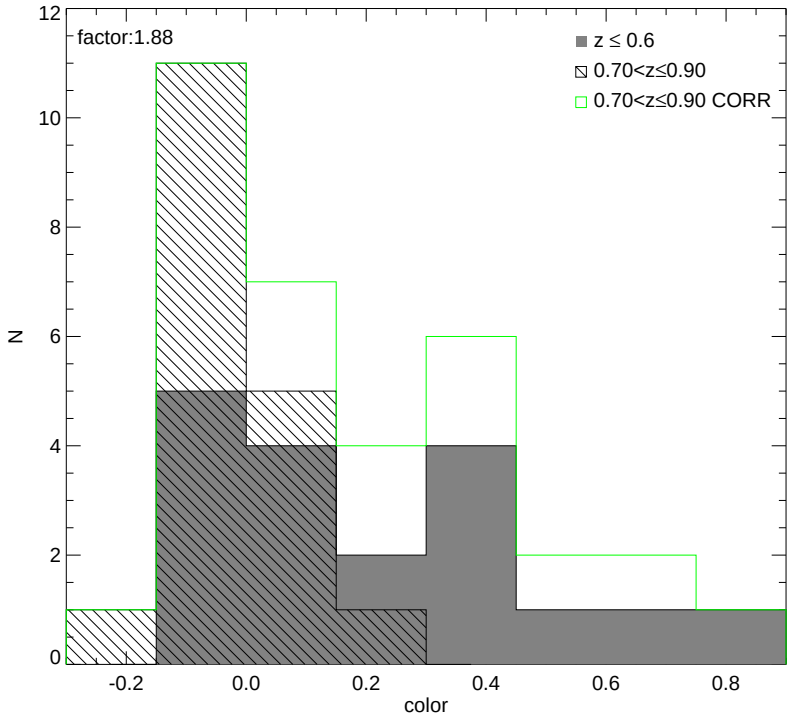

Figure 2.14: Example of how the observed color distribution (of one MC iteration) for low-s at $0.7 < z < 0.9$ (diagonal-shaded) is corrected to match the efficiency-corrected low-s color distribution at $z < 0.6$ (shaded). The final corrected color distribution for that z-bin (open histogram) has $f_b = 1.88$ more SNe than the original observed one.

Finally, errors in the efficiencies can affect the rate values. As explained in P11, those

come mainly from systematic errors in the underlying assumed Δmag distribution of SNe Ia, the distribution of residuals between the absolute magnitude of a fiducial $s = 1$ SN Ia and the magnitudes of observed SNe Ia after correction for stretch and color. To check for this systematic error, we allow for random efficiencies in the MC simulation calculated from a range of $\sigma_{int} = 0.12 - 0.15$ in the Δmag distribution, obtaining results that agree very well with the rates of Figure 2.13.

Table 2.1: Nearby low-s objects that passed the observation and fit culls used in the analysis

Name	Redshift	Stretch	Source
SN1986g	0.002	0.71	Phillips et al. (1987)
SN1990af	0.050	0.75	Hamuy et al. (1996a)
SN1991bg	0.004	0.50	Turatto et al. (1996),Filippenko et al. (1992b)
SN1992bl	0.044	0.80	Hamuy et al. (1996a)
SN1992bo	0.019	0.79	Hamuy et al. (1996a)
SN1992br	0.088	0.60	Hamuy et al. (1996a)
SN1993h	0.024	0.66	Hamuy et al. (1996a),Altavilla et al. (2004)
SN1994m	0.023	0.76	Riess et al. (1999a),Altavilla et al. (2004)
SN1995ak	0.023	0.79	Riess et al. (1999a)
SN1998bp	0.010	0.63	Jha et al. (2006)
SN1998co	0.018	0.65	Jha et al. (2006)
SN1998de	0.017	0.64	Modjaz et al. (2001)
SN1999bm	0.143	0.68	Kowalski et al. (2008)
SN1999by	0.002	0.61	Garnavich et al. (2004)
SN1999da	0.013	0.59	Krisciunas et al. (2001)
SN2000dk	0.017	0.77	Jha et al. (2006)
SN2001da	0.017	0.61	Hicken et al. (2009)
SN2002cx	0.024	0.57	Phillips et al. (2007)
SN2002hw	0.018	0.73	Hicken et al. (2009)
SN2003ic	0.056	0.77	Hicken et al. (2009)
SN2003iv	0.034	0.74	Hicken et al. (2009)
SN2005am	0.008	0.71	Hicken et al. (2009),Li et al. (2006a)
SN2005bl	0.024	0.60	Taubenberger et al. (2008)
SN2005hf	0.043	0.76	Hicken et al. (2009)
SN2005ke	0.005	0.69	Hicken et al. (2009)
SN2005mc	0.025	0.69	Hicken et al. (2009)
SN2006ak	0.038	0.78	Hicken et al. (2009)
SN2006al	0.068	0.78	Hicken et al. (2009)
SN2006br	0.025	0.78	Hicken et al. (2009)
SN2006bw	0.030	0.71	Hicken et al. (2009)
SN2006bz	0.028	0.53	Hicken et al. (2009)
SN2006gj	0.028	0.71	Hicken et al. (2009)
SN2006gt	0.045	0.53	Hicken et al. (2009)
SN2006hb	0.015	0.69	Hicken et al. (2009)
SN2006je	0.038	0.48	Hicken et al. (2009)
SN2006mo	0.037	0.73	Hicken et al. (2009)
SN2006n	0.014	0.77	Hicken et al. (2009)
SN2006nz	0.038	0.62	Hicken et al. (2009)
SN2006ob	0.059	0.75	Hicken et al. (2009)
SN2006td	0.016	0.79	Hicken et al. (2009)
SN2007al	0.012	0.47	Hicken et al. (2009)
SN2007au	0.021	0.67	Hicken et al. (2009)
SN2007ax	0.007	0.53	Hicken et al. (2009)
SN2007ci	0.018	0.79	Hicken et al. (2009)

Table 2.2: Nearby non-Ia SNe with acceptable SN Ia SiFTO fits, enough data coverage and fitted $s \leq 0.8$.

Name	Type	Redshift	Stretch	Source
SN1999eu	SNIIP	0.004	0.45	Pastorello et al. (2004)
SN2001b	SNIb	0.005	0.60	Tsvetkov (2006a)
SN2002ao	SNIbn	0.005	0.54	Pastorello et al. (2008b)
SN2002ap	SNIc	0.002	0.68	Gal-Yam et al. (2002b); Foley et al. (2003); Yoshii et al. (2003)
SN2003jd	SNIc	0.019	0.73	Valenti et al. (2008)
SN2006aj	SNIc	0.033	0.73	Pian et al. (2006); Sollerman et al. (2006)

Table 2.3: Culls applied to the training sample

Cull	**Number**			
	confirmed SNe Ia(low-s)		confirmed CC-SNe(low-s)	
	low-z	SNLS	low-z	SNLS
None	246(57)	112(3)	37(12)	47(9)
observation	207(44)	106(3)	14(6)	21(4)
$\chi^2_{\rm SiFTO}$ and snakes	184(41)	97(3)	2(2)	1(0)

Table 2.4: Culls applied to the SNLS sample

Cull	**Number**			
	all	low-s	confirmed SNe Ia	confirmed CC-SNe
None	5234	1497	407	86
observation	2615	837	343	62
$\chi^2_{\rm SiFTO}$	1054	144	338	22
$\chi^2_{\rm estimate\_sn}$	925	118	329	8
$\chi^2_{f,\rm estimate\_sn}$	848	109	303	5
snakes	710	70	295	1
FINAL	710	70	295	1
$z < 0.6$	174	18	118	0

Table 2.5: SNLS low-s candidates at $z \leq 0.6$

Name	Redshift Source	Redshift	Stretch	Colour
06D1ji	$z_{\rm hostphot}$	0.36 ± 0.05	0.66 ± 0.05	0.51 ± 0.19
04D2bt	$z_{\rm SNspec}$	0.22 ± 0.00	0.79 ± 0.04	0.24 ± 0.02
04D3df	$z_{\rm SNspec}$	0.47 ± 0.01	0.78 ± 0.02	0.05 ± 0.02
05D3jt	$z_{\rm hostphot}$	0.49 ± 0.07	0.74 ± 0.05	0.36 ± 0.13
06D3dh	$z_{\rm hostphot}$	0.44 ± 0.09	0.66 ± 0.19	0.89 ± 0.15
06D3ft	$z_{\rm hostphot}$	0.42 ± 0.08	0.73 ± 0.04	0.39 ± 0.13
05D3dw	$z_{\rm hostphot}$	0.45 ± 0.09	0.73 ± 0.03	0.12 ± 0.08
06D3dj	$z_{\rm hostphot}$	0.44 ± 0.09	0.68 ± 0.12	0.67 ± 0.13
03D4gi	$z_{\rm hostspec}$	0.58 ± 0.00	0.76 ± 0.04	0.12 ± 0.08
06D4gt	$z_{\rm hostphot}$	0.59 ± 0.10	0.71 ± 0.03	-0.05 ± 0.07
05D4ff	$z_{\rm SNspec}$	0.40 ± 0.00	0.76 ± 0.02	-0.02 ± 0.02
04D4ms	$z_{\rm hostspec}$	0.57 ± 0.00	0.63 ± 0.08	0.02 ± 0.06
03D4ah	$z_{\rm hostphot}$	0.40 ± 0.05	0.74 ± 0.05	0.36 ± 0.13
04D1po	$z_{\rm hostphot}$	0.54 ± 0.07	0.69 ± 0.04	0.31 ± 0.14
04D4hx	$z_{\rm SNspec}$	0.55 ± 0.01	0.74 ± 0.03	0.26 ± 0.06
05D3cn	$z_{\rm hostphot}$	0.13 ± 0.03	0.80 ± 0.02	-0.00 ± 0.06
06D1ce	$z_{\rm SNphot}$	0.58 ± 0.10	0.79 ± 0.02	-0.03 ± 0.06
07D3ek	$z_{\rm SNphot}$	0.57 ± 0.10	0.78 ± 0.02	-0.05 ± 0.06

Table 2.6: Volumetric rates for the subluminous SNe Ia in the SNLS. First and second column show the redshift at the middle of the bin and the mean redshift respectively. The third column is the number of objects per z-bin and the fourth is the mean weight ($w_i = (1+z_i)/(\epsilon_i \times \Delta T_i)$, where ϵ_i is the efficiency) used for the Poisson errors. Fifth column indicate the measured rate with statistical weighted Poisson errors, and sixth column the Monte-Carlo rates with weighted Poisson, Monte-Carlo and contamination errors. The seventh column shows the correction factor (with errors) applied to get the last column high-z rates corrected for the color distribution at $z < 0.6$.

$z_{\rm mid}$	$< z >$	N	$< w >, \sigma_w$	$r_{\rm meas}$ ($10^{-5}{\rm yr}^{-1}{\rm Mpc}^{-3}h_{70}^3$)	$r_{\rm MC}$ ($10^{-5}{\rm yr}^{-1}{\rm Mpc}^{-3}h_{70}^3$)	$f_{\rm corr}$	$r_{\rm corr}$ ($10^{-5}{\rm yr}^{-1}{\rm Mpc}^{-3}h_{70}^3$)
0.20	0.17	2	1.40, 0.75	$0.46^{+0.68}_{-0.31}$	$0.42^{+0.61}_{-0.28}({\rm stat})^{+0.01}_{-0.17}({\rm MC}) \pm 0.08({\rm cont})$	–	–
0.40	0.43	9	1.08, 0.24	$0.74^{+0.41}_{-0.28}$	$0.51^{+0.30}_{-0.21}({\rm stat})^{+0.16}_{-0.08}({\rm MC}) \pm 0.14({\rm cont})$	–	–
0.60	0.63	19	1.16, 0.21	$0.65^{+0.19}_{-0.15}$	$0.49^{+0.20}_{-0.16}({\rm stat})^{+0.12}_{-0.10}({\rm MC}) \pm 0.19({\rm cont})$	1.42 ± 0.20	$0.69^{+0.35}_{-0.29}$
0.80	0.78	18	1.44, 0.65	$0.44^{+0.15}_{-0.11}$	$0.40^{+0.24}_{-0.19}({\rm stat})^{+0.11}_{-0.18}({\rm MC}) \pm 0.20({\rm cont})$	1.89 ± 0.26	$0.75^{+0.51}_{-0.43}$
0.95	0.94	11	2.37, 3.02	$0.48^{+0.30}_{-0.20}$	$0.27^{+0.29}_{-0.19}({\rm stat})^{+0.18}_{-0.18}({\rm MC}) \pm 0.15({\rm cont})$	1.82 ± 0.40	$0.49^{+0.62}_{-0.40}$

2.4.3 Contamination uncertainties

An important systematic error comes from core-collapse SNe mimicking the LC of low-s SNe Ia. In P11, a missclassification fraction of less than $\leq 3\%$ was found for the normal-s population. We expect this fraction to be higher for low-s SNe Ia due to two effects. First, they are dimmer, and more easily confused with the intrinsically fainter CC-SNe at a given redshift. Second, as we probe higher redshift ranges, CC-SNe at low-z might masquerade as low-s SNe Ia at higher-z since we do not have spectroscopic redshifts for all candidates. SNe II have characteristic LCs that are very different from SNe Ia and present less danger of contamination. SNe Ib/c, on the other hand, represent a smaller fraction of CC-SNe, $\sim 30\%$ according to Cappellaro et al. (1999); Smartt et al. (2009) and 25% according to Li et al. (2010a), but are more similar to SNe Ia and will be the most probable contaminants.

The first error –where the photo-z is correct, yet the fit of a SN Ia template manages to pass the quality-of-fit cuts– can be examined using the training sample (as in §4.2). We found a 6% CC-SN missclassification rate, all SNe Ib/c. This fraction can be propagated to higher redshift using the SN Ia rate evolution of P11, $R_{Ia}(z) \propto (1+z)^{\alpha_{Ia}}$ with $\alpha_{Ia} \simeq 1.91$, and a CC-SN rate evolution reflecting the star formation rate from Hopkins & Beacom (2006), $R_{CC} \propto (1+z)^{\alpha_{CC}}$ with $\alpha_{CC} \simeq 3.6$. We assume a ratio of SNe Ia to CC-SNe of ~ 0.22 at $z = 0.3$ from Bazin et al. (2009), which translates to a local ratio of ~ 0.39 – as compared to ~ 0.48 found by Cappellaro et al. (1999) and 0.24 from Li et al. (2010a) –. The percentage fraction of contamination as a function of z, $f_{\rm cont}(z)$, can then be described as:

$$f_{\rm cont}(z) = \frac{N_{\rm passcont}(z)}{N_{\rm pass}(z)} = \frac{1}{1 + 0.39\, r\, (1+z)^{\alpha_{\rm Ia} - \alpha_{\rm CC}}}, \tag{2.4}$$

where $r = 0.88/0.06$ is the cull passing efficiency (the probability of a SN passing all selection criteria) ratio of Ia with respect to CC, assuming it does not evolve with z. This equation allows us to get a crude estimate of the number of contaminants that would pass all cuts, $N_{\rm passcont}(z)$. By dividing the expected fraction of contaminants per z-bin by the mean weight of low-s SNe found therein (per MC simulation), we translate this into a rate error lower than 20% for $z < 0.6$ up to as high as 30% at $z \simeq 0.9$. The estimates are sensitive to the power law of the rate evolution, the initial fraction of SNe Ia to CC-SNe and the local missclassification fraction of 6%. Increasing this latter fraction to 10% or using SN Ia to CC-SN local ratio of $0.241^{+3.7}_{-3.8}$ by Li et al. (2010a) instead, we obtain contamination percentages up to 30% for $z < 0.6$ and 40% at $z \simeq 0.9$.

As will be seen in next section, the rate evolution of the low-s objects is flatter than the normal SN Ia population; if we use that power-law instead, i. e. $\alpha_{\rm Ia}^{\rm low-s} = -0.34$ and a local fraction of low-s SN Ia of 21.9% (see next section), we obtain a contamination rate of approximately

40% at $z = 0.6$ up to 60% at $z = 0.9$ (see Table 2.7). This latter rate error from contamination is added in Table 2.6 and we believe it to be an upper limit. The contamination error is smaller than the combined statistical and MC errors at $z < 0.6$ but becomes comparable at higher-z. One should note that the missclassification error increases with redshift and would only make the rate higher than the actual one.

Table 2.7: Estimated core-collapse contamination percentages per redshift (from Eq. 2.4) for the low-s sample assuming a normal and low-s SN Ia rate evolution. A local 6% contamination is assumed

Redshift	0.15	0.25	0.35	0.45	0.55	0.65	0.75	0.85	0.95
normal-s evolution (%)	13	15	17	18	21	23	26	27	30
low-s evoltuion (%)	15	19	27	29	35	41	47	51	57

The second source of contamination comes from uncertainties in the photo-z. Incorrect redshift estimates can cause low-z CC-SNe to resemble low-s SNe Ia at high-z. This effect can be tested by running all spectroscopic objects through our selection criteria with their calculated photo-z instead of the spec-z. By doing this, we retain most of our candidates with a similar fit stretch and, most importantly, we still reject all the CC-SNe as contaminants (even though their photo-z was calculated with SN Ia templates and can occasionally be very different from the spec-z).

Perhaps the most concerning signature of contamination is the low-s SN Ia sample at $z > 0.6$. These have rather blue colors and could be CC-SNe instead. As an additional test, we analyzed the host galaxy properties (Figure 2.15). In general these objects are found in massive and passive galaxies, not characteristic of CC-SNe. This provides evidence that most of these candidates, including the $z > 0.6$ population, are likely the actual blue tail of the low-s SN Ia distribution, as mentioned earlier.

Nevertheless, two of these objects, 05D3hp (with $s = 0.59 \pm 0.04$ and $c = -0.16 \pm 0.09$) and 07D2bc (with $s = 0.72 \pm 0.04$ and $c = -0.13 \pm 0.03$), have unusually blue colors at very low-stretch. The host of 05D3hp is small ($M = 10^{7.9} M_{\odot}$) and star-forming ($\mathrm{SFR/mass} = 10^{-9.8} M_{\odot}\mathrm{yr}^{-1}$) and points rather towards a CC event imitating a low-s SN Ia. 07D2bc happened also in a star-forming ($\mathrm{SFR/mass} = 10^{-10.0} M_{\odot}\mathrm{yr}^{-1}$) but rather massive galaxy ($M = 10^{11.0} M_{\odot}$). If these two objects are CC-events, they would constitute a $\sim 5\%$ contamination fraction. Although it is dangerous to assume the local star formation from general galaxy properties, if we were to assume that all events in "burst" hosts with $\mathrm{SFR/mass} < -9.5 M_{\odot}\mathrm{yr}^{-1}$ are contaminants, then $\sim 30\%$ of the $z > 0.6$ objects are missclassified ($\sim 25\%$ at $z \leq 0.6$), in agreement with our generous estimates.

2.5 Discussion

We now turn to the interpretation of the low-s SN Ia rate in the light of suggested rate models, and compare it to different stretch populations. We investigate the empirical two-component rate evolution model of Mannucci et al. (2005) and Scannapieco & Bildsten (2005) but also study simple delay-time distributions (Dahlen & Fransson 1999; Strolger et al. 2004) for SN Ia progenitors. A local low-s rate estimate based on nearby studies helps constrain the models.

2.5.1 Low-z subluminous rate

Recently, Li et al. (2010b) have calculated a low-redshift SN Ia rate and a corresponding $17.9^{+7.2}_{-6.2}\%$ fraction of 91bg-like objects (Li et al. 2010a). To obtain a rough local rate estimate of low-s SNe Ia defined according to our study, i.e. $s \leq 0.8$, we use their luminosity-function sample (Table 3 of Li et al. 2010a) and directly fit objects for which we have photometric data (48 of 74) with SiFTO. For the rest we fit instead their closest R-band LC template match (column 11). Using the completeness-corrected numbers (column 9), we obtain 16.4 objects with $s \leq 0.8$, or a $21.9^{+6.9}_{-5.4}\%$ fraction. This fraction is complete within a volume of 80 Mpc and translates to a low-s rate of $(6.3 \pm 1.8) \times 10^{-6} \mathrm{yr}^{-1} \mathrm{Mpc}^{-3} h_{70}^3$ based on the local rate of Li et al. (2010b) (adjusted for $h_{70} = 1$) and including the uncertainty from the Poisson error. We note that by using the whole low-z training sample of §4.2, the 41 low-s objects correspond to a 22% fraction of the total, in good agreement.

This rate estimate is based on small sample statistics and suffers from the biases that arise from a distance-limited host-targeted survey, where the rate of SNe is converted to a volumetric rate via the galaxy luminosity function. This can lead to systematic errors, as brighter galaxies may contain more SNe Ia of a certain type (as is expected for low-s). However, a local low-s rate estimate is a valuable tool for comparison to the high-z rates.

2.5.2 Power-law evolution

The low-s SN Ia rate, as opposed to the normal-s population, does not seem to increase with redshift and follow the star formation history (SFH) trend found in P11 (Figure 2.13). If we fit a simple power-law, $r \propto (1+z)^{\alpha}$, to the SNLS rate to $z = 0.6$ and the low-z estimate, we obtain $\alpha = -0.90 \pm 1.38$, smaller than the value of the normal-s population found by P11 ($\alpha_{\mathrm{normal}} = 1.91 \pm 0.24$). This means that an evolution similar to the normal-s population is rejected with $\sim 94\%$ probability. If we include the corrected $z > 0.6$ SNLS points, we find a higher slope more consistent with zero: $\alpha = -0.34 \pm 1.41$, and we cannot reject an increasing rate similar to the normal-s.

2.5.3 Delayed component model

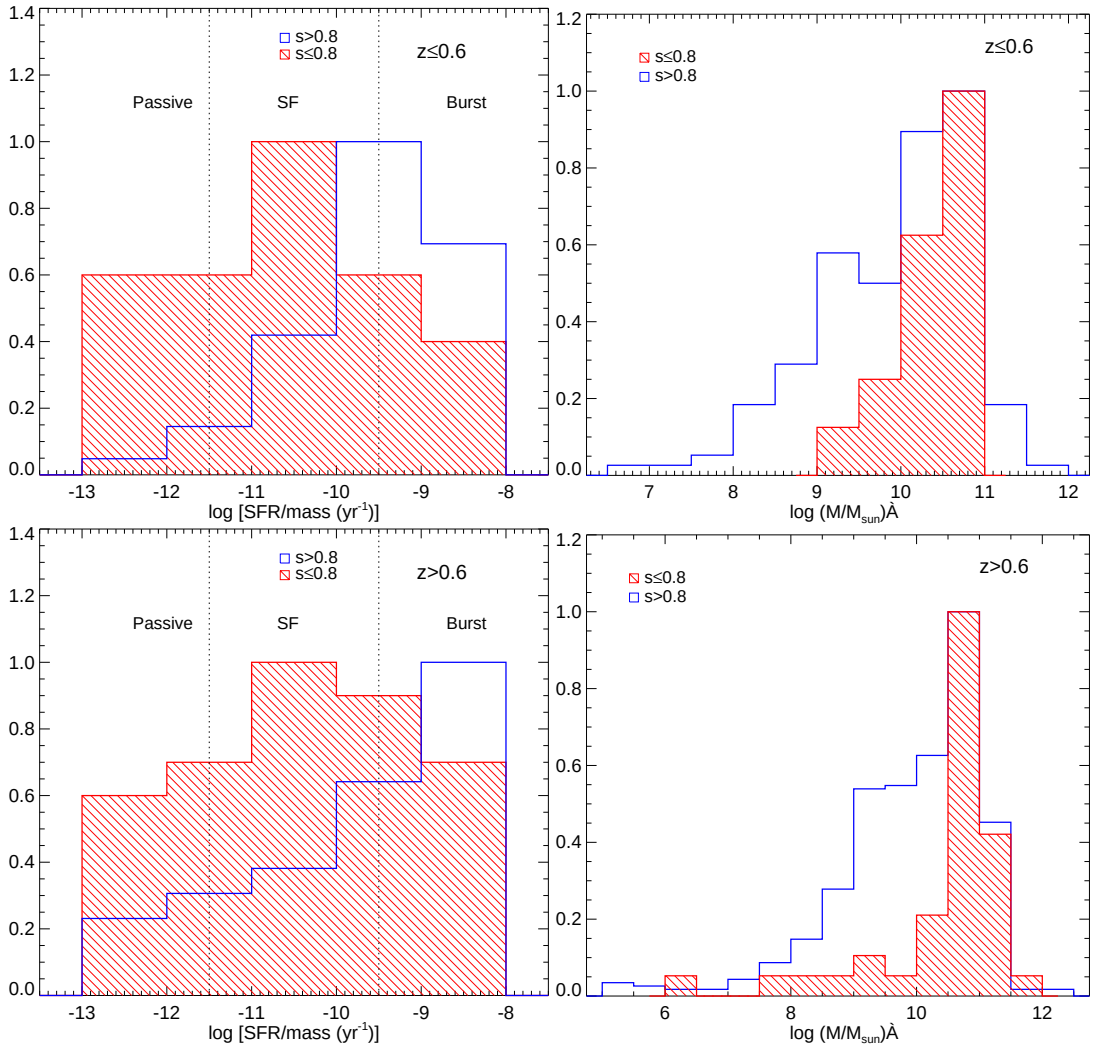

Figure 2.15: Host properties for $z < 0.6$ (*upper*) and $z > 0.6$ (*lower*) SN Ia candidates. *Left:* Normalized specific star formation (star formation per unit mass) distribution divided in normal-s (blue) and low-s (red) populations. The probability that the two populations are drawn from the same distribution (KS-statistic) is less than $\sim 0.5\%$ for both redshift ranges. *Right:* Normalized host stellar mass distribution per stretch range, normal-s (blue), and low-s (red). The KS-statistic is below $\sim 7\%$ for both redshift ranges.

It is known that SNe Ia occur in both star forming and non-star forming regions, whereas low-s objects are usually found in passive ones. In the model of Mannucci et al. (2005); Scannapieco & Bildsten (2005), two populations are considered: a "prompt" component for SNe exploding in 0.1Gyr or less that is proportional to the star formation history, $\dot{M}(z)$ and a "delayed" component for events with higher delay times that is proportional to the host mass, $M(z)$. It is described as:

$$SNR_{\rm Ia}(z) = AM(z) + B\dot{M}(z), \tag{2.5}$$

where A and B are scale factors for both components. The delayed model for low-s SNe Ia is supported when one looks at the host properties of the low-s sample. CFHT Legacy Survey host galaxy broadband photometry can be fitted to several template galaxy SEDs using PEGASE/ZPEG (Le Borgne & Rocca-Volmerange 2002) to determine average galaxy star formation rates (SFRs), stellar masses and photometric redshifts (Sullivan et al. 2006b). The properties of SNe Ia are compared to their host type (see Figure 2.15) to investigate the behavior of low-s objects in contrast to the normal-s population.

We use the specific star formation rate (sSFR), the star formation per unit stellar mass, as the indicator of star formation activity, and separate the host galaxy sample in passive galaxies, $\log({\rm sSFR}({\rm yr}^{-1})) < -11.5$, weak star formers, $-11.5 \leq \log({\rm sSFR}({\rm yr}^{-1})) \leq -9.5$, and strong star formers $\log({\rm sSFR}({\rm yr}^{-1})) > -9.5$, where SFR refers to the average star formation over the last 0.5 Gyr. This approach ignores important internal variations of SF in the galaxy, as shown in Raskin et al. (2009a), and provides only a general estimate of the SF. The sSFR distribution for two different stretch ranges (left Figure 2.15), normal-s and low-s, provides clear evidence that the low-s population is less dependent on star formation. Neill et al. (2009) find that no local low-s SN Ia is found in a host with $\log({\rm sSFR}({\rm yr}^{-1})) > -9.5$. Here, we corroborate their results for high-z objects finding that only 3 (17%) at $z < 0.6$, and 11 (25%) at higher redshift, have higher mass-weighted star formation rates.

Moreover, the host mass distribution for these stretch ranges (Figure 2.15, right) shows clearly different distributions, in which low-s SNe Ia occur almost solely in massive hosts. We extend the results of Neill et al. (2009) to the distant universe: low-s SNe Ia are found mostly in hosts with masses above $\sim 10^{9.5} M_{\odot}$. For all cases, the distribution of host-galaxy mass for the two populations, normal-s and low-s, have a low two-sided Kolmogorov-Smirnov (KS) statistic, indicating a small probability that they are randomly drawn from the same distribution.

The above relations of SN Ia properties with host characteristics demonstrate that previous findings extend to the extreme of the SN Ia population at $z > 0.1$, and at the same time are a confirmation that the observed photometric low-s sample obtained is real and not strongly contaminated from core-collapse events that are only found in late-type galaxies. The distributions for the low-s sample at low- and high-z are consistent for the sSFR (KS-test of 0.9) and inconsistent for the host mass (KS-test of 0.001) but with even higher masses favored at $z > 0.6$.

These findings also provide additional support to model the low-s SN Ia rate as just an A-component. Fitting the latter to the local and SNLS and rates up to $z = 0.6$ provides $A =$

$(1.05 \pm 0.28) \times 10^{-14}\,\mathrm{SNe\,yr^{-1}}M_{\odot}^{-1}$ and is shown in Figure 2.13. If we fit both components, we obtain $A = (1.29{\pm}0.66){\times}10^{-14}\,\mathrm{SNe\,yr^{-1}}M_{\odot}^{-1}$ and $B = (-0.27{\pm}0.64){\times}10^{-4}\,\mathrm{SNe\,yr^{-1}}(M_{\odot}\mathrm{yr}^{-1})^{-1}$. When we include the corrected SNLS $z > 0.6$ points, we obtain $A = (1.14{\pm}0.61){\times}10^{-14}\,\mathrm{SNe\,yr^{-1}}M_{\odot}^{-1}$ and $B = (0.03 \pm 0.62) \times 10^{-4}\,\mathrm{SNe\,yr^{-1}}(M_{\odot}\mathrm{yr}^{-1})^{-1}$. In the latter two cases, B is close to zero ($B < 0$ is an unphysical result) suggesting that the mass component dominates over the component proportional to the star formation history.

Comparing our delayed component (for $z < 0.6$) with the normal SN Ia population, the ratio of this value to the one in P11 is $\frac{A_{\mathrm{low}-s}}{A_{\mathrm{P11}}} \simeq 30\%$, which is particularly important at low-z, where the delayed component becomes dominant. This ratio sets a constraint on the fraction of low-s progenitors.

2.5.4 Delay-time distributions

Ideally, the rate should be able to help constrain the SN Ia delay-time distribution as follows:

$$\mathrm{SNR_{Ia}}(t) = \nu \int_{t_F}^{t} \mathrm{SFR}(t')\mathrm{DTD}(t - t')dt', \tag{2.6}$$

where t' is the age of the universe, t_F the time at which the first stars formed (effectively zero for the SNLS), DTD(t_d) is the delay-time (t_d) distribution and ν is the number of SNe Ia that explode per unit stellar mass formed. This number is related to the progenitor mass range and IMF, $\Psi(M)$, as well as the efficiency η or fraction of white dwarfs that explode as SNe Ia, and the range of WD progenitor masses, $M_{\mathrm{WD}}^{\mathrm{low}}$ and $M_{\mathrm{WD}}^{\mathrm{up}}$:

$$\nu = \eta \frac{\int_{M_{\mathrm{WD}}^{\mathrm{low}}}^{M_{\mathrm{WD}}^{\mathrm{up}}} \Psi(M)dM}{\int_{0.1M_{\odot}}^{125M_{\odot}} M\Psi(M)dM} \tag{2.7}$$

Eq. 2.6 can set constraints on the progenitors through the delay-time distribution if the SFH is known. We assume here the parameterization of Li (2008), an update of Hopkins & Beacom (2006), for a Salpeter IMF (h=0.7):

$$\mathrm{SFH} \propto \frac{(0.017 + 0.13z)h}{1 + (z/3.3)^{5.3}}. \tag{2.8}$$

The choice of SFH can affect the inferred DTD, so we also use the parameterization found by Yüksel et al. (2008) with different data.

A simple parametrization power-law DTD $\propto t^n$, has been used by several authors to model the SN Ia rate. $n \simeq -1$ is obtained in the SN Ia rate studies made by Totani et al. (2008); Maoz et al. (2011, 2010); Maoz & Badenes (2010) and is consistent with the DD scenario. Pritchet et al. (2008) obtain a different power-law of $n \simeq -0.5$ investigating the SN Ia rate as a function

of sSFR in the SNLS. It is interesting to see how the sub-sample of low-s behaves, in particular as the inferred DTDs tend to have a low tail at higher delay-times (after a sharp initial peak) where the subluminous SNe Ia are expected to lie.

By fitting this model to the SNLS data up to $z = 0.6$, we obtain $n = -0.40 \pm 1.7$ reflecting the large uncertainties in the rates. With the corrected $z > 0.6$ rates, the power-law becomes $n = -0.20 \pm 0.52$. These results are consistent for both SFH considered (see Figure 2.16).

We also use the simple empirical models employed in Strolger et al. (2004): an exponential function motivated by the double-degenerate scenario (Tutukov & Yungelson 1994) and a Gaussian function motivated by a DTD with a specific delay-time (Dahlen & Fransson 1999). The Gaussian distribution can be a proper approach for sub-groups of SNe Ia, such as the low-s one, but not for the entire population, which has been shown to be either bimodal or slowly declining in time. We use the formalism of the unimodal skew-normal DTD of eq.6 of Strolger et al. (2010) as a generalization of these models encompassing a wide variety of shapes and distributions.

The model of Strolger et al. (2010) has three independent variables, which translate to a Gaussian behavior of characteristic delay-time $\tau \sim 5$ Gyr and width $\sigma \sim 2$ Gyr. Although the results are not very constraining, they agree for both SFHs considered. These fits are shown in Figure 2.16. They indicate that low-s SNe Ia come from progenitors older than ~ 2 Gyr. This sustains the argument that low-s SNe Ia come exclusively from a delayed channel of SNe Ia. Such estimates are higher than the lower delay-time limit obtained by Schawinski (2009) based on individual SN Ia studies in early-type galaxies with optical and UV-data. On the other hand, they agree with Brandt et al. (2010) who find that SDSS SNe Ia with $s < 0.92$ have delay-times of $\gtrsim 2.4$ Gyr. Fitting all points, corrected SNLS and low-z, we obtain $\tau \sim 6$ Gyr and $\sigma \sim 0.15$ Gyr instead. Nevertheless, due to the large error uncertainties, all these results are poorly constrained.

The explosion fraction is around $0.0001 - 0.0003$ low-s SNe Ia per $M_\odot$ for all models except for the power-law fit to all corrected data which is 0.001 low-s SNe Ia per $M_\odot$. These fractions are lower than for the normal-s population –generally higher than $\sim 10^{-3}$ (e.g. Dahlen et al. 2004; Maoz et al. 2010). Both populations differ by an order of magnitude which, if coming from the same mechanism (and same DTD), could be due either to a) a lower conversion efficiency η of WD into SN Ia, or b) a lower progenitor mass range, taking into account that low mass stars are more frequent, or a combination of both. If one assumes that the conversion efficiency is constant over mass –this can be the case for certain considerations of the SD and DD scenarios (Pritchet et al. 2008)– the allowed mass range of low-s SNe Ia would need to be extremely narrow. With a Salpeter IMF, and assuming that all main-sequence stars with $0.8M_\odot < M < 8M_\odot$ become WDs, the cutoff value between low-s and normal-s progenitors

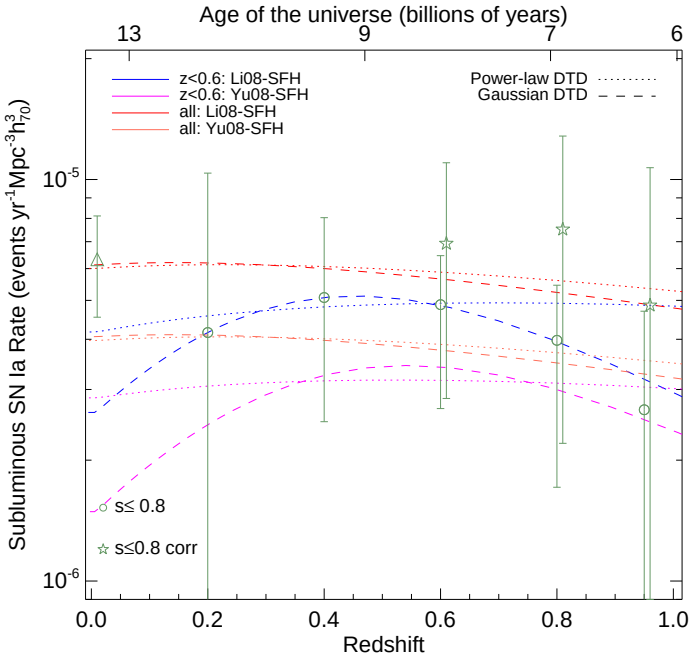

Figure 2.16: Best fit DTDs to the low-s SN Ia rate: power-law (dotted) and Gaussian behavior (dashed). Results for the SNLS up to $z < 0.6$ (and for all corrected SNLS and local) are shown for two SFHs: Li (2008) in blue (and red) and Yüksel et al. (2008) in purple (and orange).

(from Eq. 2.7) would lie at $\sim 1M_{\odot}$, an extremely narrow range of stars with too long delay-times (> 10 Gyr) to be seen at $z \gtrsim 0.3$. Changing the range of progenitors masses to $3M_{\odot} < M < 8M_{\odot}$ (Nomoto et al. 1994), the cutoff would need to be at $\sim 3.2M_{\odot}$, but these stars are too short-lived. A better constrained rate evolution of low-s compared to normal objects will potentially provide clues on the the viability of a single DTD to explain both populations and if so, their initial mass ranges.

2.5.5 Extremely low-s SNe Ia

We note that our sample does not consist of extremely subluminous SNe Ia. Looking at the local sample of typical subluminous objects, such as SN1991bg or SN1999by, the stretch is on the low end, i. e., $s = 0.5 - 0.65$. In the SNLS $0.1 < z < 0.6$ range, we only obtain one such object (see Figure 2.17), although with colors on the lower end. This SN has a spectroscopic redshift of $z = 0.57$ with LC parameters: $s = 0.63 \pm 0.08$ and $c = 0.02 \pm 0.06$. The candidate is hosted in a galaxy of mass $M = 10^{10.47} M_{\odot}$ and sSFR $= 10^{-11.93} M_{\odot}\mathrm{yr}^{-1}$, typical of very low-stretch objects.

This single SN corresponds to a single $z = 0.35$ rate of $(0.25^{+0.56}_{-0.21}(\mathrm{stat})^{+0.06}_{-0.03}(\mathrm{MC})) \times 10^{-6}\mathrm{yr}^{-1}\mathrm{Mpc}^{-3}$ (see Figure 2.18). Despite the obvious uncertainty in this number, it is tempting to argue that perhaps this "extremely low-s" population, i.e. $s < 0.65$, actually behaves differently than our

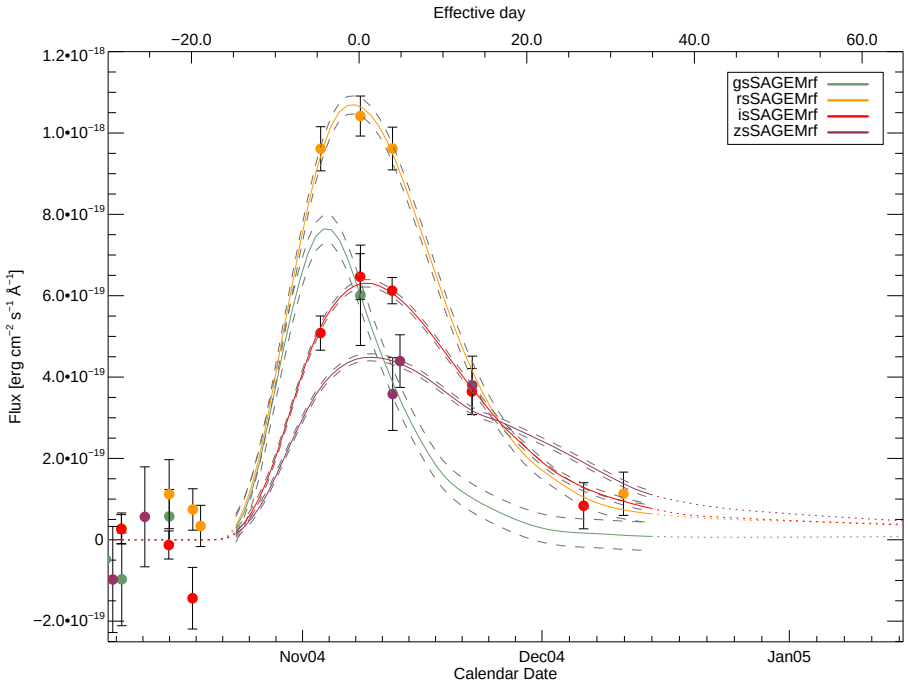

Figure 2.17: Extremely low-s candidate, 04D4ms, at spectroscopic redshift $z = 0.57$ with $s = 0.63 \pm 0.08$ and $c = 0.02 \pm 0.06$.

$s \leq 0.8$ group. If we maintain the extremely low-s definition for the local luminosity-function sample of Li et al. (2010a) as well, we obtain 5 objects with $s \leq 0.65$ (5.16 corrected for completeness with the detection efficiencies), which corresponds to $6.9^{+4.5}_{-2.9}\%$ of their rate (if we were to use the entire local sample, 15 objects have $s < 0.65$, i.e., a $\sim 9\%$ fraction), that is a rate of $(2.0 \pm 1.1) \times 10^{-6} \mathrm{yr}^{-1} \mathrm{Mpc}^{-3}$. We note that this is much smaller than the 91bg fractions generally quoted, such as the $17.9^{+7.2}_{-6.2}\%$ by Li et al. (2010a), indicating that this photometric definition is more restrictive than their definition (which is also based on spectra). Contrarily, if we were to use their fraction of "subluminous" SNe Ia to estimate the stretch limit, we would obtain $s \sim 0.75$. We emphasize therefore the importance of having a clear and consistent definition of "subluminous" SNe Ia across the redshift range. As shown in Figure 2.18, the rate evolution for this population also reveals a decline, perhaps even more rapid than for our standard low-s sample.

2.6 Summary

We have conducted a search in the SNLS for low-stretch SNe Ia, defined here as objects with $s \leq 0.8$. Typical "subluminous" surveys considered more extreme objects based also on spectroscopic features which have equivalent stretches of $\lesssim 0.72 - 0.75$. The definition chosen suits better our constructed color-stretch and magnitude-color-stretch relations trained with low-z

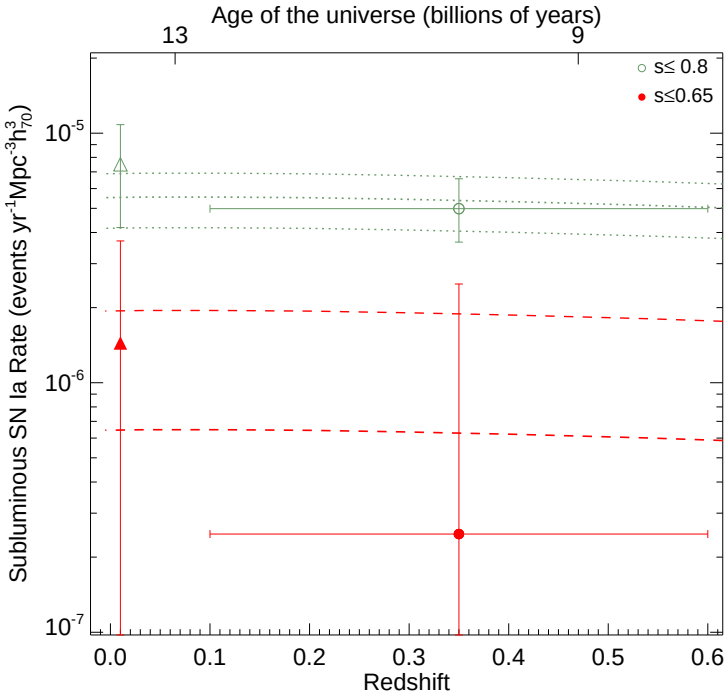

Figure 2.18: Single bin rate evolution for low-s candidates ($s \leq 0.8$) and extremely low-s candidates with $s \leq 0.65$ from the SNLS (green and red circles respectively), and the estimated fraction of the SN Ia rate from Li et al. (2010b) (triangles). Horizontal error bars indicate the width of the z-bin.

and SNLS objects. A lower transition value, nevertheless, provides also consistent LC relations. This argues for a continuous distribution of LC properties of SNe Ia, with low-s SNe Ia having distinctive redder colors and a steeper color-stretch relation. The exact stretch value at which this transition occurs is not a sharp one and lies somewhere between and $0.69 - 0.87$.

The LC relations serve for the typing of low-s SNe Ia at high redshift and for modeling the survey efficiency. We find 18 photometrically-identified low-stretch SNe Ia up to $z \sim 0.6$, indicating that the primary reason for their previous non-detections at high redshifts was due to selection effects. Most of the candidates at $z < 0.6$ have $s > 0.65$ and colors similar to the local sample. Only one of them is comparable to the faintest local counterparts such as 1991bg. The candidates are observed to be primarily hosted in passive galaxies, with no star formation, as it is found locally. The spectroscopic candidates have no conclusive features due to low signal-to-noise.

We also find a population of blue low-s SNe Ia at $z > 0.6$ hosted mostly in quiet host environments. They represent the blue end of the low-s SN Ia sample at high-redshift, whereas its reddest counterpart is not seen due to selection effects. A 30% fraction of these have unusual blue colors that are mostly attributed to the larger photometric uncertainties at high-z. Nonetheless, some of them occur in star-forming galaxies and are possible CC-SN contami-

nants ($\lesssim 10\%$). Alternatively we speculate that they could represent a different set of objects that evolve rapidly but have bluer colors than typical low-s SNe.

We calculate a rate evolution of low-s SNe Ia as a function of redshift and the results indicate a steady or slightly decreasing trend up to $z = 0.6$. We correct the rates at $z > 0.6$, where our sample is incomplete, and find the evolution to be different from the increase of the normal SN Ia population. The missclassification of CC-SNe as SNe Ia (or different unknown blue high-z transients) is an important source of systematics in the rate measurements. This would overestimate the rate and should become larger with redshift, so that the effect of a decreasing rate would be even stronger. The main findings of this study are therefore not influenced by contamination.

An A-component model, proportional to just the mass of the galaxy, is sufficient to fit the rate. This is expected as most of the candidates are hosted in passive galaxies with low star formation. Low-s SNe Ia are therefore coming from an evolved population (in massive galaxies) which corresponds to a long DTD, and could correlate with other properties such as metallicity. Alternatively, they can arise from dynamical processes as found in globular clusters, which congregate around large passive galaxies. The rate predicted by those events would be roughly constant in time, although the absolute number is different by several orders of magnitude.

As shown in Howell et al. (2007), this has consequences for cosmological studies because the relative proportion of low to high stretch SNe Ia evolves at high redshift. The present study supports their findings at the extreme low-stretch end of the population. We find that $A + B$ models have an A-component with $\sim 30\%$ coming from the low-s population.

Studies of the DTD of different scenarios help constrain progenitors masses and models, as well as the conversion efficiency of WDs into SNe Ia. The model of Strolger et al. (2010) fitted to our data agrees with a Gaussian distribution centered around $\tau \simeq 5 - 6$ Gyr, but is not very constraining. The explosion fraction for those models is $\nu \sim 10^{-3} - 10^{-4}$ low-s SNe Ia per $M_{\odot}$, an order of magnitude lower than for normal-s objects. These results again argue for the low-s being part of a delayed component. Low-s SNe Ia, together with other long delay SNe Ia of higher-s, could come from a separate progenitor channel. Although both, the SD and DD, scenarios can produce delayed SNe Ia, the merger of two low-mass WDs producing a sub-Chandrasekhar explosion seems more favorable to produce faint SNe in old stellar environments. Meng et al. (2011) show that the merger of equal-mass WDs can give rise to subluminous explosion with long enough delay-times, depending on the treatment of the common envelope phase. Nevertheless, they argue that this scenario could only account for 1% of all SNe Ia, so that other mechanisms would be necessary to explain our 7-22% subluminous fraction.

Finally, future surveys should be able to determine the rate evolution of low-s much better and to higher redshifts where the systematic errors in this study become more significant. Spectroscopic redshifts of high-z low-s SNe Ia are essential for this and could provide additional hint on their properties and their evolution. Further comparison of different SN Ia populations will give clues to understand the formation and explosion mechanisms.

Chapter 3

The Rise-Time of Normal and Subluminous Type Ia Supernovae

3.1 Introduction

Type Ia supernovae (SNe Ia) are believed to be very bright explosions of carbon-oxygen white dwarfs (WDs) in binary systems that undergo thermonuclear runaway. Despite this consensus, the nature of the companion and explosion mechanism are under debate. The enormous energy release of a SN Ia takes around 2 weeks to peak in the optical. During this early phase of the SN, when the luminosity rises to maximum, fundamental aspects of the explosion, and possibly of the progenitor, are revealed to the observer. The spectroscopic presence of intermediate mass elements such as Silicon, between carbon-oxygen and iron-peak elements, for instance, suggests incomplete burning from a subsonic deflagration component in the explosion (Filippenko 1997; Mazzali et al. 2007). A subsequent delayed detonation is typically favored to account, among others, for the energy output of SNe Ia (Khokhlov 1991; Yamaoka et al. 1992; Woosley & Weaver 1994).

The radioactive decay of the ^{56}Ni synthesized in the explosion powers the lightcurve of SNe Ia (Truran et al. 1967; Colgate & McKee 1969). It is thought that the variety in the amount of ^{56}Ni gives rise to most of the scatter in SN Ia luminosities. Values of $0.4 - 0.8 M_{\odot}$ of ^{56}Ni result in "normal" SNe Ia. "Subluminous" or 1991bg-like objects, very faint and fast evolving SNe Ia, are produced by small amounts of ^{56}Ni: $0.07 - 0.17 M_{\odot}$ (Filippenko et al. 1992b; Leibundgut et al. 1993). Slowly evolving and very bright SNe, such as 1991T are generated by $0.85 - 1.1 M_{\odot}$ of ^{56}Ni (Phillips et al. 1992). In this framework, the duration from explosion until maximum light, known as the rise-time, is partly determined by the amount of ^{56}Ni (e.g Arnett 1982; Shigeyama et al. 1992; Branch 1992; Khokhlov et al. 1993; Hoeflich et al. 1993; Domínguez et al. 2001).

The picture of the early behavior of SNe Ia has greatly benefited from the advent of improved aspherical and multi-dimensional simulations of delayed detonations (e.g Bravo & García-Senz 2008; Kasen et al. 2009; Maeda et al. 2010; Roepke et al. 2010). These authors show that the quantity of ^{56}Ni synthesized in the explosion that powers the lightcurve depends primarily on a single parameter that can be characterized by the density at which the supposed transition from deflagration to detonation in the delayed detonation framework occurs. If the amount of burning in the deflagration phase is very large (due to, for example, numerous symmetric sparks), the transition density is low and the detonation produces less ^{56}Ni. Nevertheless, other factors like the metallicity could affect the luminosity to second order (e.g Timmes et al. 2003; Gallagher et al. 2008; Howell et al. 2009; Neill et al. 2011; Bravo et al. 2010). Höflich et al. (2010), for example, predict that a dependence of the early lightcurve on the C/O ratio of the progenitor (determined mainly by the progenitor main-sequence mass) potentially affects the slope of the rise behavior at epochs earlier than 5 days before maximum.

Beyond the physics of the explosion, the rise-time study of SNe Ia can directly provide information on the progenitor system. Kasen (2010) suggests that in the single degenerate (SD) scenario, where a WD accretes material from a main-sequence or a red giant, the early phase of the lightcurve can be affected by the interaction of the companion star with the SN shock, particularly at shorter wavelengths. The magnitude depends on the observing angle, as well as on the size and separation of the companion, and can be directly tested with well sampled early rise-time data. In the double detonationof sub-Chandrasekhar mass WDs, Fink et al. (2010) predict faster rise-times for brighter and slowly declining SNe Ia. They also show that models with additional radioactive decay of other short-lived nuclei like ^{52}Fe and ^{48}Cr contribute and magnify the early epoch output of SNe Ia.

These models suggest that the lightcurve parameterization of SNe Ia could need additional corrections besides the standard width-luminosity –and color-luminosity as well as the recent host mass-luminosity (Sullivan et al. 2010; Kelly et al. 2010), especially at early epochs. The inclusion of secondary parameters that correlate with luminosity may provide an improved calibration of SNe Ia as distance indicators for cosmological studies. On the other hand, secondary parameters might not affect the luminosity directly but still be very important to understand the SNe Ia themselves.

Subluminous SNe Ia are an extremely faint population with redder colors. Standard scenarios do not reach the very faint explosions of subluminous SNe Ia and cannot reproduce their Fe- and Si-composition. Pakmor et al. (2010) propose a merger system of two WDs of similar masses ($\simeq 0.9 M_{\odot}$) that is able to account for the low ^{56}Ni mass of $\simeq 0.1 M_{\odot}$. These objects are useful to understand the amount of ^{56}Ni needed to power a lightcurve, and to investigate possible secondary effects. As subluminous SNe Ia are preferentially found in older,

more metal-rich stellar populations (Hamuy et al. 1996a; Howell 2001; González-Gaitán et al. 2011), they also offer an opportunity to study metallicity effects on the amount of ^{56}Ni produced.

The early epoch study, however, requires good early sampling of SN lightcurves. Modern rolling surveys like the Sloan Digital Sky Survey (SDSS) and the Supernova Legacy Survey (SNLS) have a better cadence and provide very well sampled pre-maximum lightcurve data, even of SNe discovered much later. Comparing fiducial stretch-corrected rise-times measured from different groups is an extremely difficult task, particularly because of the rather arbitrary definition of a fiducial, or, $s = 1$ template. Ideally, the study of several SN Ia populations, be it at varying redshift or host environment for instance, should be done with the same techniques and templates. Previous studies include the pioneering work by Riess et al. (1999b) who found a B-band fiducial rise-time of 19.5 ± 0.2 days using combined nearby data -10 days before maximum. Aldering et al. (2000) find no evidence of evolution in SN Ia rise-time and Conley et al. (2006, hereafter C06) confirmed this by calculating the rise-time of the low-z data compared with higher-z from the SNLS ($z < 0.9$) finding consistent rise-times, $19.58^{+0.22}_{-0.19}$ for the nearby and $19.10^{+0.18}_{-0.17}$(statistical)± 0.2(systematic) for the SNLS. Strovink (2007) found a fiducial rise-time of 17.44 ± 0.39 days with an algorithm that avoids external templates and fits smooth functions to the photometric data directly. Furthermore, they found individual rise-times in a bimodal distribution around 18.81 ± 0.36 days and 16.64 ± 0.21 days. Hayden et al. (2010b) propose a new parameterization of the lightcurve: they divide it into a rising and a falling component, and find a stretch-corrected rise-time of 17.38 ± 0.17 days for the SDSS, rejecting the bimodal distribution of Strovink (2007). They also find evidence for a faster stretch-corrected rise-time in slow decliners. Hayden et al. (2010a) and Bianco et al. (2011) go further to constrain the SD models of Kasen (2010) and have largely ruled out red giant companions.

None of the previous studies have included subluminous SNe Ia. In this work, we make use of the large, homogeneously observed, but intrinsically heterogeneous SN Ia sample obtained by the SNLS, in particular of the photometric group of low-stretch ($s \leq 0.8$) objects found in González-Gaitán et al. (2011). We investigate the stretch-corrected rise-time behavior of different SN Ia stretch populations to look for any secondary variations in the lightcurve besides the standard width-luminosity relation. We study the importance of different templates and lightcurve fitting techniques on the stretch-corrected final rise-time calculations. For proper comparison with other samples, we also analyze nearby and SDSS data with our own techniques. The paper is organized as follows: In § 3.2 we present the rise-time parameterization used in our study, in § 3.3 we introduce the data we used, its analysis follows in § 3.4 and comparisons between subluminous SNe Ia and other populations, as well as to previous studies are presented in § 3.5. We conclude in § 3.6.

3.2 Rise-time fit

3.2.1 Lightcurve parameterization

We follow a similar approach to C06 to measure the common stretch-corrected rise-time of our combined SN Ia sample data. We call this stretch-corrected rise-time a "fiducial" rise-time. Different SNe Ia are corrected for lightcurve (LC) shape and normalized to peak flux, after expressing all data in the same filter – normally B – via K-corrections. For the K-corrections, we use the appropriate spectral energy distribution (SED) based on the epoch, SN's redshift and LC parameters such as stretch and color. For restframe epochs (corrected by dividing by $(1+z)$) before explosion, where the flux is generally zero, the K-corrections only include the redshift term correction: $-2.5\log(1+z)$ (Nugent et al. 2002). Due to the small number of low-stretch SNe Ia available, our study of the rise-time focuses on the average properties of the aggregate stretch-corrected LCs, instead of individual rise-times.

The LC fitter used throughout this study is a modified version of the SiFTO algorithm (Conley et al. 2008; Guy et al. 2010) that uses SED templates to model SN Ia LCs. The SED sequence has been trained with low-z and SNLS data (Conley et al. 2008) and descends from the spectral sequence of Hsiao et al. (2007). The LC is parameterized with a single time-axis stretch parameter in the restframe B-band, s_B. Each observed filter is stretched differently according to a relation between the wavelength and s_B (Conley et al. 2008). The modified fitter also works well for subluminous objects (González-Gaitán et al. 2011, hereafter G11). The same SEDs are used to K-correct all data to the restframe. Observed epochs are transformed to effective dates, τ, by $\tau = (t - t_0)/s(1+z)$, where t_0 is the date of maximum flux in the restframe B-band and z is the redshift.

The LC fits normally use all available photometry, including the early time. In order not to affect the rise-time analysis, we fit the LC and calculate stretch with only photometry past a certain phase, i.e. $\tau_t < \tau < 35$ days. We call this the "core" LC. The transition value from rise-time to core LC, τ_t, considered here ranges from -10 to -8 days (see § 3.4.5). One can also use other LC parameters based uniquely on post-maximum data, such as Δm_{15} (Phillips 1993; Phillips et al. 1999). Alternatively, Hayden et al. (2010b, hereafter H10) suggest a two-stretch approach for dividing the LC fit around the epoch of maximum light τ_0. If $f(t)$ is the flux, we have:

$$f(t) = \begin{cases} f_0\, F((t-t_0)/s_r) & \text{if } t < t_0 \\ f_0\, F((t-t_0)/s_f) & \text{if } t > t_0 \end{cases} \tag{3.1}$$

where f_0 is the flux at peak (which is the same for both parts of the LC), $F(t)$ is the fiducial

($s = 1$) flux of the template, and s_r, s_f are the rise and fall stretches, respectively. This means that for the two-stretch technique, the epoch is given by $\tau = (t-t_0)/s_r(1+z)$ for pre-maximum data and by $\tau = (t-t_0)/s_f(1+z)$ for post-maximum data. In this paper, we use both the single- and two-stretch parameterizations to fit the LCs of SNe Ia.

3.2.2 Rise-time parameterization

To study the rise-time, we adopt the description used by Riess et al. (1999b); Aldering et al. (2000); Goldhaber et al. (2001) and C06. If τ is the LC phase and t_r is the fiducial rise-time of a $s = 1$ SN that we want to constrain[1], we have for the flux:

$$f(\tau) = a(\tau + t_r)^n + b, \tag{3.2}$$

for $\tau > t_r$ and b at earlier epochs. Normally, the nuisance parameter b should be zero, but we investigate possible photometric subtraction errors that could systematically shift fluxes up or down (see § 3.4.6). a is the slope of the rise and is another nuisance parameter in the fit. The quadratic form, $n = 2$, is motivated by the characteristic expansion of a hot object in the Rayleigh-Jeans tail of the SN Ia SED at early times in the B- and V-filters. The flux is proportional to the temperature and to the radius squared, the latter in a homologous expansion ($r \propto v\tau$) depending linearly on the velocity of the expansion: $f \propto r^2T \propto v^2(\tau + t_r)^2T$, where r is the radius, v the rise "speed" and T the temperature. Since $\Delta T/T$ is almost constant observationally, and $\Delta v/v$ is also close to constant at early epochs, then $f \propto (\tau+t_r)^2$. Although past studies agree that this quadratic model fits the rise-time behavior quite well, small variations among SN Ia species are possible, not only for the rise-time t_r but also for the power n of the rise. We therefore investigate such variations as well (see § 3.4.7).

3.2.3 ^{56}Ni radioactive decay

The radiated luminosity of a SN Ia is powered by the radioactive decay of ^{56}Ni through ^{56}Co to ^{56}Fe (Arnett 1982; Arnett et al. 1985; Branch 1992). At peak, this energy is still trapped in nickel and is slowly released by its radioactive decay (Nugent et al. 1995):

$$L_{bol} = \gamma \dot{S}(\tau_r) M_{\rm Ni}, \tag{3.3}$$

[1]Note that we use t_r for the average fiducial rise-time and τ_r for the individual rise-time of each SN uncorrected for stretch

where $M_{\rm Ni}$ is the mass of ^{56}Ni, $\gamma \sim 1.2$ is the ratio of bolometric to radioactivity luminosities for normal SNe Ia, and $\dot{S}$ is the luminosity from radioactivity per unit nickel mass given by:

$$\dot{S} = \left(6.31\, e^{-\tau_r/8.8} + 1.43\, e^{-\tau_r/111}\right) \times 10^{43}\, \mathrm{erg}\, s^{-1}\, M_{\odot}^{-1}. \quad (3.4)$$

This comes from the characteristic decay times of ^{56}Ni and ^{56}Co of 8.8 and 111 days, respectively, with mean energy release per decay of 1.71MeV and 3.76MeV. Therefore, by measuring the individual rise-time τ_r and bolometric luminosities L_{bol} of SNe Ia, we can estimate the amount of ^{56}Ni synthesized in the explosion under the assumed model. Variations in the amount of ^{56}Ni mass produced in the explosion will lead to changes in the rise-time for a fixed peak brightness (Contardo et al. 2000).

The value of γ is near unity but could in principle vary slightly depending on the ^{56}Ni mass, i. e. for large nickel masses, the radioactivity energy released above the photosphere will escape directly instead of remaining trapped, leading to lower values of γ. In the absence of a model for its variation, we assume $\gamma = 1.2 \pm 0.2$ (Nugent et al. 1995) and propagate this uncertainty in our calculations.

3.3 Data

3.3.1 SNLS

The five-year (2003-2008) Supernova Legacy Survey took advantage of the MegaCam wide-field imager (Boulade et al. 2003) to observe supernovae, as part of the Canada-France-Hawaii Telescope (CFHT) Deep Synoptic Survey. It used a rolling search technique suited for full coverage of the LC, including early-time, by imaging every 3-4 days (2-3 days in SN restframe) four fields in four different bands $g_M r_M i_M z_M$, which are similar to the filter system $ugriz$ of the SDSS (Smith et al. 2002). The SNLS had two independent photometric reconstructions based in Canada and France (Guy et al. 2010). We use the French photometry here, as in the SNLS cosmological analyses (Guy et al. 2010; Conley et al. 2011).

C06 used 73 spectroscopically confirmed normal SNe Ia for their rise-time study. Here, we use 30 photometrically identified low-stretch ($s \leq 0.8$) SNe Ia and 221 normal SNe Ia (González-Gaitán et al. 2011; Perrett et al. 2011) at $0.1 \leq z \leq 0.7$ to study the respective stretch-corrected rise-times and compare them. The photometric candidates went through a selection process that ensured proper redshift and stretch estimation. As part of the selection criteria to constrain the stretch, we require here good lightcurve sampling, particularly enough early data. For this, we re-fit for stretch using only data *after* τ_t, to ensure the lightcurve shape (stretch) is not affecting our rise-time estimation. We require at least two data points within

$\tau_t < \tau < 0$ days of restframe B-band maximum. The restframe B-band for these objects will be mostly mapped by r_M (and somewhat by i_M). The lightcurves must also have a good SiFTO fit with a total reduced chi-squared, χ^2_ν, better than 3.0. Additionally, we require that the error in the determination of the peak epoch be less than 0.7 days (1.2 days for the two-stretch parameterization, as shown in section 3.4.2). For the rise-time region fit, SNe Ia are required to have data prior to -10 days. These cuts reduce the sample to 134 SNe, of which 12 have $s \leq 0.8$.

In our dataset, 35% of the low-s and 74% of the normal SNe Ia have a spectroscopic redshift. The effect of having uncertain photometric redshifts can lead to considerable errors propagated in the K-corrections as well as in the effective dates τ of each SN, ultimately affecting the rise-time fit. Throughout this study, photometric redshifts are used in the same way spectroscopic redshifts are, but a proper inclusion of their errors is analyzed in § 3.4.1.

3.3.2 Low-z and SDSS

Table 3.1: Nearby objects used in the rise-time calculation. Name (column 1), redshift (column2), single-stretch (column 3), 2-s rise- and fall-stretch (columns 4 and 5), and source (column 6) are presented.

Name	Redshift	Stretch	Rise-Stretch	Fall-Stretch	Source
SN1990n	0.0034	1.07	1.18	0.96	Lira et al. (1998)
SN1994ae	0.0043	1.05	1.09	1.03	Riess et al. (2005),Altavilla et al. (2004)
SN1997bq	0.0094	0.91	1.05	0.81	Jha et al. (2006)
SN1998aq	0.0037	0.97	1.10	0.90	Riess et al. (2005)
SN2000e	0.0048	1.06	1.28	1.00	Valentini et al. (2003); Tsvetkov (2006a)
SN2001el	0.0039	0.96	1.12	0.91	Krisciunas et al. (2003)
SN2001v	0.0150	1.09	1.22	1.05	Hicken et al. (2009)
SN2002bo	0.0042	0.94	1.02	0.93	Krisciunas et al. (2004a)
SN2003du	0.0064	1.00	1.04	1.00	Anupama et al. (2005),Stanishev et al. (2007),Leonard et al. (2005)
SN2004fu	0.0092	0.90	0.99	0.84	Tsvetkov (2006b); Hicken et al. (2009)
SN2005cf	0.0064	0.98	1.03	0.96	Pastorello et al. (2007c),Wang et al. (2009b),Hicken et al. (2009)
SN2005mz	0.0176	0.63	0.91	0.53	Hicken et al. (2009)
SN2006cp	0.0223	1.05	1.11	1.02	Hicken et al. (2009)
SN2006gz	0.0237	1.22	1.30	1.19	Hicken et al. (2007)
SN2006le	0.0174	1.08	1.10	1.05	Hicken et al. (2009)
SN2007af	0.0055	0.94	1.07	0.91	Hicken et al. (2009)

To test our techniques, we also analyze available low-z rise-time data (see Table 3.1), as well as the SDSS-II SNe Ia from Holtzman et al. (2008). We can thus compare our results to low redshift to study any evolutionary effects. We cannot provide a comparison of our low-s

stretch-corrected rise-time analysis to nearby ones, as published early data for nearby $s \leq 0.8$ are scarce. The cuts applied to the SNLS are also used for the SDSS-II and low-z data, i. e. at least two data points in restframe B-band at $\tau_t < \tau < 0$ days, and at least one point before τ_t.

3.4 Analysis

3.4.1 Rise-time calculation

To make a combined rise-time study of all SNe Ia in each sample, we process each lightcurve as described in § 3.2.1. We then take the restframe B-fluxes of the low-stretch SNe Ia and overlay them on a single plot, as shown in Figure 3.1. For the rise-time region, we use early data, before a characteristic transition epoch $\tau_t = -10$ days to fit it to the model of Equation 3.2 (see Figure 3.2). Minimizing the χ^2 of the best fit model with respect to the data provides the best stretch-corrected rise-time. The choice of the transition epoch used affects the fit, as will be shown in § 3.4.5. We perform an iterative outlier rejection (similar to C06) to discard any data points that strongly deviate from the fit according to Chauvenet's criterion (Taylor 1997). For the total sample, this corresponds to 3.4σ and discards 25 (out of 449) data points, but does not affect the final fit. It is tempting to argue that some of the points in Figure 3.2 for the lo-s are above the fit (and template) and could provide evidence for interaction with a companion, as in the model of Kasen (2010). This is hard to test with the available dataset but a red giant companion has been rejected by Bianco et al. (2011) for the normal-s population.

The early time fit of the aggregate LC, nevertheless, does not take into account uncertainties in the SN fit parameters and the photometric redshift. Errors in the redshift estimate induce small changes in stretch (G11). Additionally, the use of a common SED for the LC fit as well as for the K-corrections introduces strong correlations, as do the uncertainties of maximum date and stretch of each SN fit. We handle these by shifting the photometric redshift according to its error (for those SNe Ia with photo-z) in a Monte Carlo (MC) fashion. For each new redshift a corresponding fit provides the new LC parameters (stretch, date of maximum and flux scales) and their respective errors (and covariance matrix). These values and errors, in turn, are used to generate a new set of random LC values (for SNe with and without photo-z) that determine the model SED for each epoch. The K-corrections are recalculated for the new set of redshift and LC parameters. For each of these realizations we fit the rise-time data of all SNe to the model and get the best fiducial, stretch-corrected rise-time t_r and slope a, respectively. The final values are drawn from the median of all realizations combined. The statistical uncertainties in the parameters are given by the 1σ uncertainties in the distribution (see Figure 3.3). The distribution is broader for low-s because of the smaller sample size,and

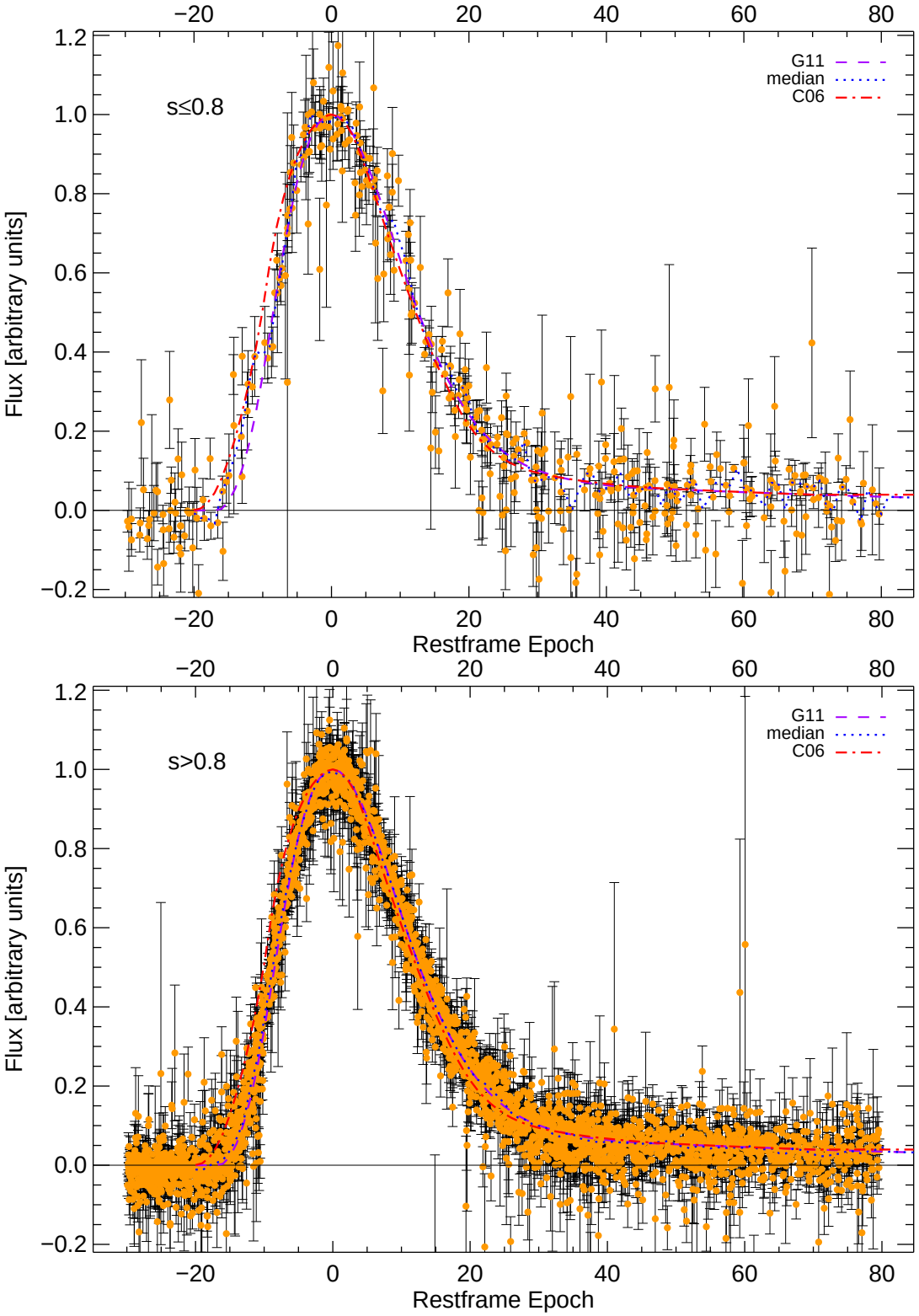

Figure 3.1: Overlaid B-band restframe lightcurves of low- ($s \leq 0.8$) and normal-stretch ($s > 0.8$) SNe Ia from the SNLS. These are K-corrected, flux normalized and scaled to s and $(1+z)$. The blue dotted line is the median of the flux points, the dashed violet line is the fiducial G11 template used, whereas the red dot-dashed is the template used in C06.

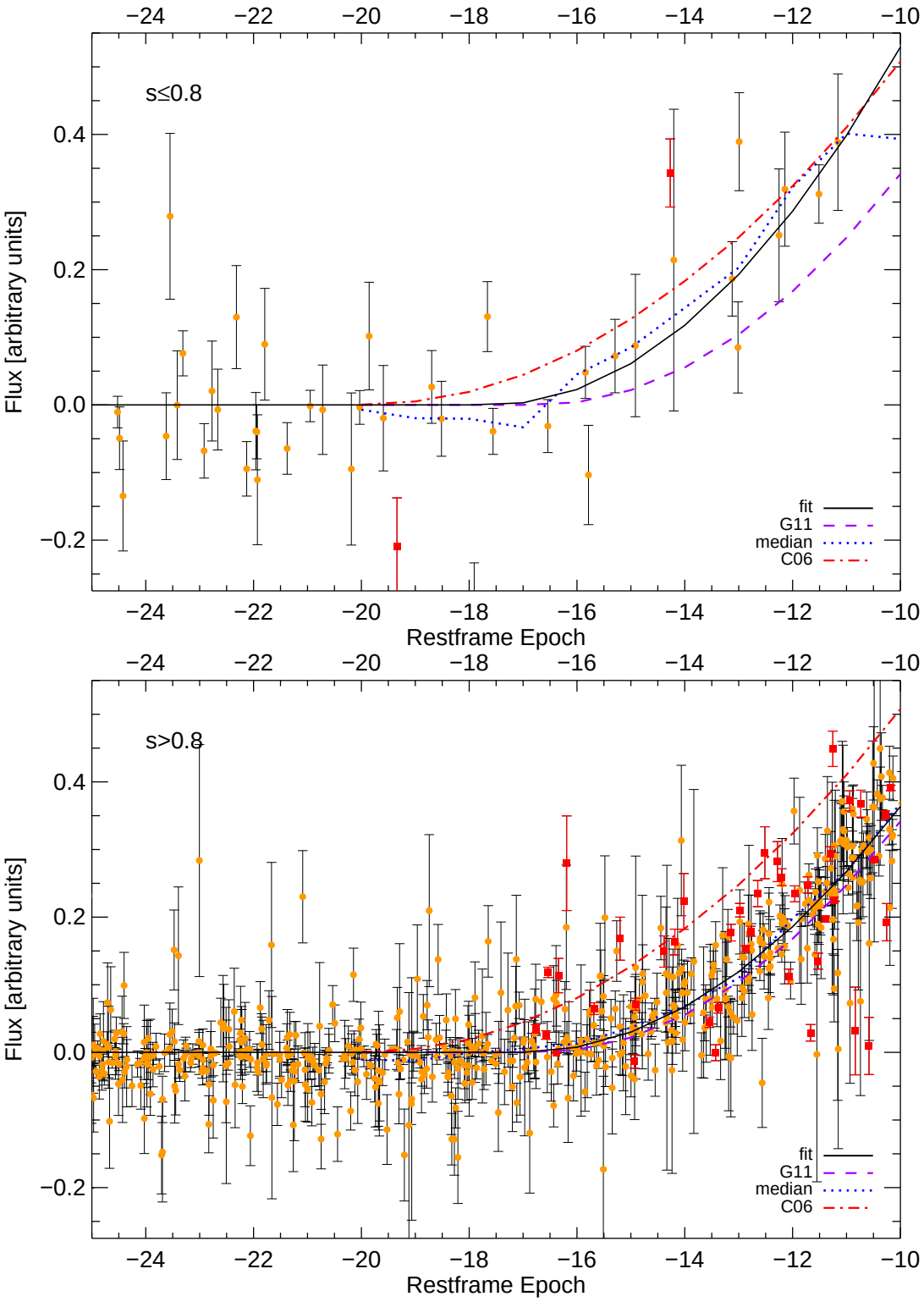

Figure 3.2: Overlaid B-band restframe lightcurves of low- ($s \leq 0.8$) and normal-stretch ($s > 0.8$) SNe Ia from the SNLS in the early rise at $\tau_t < -10$ days. Red squares are outliers from the fit ($\sim 3.4\sigma$). The solid black line is the best quadratic fit, the blue dotted line is the median of the flux points, the dashed violet line is the fiducial G11 template used, and the red dot-dashed is the C06 template.

because the low-s sample includes more SNe with photometric redshifts, and hence larger errors in z (see G11 for details).

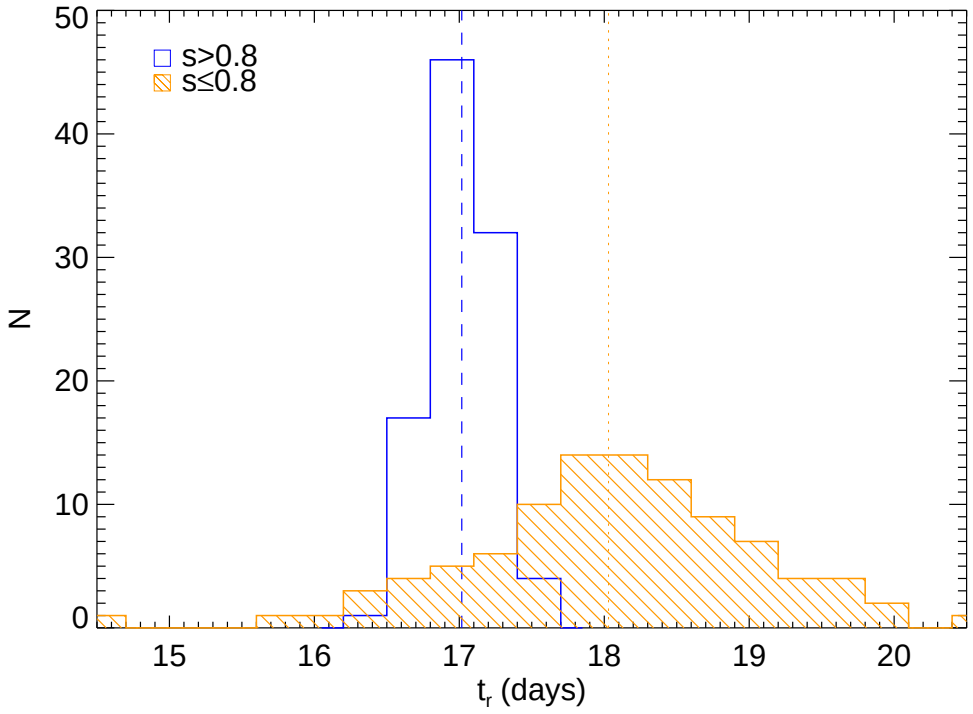

Figure 3.3: Distribution of 100 MC stretch-corrected rise-time fits to $s \leq 0.8$ (filled orange) and $s > 0.8$ (empty blue) SNe Ia. The dashed and dotted lines represent the median for both samples.

Final rise-times for the SNLS, SDSS-II and nearby samples are shown in Table 3.2. The different samples agree well with each other providing no evidence for evolution. This is confirmed by the fiducial rise-time of the SNLS SNe Ia at $z > 0.7$. Rise-times for different SNLS stretch populations after the primary LC-width, or stretch, correction are also consistent. However, the data are also in agreement at a $\sim 1\sigma$ level with a secondary slight trend for longer *fiducial* rise-times in fast decliners. High-stretch SNe ($s > 1.0$) have the shortest stretch-corrected rise-times, $\sim 1\sigma$ shorter than mid-stretch SNe ($0.8 < s \leq 1.0$), and low-stretch ($s \leq 0.8$) also seem to follow this trend. In the next sections, we investigate systematic effects that could modify these results.

3.4.2 Comparison of single- and two-stretch fits

Here, we investigate differences arising from the parameterization of the LC in two pieces (rising and falling) as in Equation 3.2.1, and as done in H10. We process our data by fitting it with a 2-s model, and we find that the rise-stretch and fall-stretch are consistent within the errors, although the average rise-stretch is slightly larger than the fall-stretch: $\langle s_r - s_f \rangle =$

Table 3.2: Stretch-corrected rise-time fit results for the single- and two-stretch lightcurve fits (with $\tau_t = -10$ days)

Sample	N_{SN}(1-s)	t_r(1-s) (days)*	N_{SN}(2-s)	t_r(2-s) (days)*
SNLS $z < 0.7$	134	$17.02^{+0.19}_{-0.26}$	87	$16.92^{+0.38}_{-0.49}$
$s \leq 0.8$	12	$18.03^{+0.81}_{-1.37}$	8	$17.89^{+1.31}_{-2.33}$
$0.8 < s \leq 1.0$	55	$17.44^{+0.45}_{-0.43}$	31	$17.56^{+0.63}_{-0.77}$
$s > 1.0$	67	$16.87^{+0.15}_{-0.25}$	48	$16.62^{+0.44}_{-0.58}$
SNLS $z > 0.7$	102	$17.11^{+0.24}_{-0.36}$	15	$16.11^{+0.68}_{-0.77}$
Nearby	16	$17.39^{+0.16}_{-0.24}$	15	$16.58^{+0.21}_{-0.27}$
SDSS-II	64	$17.44^{+0.33}_{-0.53}$	36	$17.03^{+0.26}_{-0.40}$
$0.8 < s \leq 1.0$	23	$17.78^{+0.34}_{-0.40}$	12	$17.51^{+0.31}_{-0.68}$
$s > 1.0$	41	$17.37^{+0.44}_{-0.44}$	24	$16.91^{+0.24}_{-0.48}$

*Statistical MC errors only

0.09 (RMS of 0.24). The mean rise-stretch is also larger than the stretch from the 1-s model, $\langle s_r - s \rangle = 0.06$ (RMS of 0.17) (see Figure 3.4). This can be explained as the day of maximum gets pushed to later times by more than half a day, $\langle t_0(s_r, s_f) - t_0(s) \rangle = 0.65$ (RMS of 1.77).

The mean error in the peak date is much larger for the 2-s fits, $\langle \Delta t_0(s_r, s_f) - \Delta t_0(s) \rangle = 0.87$ (RMS of 0.53) (see Figure 3.5). An incorrect estimate of the date of maximum has a direct effect on the rise-time calculation. For our MC technique, in which the fit parameters are varied according to their errors, large uncertainties in the peak epoch will affect the final rise-time even more. Our initial cut of $\Delta t_0 < 0.7$ days rejects more than 80% of the 2-s fits of the SNLS sample (40% for the 1-s fits), including all low-s objects and all $z > 0.7$ SNe Ia. We therefore relax the cut to $\Delta t_0 < 1.2$ days for the 2-s fits.

We do not change our low-s definition for the 2-s fits to $s_r \leq 0.8$ as this would reflect only the early part of the LC. If we were to use the fall-stretch instead, some low-s candidates would have even lower stretch values. Instead we note that most candidates have a mean 2-s stretch, i. e. $(s_r + s_f)/2$, closer to the single-stretch: $(s_r + s_f)/2 - s = 0.01$ with 0.05 RMS, and use this to separate the different stretch samples. This definition keeps most of the low-s candidates and is the best overall description of the lightcurve.

With the new stretch values we derived for the 2-s fits, we repeat the procedure to estimate the fiducial rise-time, using the rise-stretch instead of the single stretch values for the K-correction and normalization of all pre-maximum epochs. We obtain shorter stretch-corrected rise-times than the 1-s approach, about 1-2% for the different SNLS samples (5% for SNe Ia at $z > 0.7$), but still within the uncertainties. The decrease in fiducial rise-time with the 2-s

respect to the 1-s fit comes partially from the compensation for the higher rise-stretches measured.

The 2-s technique introduces new parameters in the fit, and we want to assess if an improvement is simply due to the increased complexity of the model, or if there is a real advantage in using it. To compare the two models, we use the Bayesian Information Criterion, $\mathrm{BIC} = \chi^2 + f\ln(N)$, a tool that gives weight to the number of parameters of the fit, f, as well as the total data used, N (Schwarz 1978). By summing all the individual core LC fits ($-10 < \tau < 35$ days) of all SNe, we find that the 1-s fit gives a smaller BICvalue: $\mathrm{BIC} = 17405$, compared to the 2-s value: $\mathrm{BIC} = 19721$ (the average χ^2 per degree of freedom for the individual 2-s fits is slightly better, $\langle\chi^2_\nu\rangle = 1.44$, than for the 1-$s$ technique: $\langle\chi^2\rangle = 1.48$), i. e. the 2-$s$ technique did not lead to a better fit once the increase in parameters is taken into account. If we only consider the rise portion of the lightcurve (for which we use the same quadratic fit for both techniques, so that BIC is unnecessary), we obtain a slightly lower chi-square per degree of freedom for the 1-s approach, $\chi^2_\nu = 1.60$, than for the 2-s fit: $\chi^2_\nu = 1.64$. The SNLS systematic uncertainties from different LC fits, 2-s and a newer SiFTO version different from G11, are shown in Table 3.3.

Similar results are found for the SDSS and low-z samples. The core LC fits are better for the 1-s fits whereas the early rise-time fit is better for the 2-s approach, according to the BIC criterion. The average rise-stretch is larger than the fall-stretch (by 0.09 for the SDSS and 0.11 for the low-z sample) partly because of a mean shift in the peak date (of 0.45 and 0.40 days for the SDSS and low-z, respectively). The mean errors in peak time are somewhat lower (0.69 for the SDSS and 0.21 for the nearby sample). The final rise-times obtained are comparable for both techniques, although the low-z 2-s result is $\sim 1.5\sigma$ lower than its 1-s counterpart.

In the present study, we do not find a significant change in the rise-times of different samples for the two parameterizations considered: 1-s and 2-s, except for the nearby set for which a $\sim 1.5\sigma$ difference is found. Our 2-s technique that is based on an adapted two-piece SiFTO fitter provides more uncertain peak date estimates. Requiring accurate maximum epochs affects the number of SNe we can use in the fit for the 2-s technique (see section 3.3). We find that using only SNe with $\Delta t_0 < 1.2$ days is good enough for the fit but the number of objects used is less than for the 1-s technique, even though we use a tighter criterium for that fitter of $\Delta t_0 < 0.7$ days.

Although the statistical analysis of the fiducial rise-time remains unchanged with the parameterization used, Figure 3.4 shows that rise- and fall-stretches in the 2-s technique do not vary equally for different SNe. The linear fits show that lower-s SNe Ia tend to have larger rise-stretches and shorter fall-stretches for their respective 1-s, a higher difference between the two, as compared to higher-s SNe Ia. The slopes of rise- and fall-stretch are different by more

than 3σ.

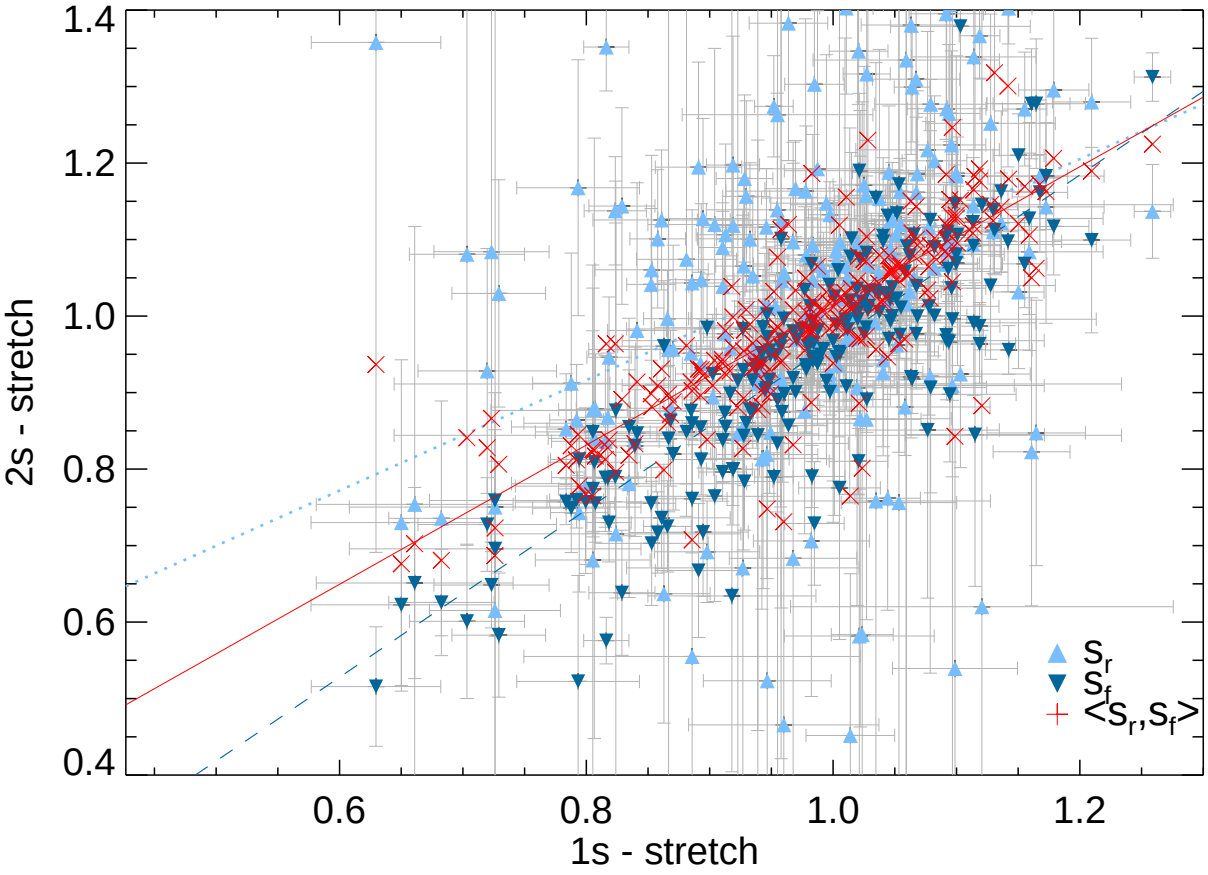

Figure 3.4: Comparison of rise- (light blue triangles) and fall-stretch (dark blue inverted triangles) for SNLS SNe Ia calculated with the two-stretch technique as a function of the single-stretch. The crosses are the mean of the rise- and fall-stretches. The lines are linear fits: solid (red) for the mean of rise- and fall-stretches (slope: 0.91 ± 0.08), dotted (light blue) for rise-stretch (slope: 0.72 ± 0.07) and dashed (dark blue) for the fall-stretch (slope: 1.09 ± 0.04).

3.4.3 Comparison of different templates

The template used in C06 descended from Nugent et al. (2002) and the early portion was based on a limited number of SNe Ia. Using this template to calculate the rise-time, we obtain 19.33 days, in agreement with the result obtained in C06 of 19.10 days.

The fiducial stretch-corrected SN Ia rise-time is dependent on the SED template used (see Figure 3.6), in particular on the rather arbitrary definition of a $s = 1$ SN. This is especially important when comparing rise-times from different sources, where various templates can lead to different rise-times. A $s = 1$ SN is defined here as the mean stretch of the training sample for the template we use, which is the same as in G11. If we correct rise-time of the C06 template for the different $s = 1$ definitions, by comparing the fits directly (see Figure 3.7),

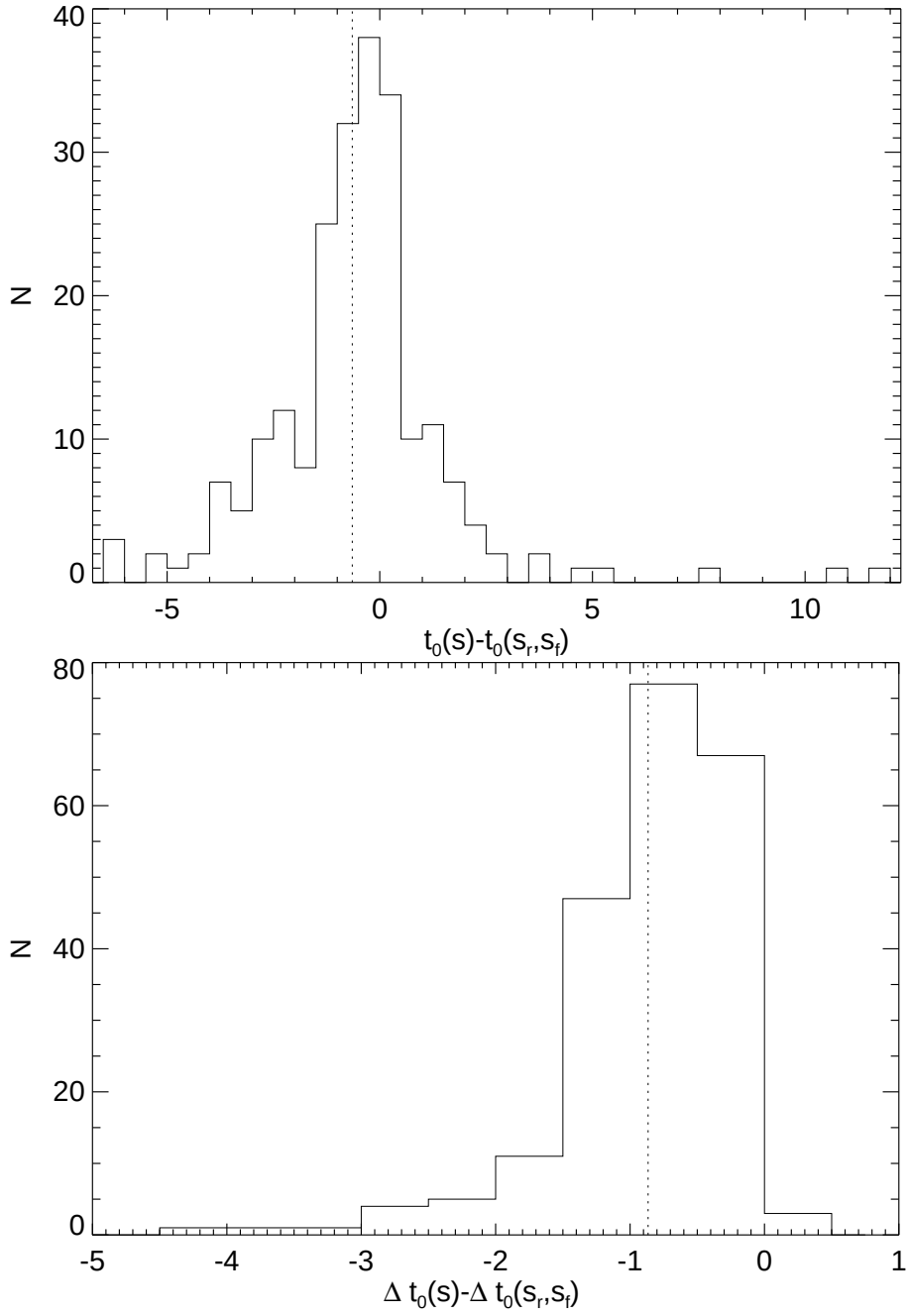

Figure 3.5: Difference of peak date (upper) and peak date error (lower) calculated with the 1-s and the 2-s techniques for the SNLS sample

Table 3.3: Stretch-corrected rise-time systematic uncertainties for the SNLS stretch samples: low-s ($s \leq 0.8$), mid-s ($0.8 < s \leq 1.0$) and high-s ($s > 0.8$) and differences between them

Systematic	**Rise-time t_r (days)**				**Difference Δt_r (days)**	
	all	low-s ($s \leq 0.8$)	mid-s ($0.8 < s \leq 1.0$)	high-s ($s > 1.0$)	low-s - mid$s$	mid-s - high-s
STANDARD	$17.02^{+0.19}_{-0.26}$	$18.03^{+0.81}_{-1.37}$	$17.44^{+0.45}_{-0.43}$	$16.87^{+0.15}_{-0.25}$	$0.59^{+0.93}_{-1.44}$	$0.57^{+0.47}_{-0.50}$
LC-FIT						
1-s new SiFTO	17.14	18.46	17.99	16.57	0.47	1.42
2-s	16.92	17.89	17.56	16.62	0.97	0.94
TEMPLATE						
NEW (conley09f)	16.94	18.33	17.70	16.59	0.63	1.11
C06 (nugent05)	18.77	20.13	19.68	18.21	0.45	1.47
SALT2	18.16	19.13	18.77	17.57	0.36	1.20
TRANSITION EPOCH						
$\tau_t = -8$d	17.22	18.68	17.56	16.95	1.12	0.61
PHOTOMETRY						
Fr phot, $b = 0$	17.21	17.96	17.40	16.96	1.02	0.44
Ca phot, free b	17.18	18.07	17.50	16.86	1.03	0.64
POWER LAW						
$n = 1.9$	16.83	17.87	17.26	16.68	0.61	0.58
$\boldsymbol{\sigma^{\rm tot}_{\rm syst}}$	$\mathbf{+1.78}$ $\mathbf{-0.23}$	$\mathbf{+2.24}$ $\mathbf{-0.22}$	$\mathbf{+2.31}$ $\mathbf{-0.18}$	$\mathbf{+1.35}$ $\mathbf{-0.45}$	$\mathbf{+0.69}$ $\mathbf{-0.27}$	$\mathbf{+1.24}$ $\mathbf{-0.13}$

*This template is based on an old limited SN sample and is not included in the final systematic error budget.

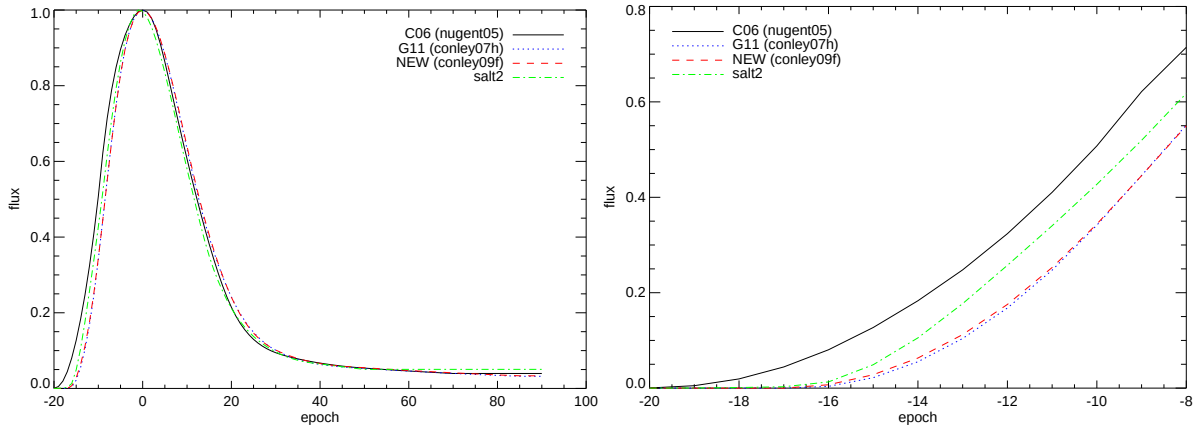

Figure 3.6: Different SN Ia light-curve templates (inset of early portion on the right): C06 (solid black), G11 (dotted blue), NEW (dashed red) and SALT2 (dot-dashed green).

i. e. a $s = 1$ SN for the G11 template corresponds to a $s = 1.03$ for the C06 template, we then obtain 18.77 days. This averaged correction partially accounts for the early wide behavior of the C06 template (see Figure 3.2). The simple change of $s = 1$ definition is not sufficient to fully compensate the effect of an incorrect early template, so that a longer stretch-corrected rise-time is still obtained. We get similar long rise-times with the C06 template applied to the 2-s technique, indicating that this parameterization is not independent of the template used.

Newer templates trained with the well-sampled data of the SNLS, like the one used in G11, or a more recent version trained with a larger sample (used for SiFTO in Guy et al. 2010), give consistent rise-times after correction for the different $s = 1$ definition. Table 3.3 shows the rise-times for different templates.

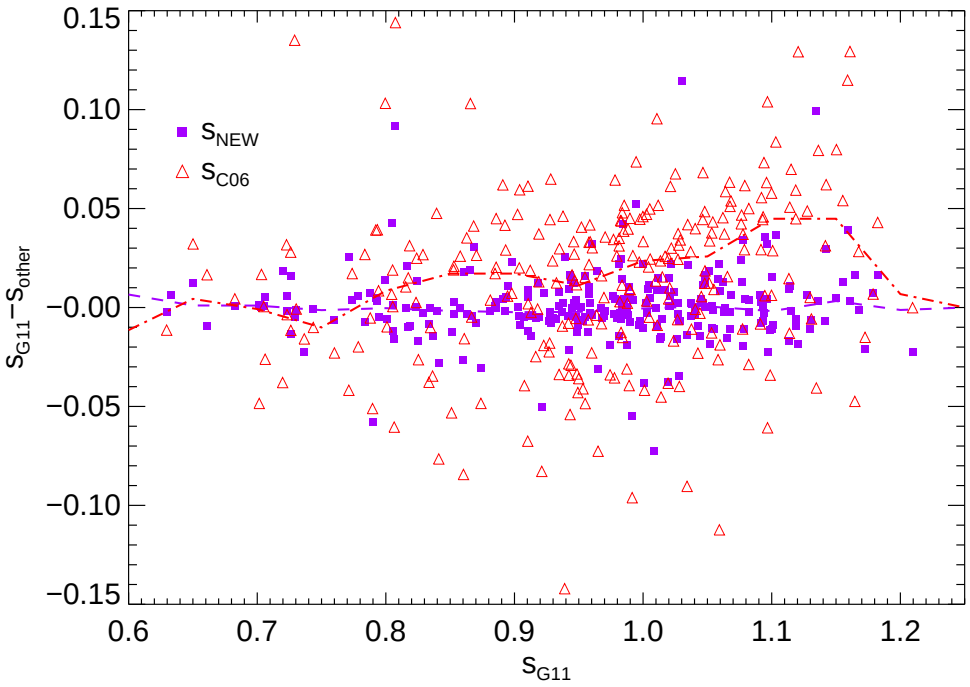

Figure 3.7: Stretch comparison between lightcurve fits of the G11 template and other templates: C06 (purple dots), and a more recent one NEW (red squares). The purple dashed and red dot-dashed lines are the averaged median in 0.05 stretch bins.

3.4.4 Comparison with SALT2

We investigate here the use of a different LC fitter, SALT2 (Guy et al. 2007). This fitter also makes use of different templates from the ones presented in the previous section, so that we are probing two systematics simultaneously.

In order to do this, we fit all SNe Ia with SALT2 in the range $\tau > -10$ days. A direct comparison of their SiFTO stretch and X_1 parameter from SALT2 is shown in Figure 3.8 through

a linear fit. We calculate restframe, stretch-corrected epochs using the redshift and a corresponding stretch (for each X1 parameter): $\tau = (t-t_0)/s(X_1)(1+z)$. Every data point matching restframe B-band is K-corrrected by taking the SED for each restframe epoch based on Eq. 1 of Guy et al. (2007) with X_0, X_1 and color obtained from the SALT2 fit, and integrating it in the appropriate filter at the proper redshift. We then fit the aggregate LC points of the early rise ($\tau < -10$ days) to the quadratic rise model.

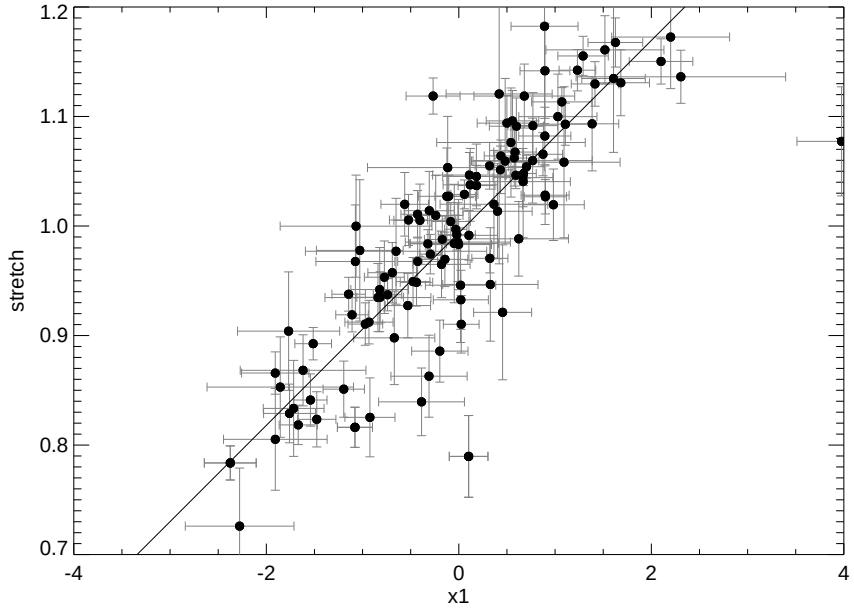

Figure 3.8: Comparison of SiFTO stretch and SALT2 X_1 for the SNLS SN Ia sample. The solid line represents the fit: $st = a \times X_1 + b$ with $a = 0.086 \pm 0.026$ and $b = 0.997 \pm 0.022$.

Similarly, we take into account errors with a MC that shifts the fit parameters ($z_{\rm phot}$ if necessary, and $\tau_{\rm max}$, X_0, X_1 and color) according to their covariance matrix, and re-calculate a stretch from this, as well as a new K-correction for each point of each simulation. The mean of all iteriations, the final fiducial rise-time we obtain for the normal-s population, is 18.16 ± 0.44 days. This is larger than ~ 1.1 days than the standard SiFTO 1-s and 2-s rise-times. Although the SALT2 template is different than the templates we use (see Figure 3.6), is is not as extreme as the C06 template. Clearly, the use of the LC fitter also affects the measured rise-time and is an important systematic. The differences between SN Ia populations are still consistent as shown in Table 3.3 (under "template", although this is a twofold systematic: "template" and "LC-fit").

3.4.5 Transition Epoch

The transition epoch is the minimum epoch used in the core LC fit and the maximum epoch allowed in the early rise-time fit. Its value can affect the quality of the fit but also the resulting

rise-time (and even the quadratic behavior of the rise). A higher value, like $\tau_t = -6$ days, increases the amount of data for the early-time fit, but the rise may no longer follow a simple quadratic relation. Figure 3.9 shows that rise-time fits with different transition times and a fixed power fit (quadratic $n = 2$) for the SNLS do not change much up to a maximum value of $\tau_t \simeq -8$ days, where the rise-time starts to diverge. We use here the standard $\tau_t = -10$ days used in other studies but add a systematic uncertainty to the rise-time based on the differences at $\tau_t = -8$ days (see Table 3.3).

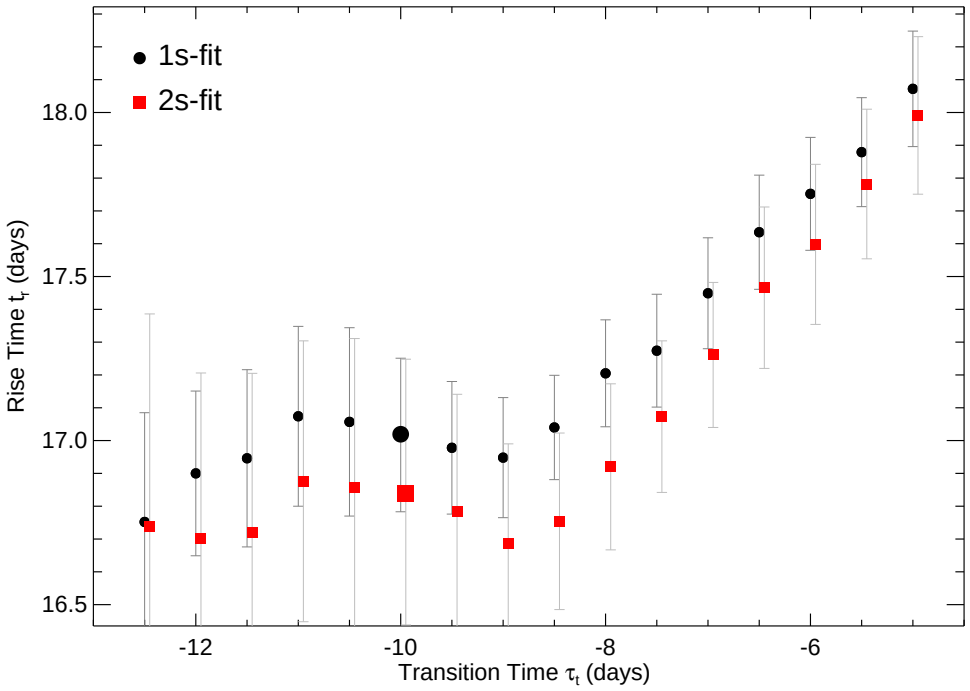

Figure 3.9: Stretch-corrected rise-time as a function of the transition epoch, the maximum date allowed in the single- (black circles) and two-stretch (red squares) rise-time fits. The rise-time errors are the MC errors calculated as in § 3.4.1. The larger points at $\tau_t = -10$days are the quoted fiducial rise-times of this study.

3.4.6 Zero scale b

Wrong photometric subtraction affects fluxes that are close to zero and strongly influences the final stretch-corrected rise-time calculation. To study this systematic error, we add a nuisance parameter, b, to the quadratic form (Eq. 3.2) that will absorb any general photometric error. For a good photometry, we should obtain b values close to zero. In our study, we get $b = (-0.48^{+0.12}_{-0.09}) \times 10^{-3}$, an off-zero value reflecting the large dispersion of the fluxes near zero (median of 3.1×10^{-4} with 0.03 RMS) but small enough to represent a negligible effect on the rise-time. Consistent rise-times are obtained with free/fixed b values for the photometry

processed via the French and Canadian reconstructions, as seen in Table 3.3.

The importance of this parameter can be observed in Figure 3.10(a), in which different b values in the range $-0.05 < b < 0.05$, or a 5% maximum shift of the normalized flux at peak, result in rise-times shifted by several days. We emphasize therefore the importance of proper photometry, well-sampled to dates even before explosion, to correctly calculate b and not affect the rise-time.

3.4.7 Different rise power laws

Other parameters that could influence the fiducial rise-time behavior are a and the rise power n in Eq. 3.2. We find $a = (7.40^{+0.58}_{-0.62}) \times 10^{-3}$ for the normal-s SNLS population (arbitrary flux units) and an assumed $n = 2$ quadratic form. If we relax the quadratic rise assumption and allow the power of the rise-time model to be free (a is free and $b = 0$), we obtain $n = 1.92^{+0.31}_{-0.37}$(stat). Rise-times fitted with this new power law are lower for all stretch populations but consistent with their quadratic equivalents.

Figure 3.10(b) shows the relation between the assumed power-law, n, and the measured stretch-corrected rise-time, t_r for the normal SN Ia sample. A higher n makes the LC rise faster. In order to compensate for this, the duration of the rise to maximum of the fit becomes longer. This effect has a high degree of degeneracy and correlation between the two fit parameters. A very similar trend is observed for the different stretch samples. Furthermore, if the quadratic form is relaxed for all populations, we obtain increasing power laws and rise time for higher-s SNe (Table 3.4). This variation shows again the clear difference in the rise-time region for the sub-samples of SNe Ia.

Table 3.4: Stretch-corrected rise-time and power-exponents fit results for the different stretch samples in the SNLS

Sample	t_r(days)*	n*
SNLS	$16.85^{+0.54}_{-0.81}$	$1.92^{+0.31}_{-0.37}$
High-s	$17.89^{+0.77}_{-0.98}$	$2.66^{+0.44}_{-0.59}$
Mid-s	$16.49^{+0.56}_{-0.88}$	$1.48^{+0.34}_{-0.37}$
Low-s	$16.14^{+1.00}_{-1.99}$	$0.78^{+0.71}_{-0.71}$

*Statistical MC errors

Although the systematic uncertainty from this variation is also highly correlated with the transition time, we still include it in the total systematic error budget.

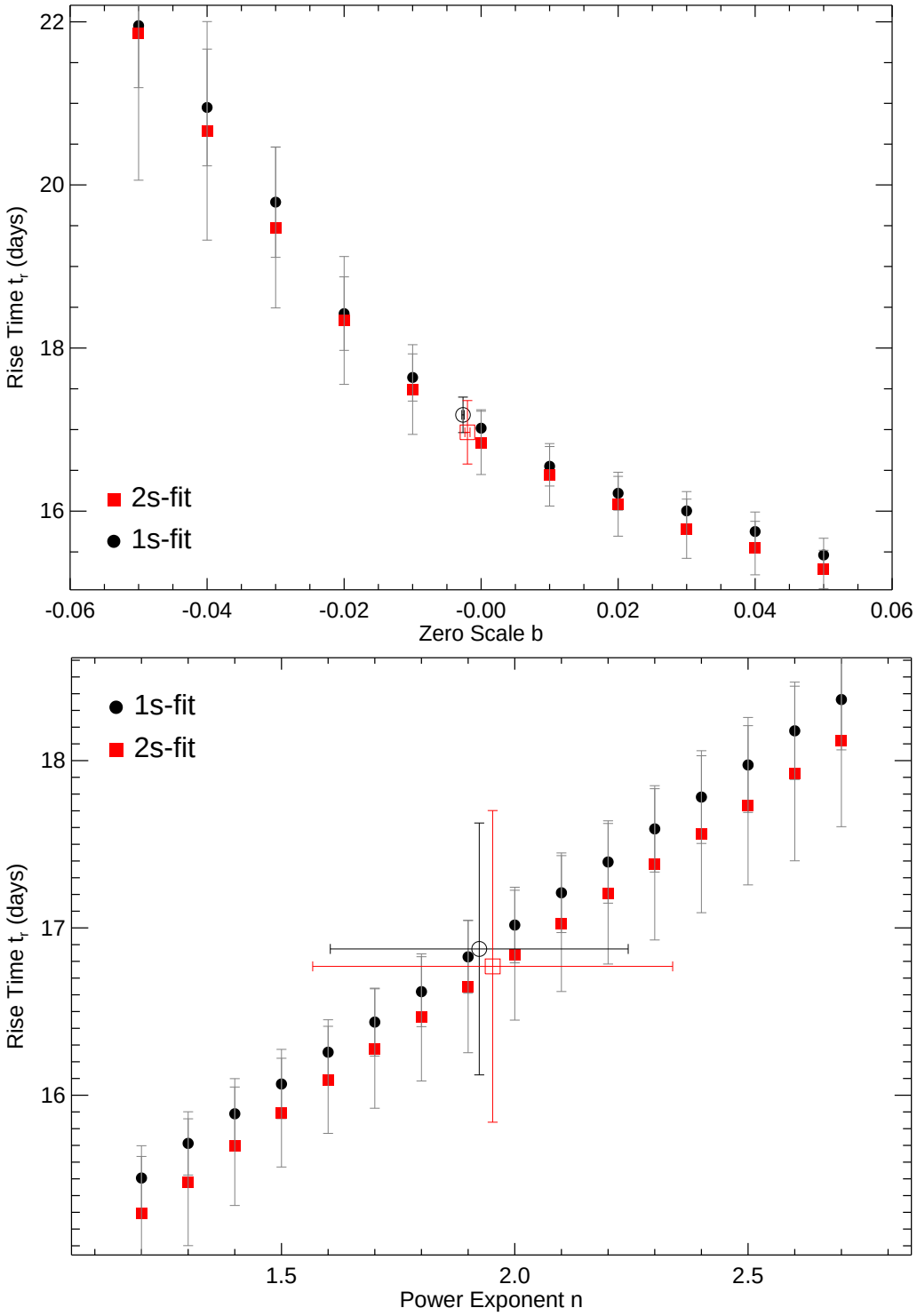

Figure 3.10: Rise-time t_r as a function of zero scale b (*upper*) and power exponent n (*lower*) of Equation 3.2, as obtained in the fits for 1-s (black circles) and 2-s (red squares) techniques (at $\tau_t = -8$ days). Errors indicate MC uncertainties (§ 3.4.1). Empty points are the best fits with b and n free, respectively (a was kept free for all fits).

3.5 Results and Discussion

The final fiducial rise-time, t_r, for all SNe Ia in the SNLS calculated via the single-stretch method is $t_r = 17.02^{+0.19}_{-0.26}(\text{statistical})^{+0.30}_{-0.23}(\text{systematic})$. The statistical uncertainty represents the 1σ distribution of the MC simulations and the systematic uncertainty comes from the different effects considered in the previous section (added in quadrature) and shown in Table 3.3. This agrees with the value found via the two-stretch technique.

We find that the fiducial stretch-corrected rise-times are consistent for fast and slow decliners, independently of different fit characteristics such as the template or lightcurve fitter. Mid-stretch SNe Ia ($0.8 < s \leq 1.0$) have a fiducial rise-time $\Delta t_r = 0.57^{+0.47}_{-0.50}(\text{stat})^{+1.24}_{-0.13}(\text{syst})$ days longer than their high-stretch counterpart ($s > 1.0$), barely a $\sim 1\sigma$ result. With even lower significance, low-stretch SNe Ia show a difference with respect to the high-stretch population of $\Delta t_r = 1.16^{+0.82}_{-1.39}(\text{stat})^{+1.42}_{-0.19}(\text{syst})$ days.

Although we do not measure individual rise-times, an estimate based on the stretch of each object can be obtained from the fiducial rise-time. For the single-stretch case we do $\tau_{r,i} = s_i \times t_r(s)$, where the subscript i denotes each individual SN and $t_r(s)$ is the fiducial rise-time. Individual rise-times for the low-s population lie in the range of 10-14 days. For the normal-s population, they lie in the range of 14-21 days. We plot them as a function of B-band magnitude at maximum and SALT2 X_1 in Figure 3.11. One can see that as τ_r is calculated from stretch, which correlates with X_1, the rise-time follows the LC-shape quite closely, while there is more scatter with maximum brightness.

3.5.1 Comparison to previous studies

As mentioned in § 3.4.3, the different definition of a fiducial $s = 1$ lightcurve across different templates makes the comparison of stretch-corrected rise-times from several studies quite difficult.

Having that in mind, recent studies (Strovink 2007; Hayden et al. 2010b), including the present one, agree that the average rise-time of SNe Ia is shorter than previously thought. With more data, better-sampled at early times, the new templates, as well as LC-fitting techniques, provide evidence for a $\sim$2 days shift in the average rise-time of SNe Ia with respect to previous studies (Riess et al. 1999b; Conley et al. 2006), although the precise value is heavily dependent on the definition of a fiducial $s = 1$ LC template.

Although we use the same technique as C06, the template they used was trained with a handful of SNe Ia and consequently had a rise-time behavior to maximum quite different from the current templates. Their rise-time is longer than the one we find here, even after correcting for our $s = 1$ definition.

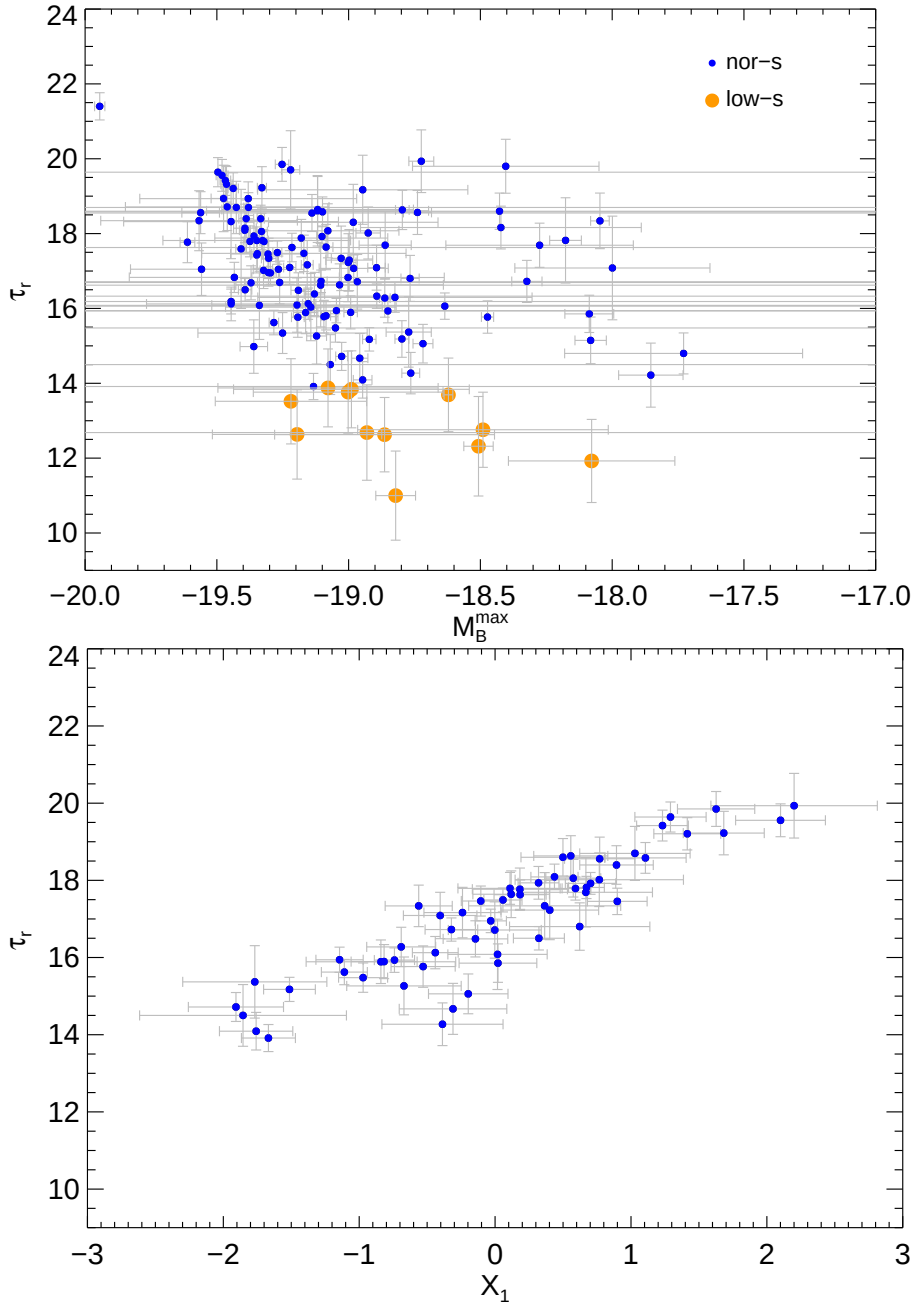

Figure 3.11: Individual rise-times as a function of B-band magnitude at maximum and X_1

We also analyze the nearby and SDSS-II datasets with our same template and LC fitter. H10 used a much larger SDSS-II sample (361 SNe) than used here (the 146 SDSS-II SNe from Holtzman et al. 2008). Our SDSS-II fiducial rise-time agrees well with theirs. They argue that the two-stretch technique presents a much better parameterization than a single parameter approach. We do not agree with those findings, neither for the SNLS nor the SDSS and low-z data. We attribute this to the use of a different fiducial LC template and fitter that differ in the rise-time region from the ones they use (G11 and modified SiFTO vs MLCS2k2, Jha et al. 2007), in particular the stretch they calculate is not based on multiple bands. The Bayesian Information Criterion for the core LC fits suggest that the inclusion of an additional parameter to model SN Ia lightcurves does not provide a valuable improvement of the fit. The quadratic fit of the early rise-time data, on the other hand, could benefit from such an independent parameterization but does not alter the average rise-time results.

Based on our calculations of the fiducial rise-time for different samples across the redshift range $0 < z < 1$, we do not find evidence for a significant evolution in the early portion of SN Ia lightcurves. Dividing the SNLS sample into three populations according to their stretch values, we measure the average rise-times for each sub-group and find them to be consistent. Although at low confidence, the data also agree with a trend of faster fiducial rise-times for brighter and slowly declining SNe Ia *after* the primary stretch correction, for the SNLS and SDSS-II. H10 obtained a similar trend for the individual rise-times of SDSS-II objects.

3.5.2 ^{56}Ni masses

In order to estimate the ^{56}Ni masses, we need to calculate bolometric luminosities. We integrate the model SEDs for each SN across all observed bands. This omits the near-infrared (NIR), which accounts for a substantial fraction of the bolometric luminosity, so we must apply a correction factor. In Howell et al. (2009) the IR percentage for normal SNe Ia is estimated via integration of proper SEDs corrected for each SN in the region outside the observed spectrum, under some assumptions. For low-s SNe Ia, SEDs are not as fully sampled. We instead use a very broad approximation based on the IR fraction found for SN1999by and SN2004eo (Höflich et al. 2002; Garnavich et al. 2004; Taubenberger et al. 2008): $\sim 15 - 25\%$. The fraction is at least 5% higher than for normal SNe Ia. We use a standard $20 \pm 10\%$ value (and $10 \pm 5\%$ for the normal-s) to calculate via Equations 3.3 and 3.4 the ^{56}Ni mass.

In order to account for the errors in the LC parameters, we carry out this computation for every realization of the LC data in the MC of § 3.4.1, and use the median L_B of each SN to calculate the final ^{56}Ni masses, as shown in Figures 3.12 and 3.13. We also include the error on the conversion factor γ, which can also slightly vary with ^{56}Ni mass. The ^{56}Ni masses lie between 0.05-0.35 $M_\odot$ for the low-s and 0.1-0.8 $M_\odot$ for the normal-s populations. Our

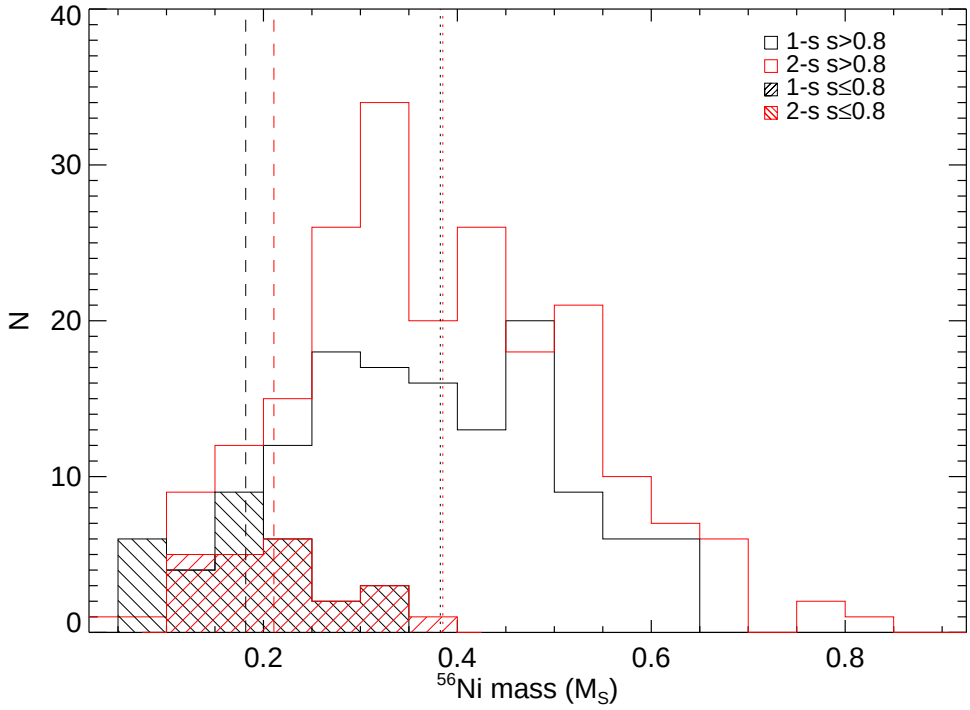

Figure 3.12: Distribution ^{56}Ni masses (solar units) for the normal-s (solid histograms) and low-s (filled histograms) SN Ia SNLS samples based on 1-s (black) and 2-s (red) fits. Vertical lines represent the mean for each case.

estimates are lower than typical values in the literature because of the lower rise-times. They are similar for both parameterizations of the lightcurve (see Figure 3.14).

Figure 3.13 shows ^{56}Ni masses as a function of the individual rise-times for all SN Ia. The relation of Ni mass and rise-time is expected from the use of Arnett's rule. The individual rise-times are obtained from the fiducial rise-time and the individual stretches, so that ^{56}Ni mass also relates with stretch. The scatter of ^{56}Ni masses is quite high at a given τ_r. This is due the large range of bolometric luminosities as seen in the large distribution of $M_B^{\max}$, as seen in Figure 3.11.

One can also observe that, as the rise-time is more independent of stretch for the 2-s technique, there is a more diverse ^{56}Ni mass range for each stretch population. It may be beneficial to divide the LC into separate regions, rise and fall, to disentangle the rise portion from the primary width-luminosity driver, when studying early-time effects of SNe Ia.

3.5.3 Secondary lightcurve parameters

The need for secondary parameters to describe SNe Ia at early times, beyond the traditional core LC parameter like stretch or Δm_{15}, would have important consequences for the understanding of SNe Ia. To the precision achieved in this study, these secondary effects in the early

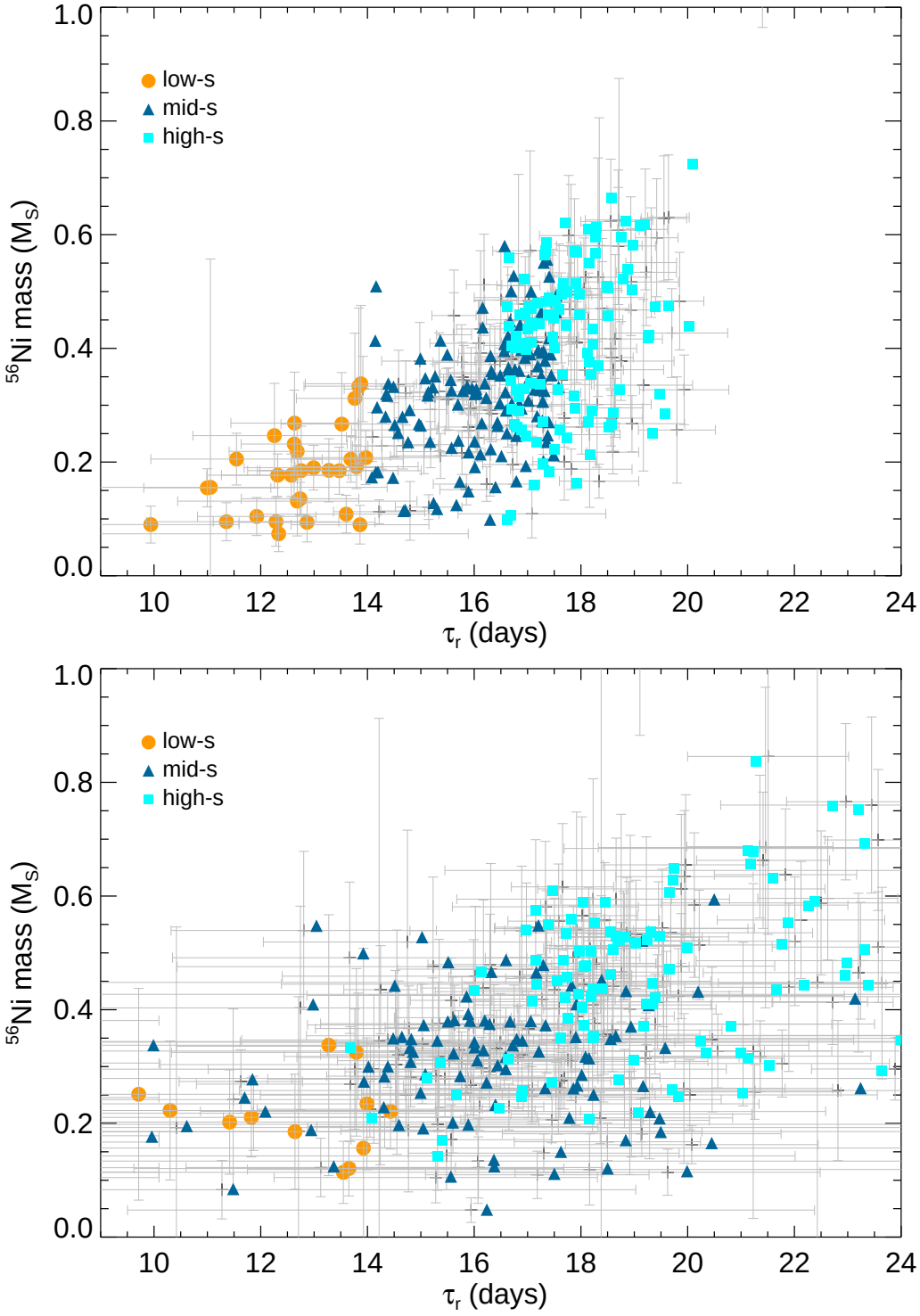

Figure 3.13: ^{56}Ni mass as a function of individual rise-time for the single- (*upper*) and two-stretch (*lower*) techniques. The low-s (orange circles), mid-s (blue triangles) and high-s (light blue squares) SNe Ia are indicated.

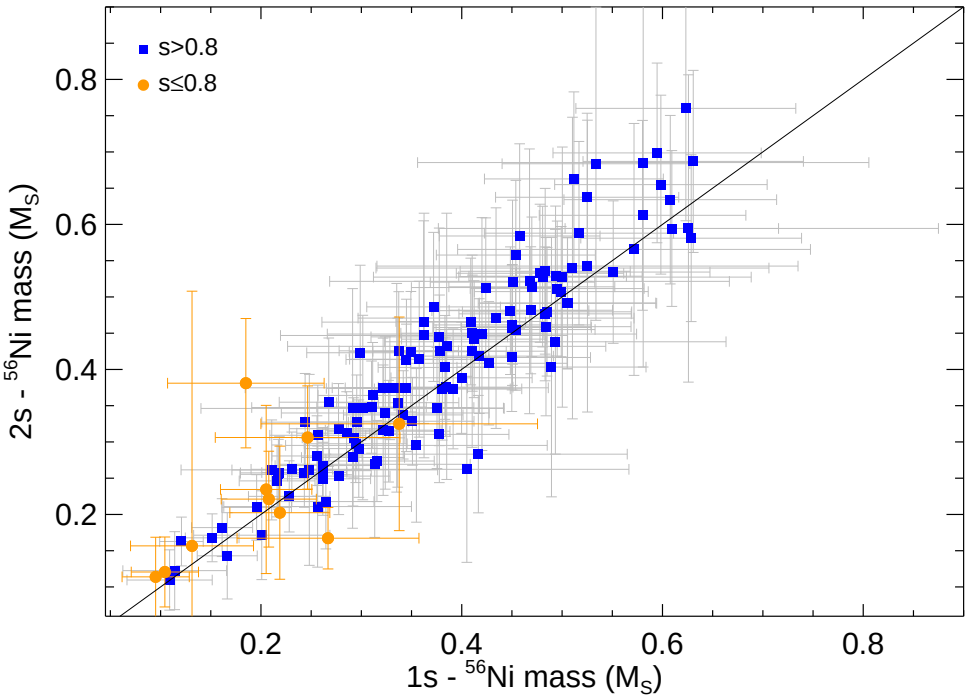

Figure 3.14: Comparison ^{56}Ni mass estimates as calculated in § 3.5.2 for the single- and two-stretch techniques. Green open circles are the low-s objects.

rise-time region do not seem necessary to describe SN Ia LCs. We find a low-significance trend towards longer rise-times in fast decliners *after* stretch correction. If confirmed with more data, this would mean that rise-times do not correlate to second-order with stretch and ^{56}Ni mass. This would suggest that beyond the radioactive decay of nickel which only sets in later in the LC, some other parameter in the initial explosion in the outer ejecta could play a role.

Besides a primary parameter responsible for the luminosity-width relation of SNe Ia, like ^{56}Ni mass (from a varying density at the transition of subsonic deflagration to supersonic detonation in the delayed-detonation scenario), Höflich et al. (2010) predict that there could be other variables like the C/O ratio of the WD progenitor that would affect the early part of the lightcurve. Higher C/O ratios result in a smaller binding energy at time of the explosion of the WD. In turn, this leads to higher expansion velocities meaning a faster photosphere recession and a shorter rise to maximum light. Lower main-sequence masses (during He-core and He-shell burning for example) can lead to higher C/O ratios. This would imply that lower-stretch SNe Ia with longer rise-times come from higher masses. The fact that low-stretch SNe Ia are primordially found in old environments suggest that their progenitors are long-lived and of low-mass (González-Gaitán et al. 2011), in contradiction to these findings.

On the other hand, low-stretch SNe having longer rise-times is reminiscent of the behavior predicted by Fink et al. (2010) for the double-detonation of sub-Chandrasekhar models.

The initial He-shell detonation on the WD surface can lead to a detonation of the CO core of the WD. Varying WD masses (0.8-1.4$M_{\odot}$), and with it their central core and shell densities, give rise to a variety of ^{56}Ni masses and burning products powering the lightcurve. Particularly they find that brighter events have faster rise-times. This is because brighter explosions produce more core ^{56}Ni that expand faster with less opacity in the outer shells from iron-group-elements created in the He-shell detonation. Their effect is anti-corrected with stretch, which would indicate a primary correction rather than a secondary one. In this picture, the lightcurve and the rise-time are directly related to the initial mass of the WD. Lower-mass WDs (of $\sim 0.8M_{\odot}$) have lower He-shell and CO core densities leading to a distribution of burning products that give rise to slower rise-times for low-stretch SNe Ia. Lower mass WDs producing fast decliners would agree with the aforementioned observations of older host environments.

Another interesting feature of the predictions by Fink et al. (2010) is that the contribution of other radioactive elements like ^{52}Fe and ^{48}Cr of short decay times can make the rise-time longer. This is particularly true for subluminous SNe Ia, which in their models produce as much as 20% of these radioactive nuclei, particularly ^{44}Ti, which does not contribute to the early lightcurve, but is known to be observed in the spectra as well. These yields are a direct consequence of the initial He-shell detonation.

3.6 Conclusions

We have constructed aggregate restframe B-band LCs of a sample of spectroscopic and photometrically identified SNe Ia at $z \leq 0.7$ from the SNLS. We obtain fiducial rise-times that are consistent with measurements for the low-z and SDSS-II samples calculated here with the same techniques. We extend our SNLS sample and show that there is no significant evolution in the early portion of SN Ia lightcurves up to $z = 1.0$.

We find that the use of a two-stretch parameterization for the lightcurve fits of SNe Ia is equivalent to the single-stretch parameterization. We confirm the consistency for the SDSS-II and SNLS samples while the nearby set has a rise-time $\sim 1.5\sigma$ lower for the 2-s technique and discrepant with all other calculated rise-times. The 2-s approach might be useful for detailed studies of the early-rise time that reach higher precision than the one attained in this work. We insist in the importance of proper lightcurve fitters with parameters that can take into account earlier parts of the lightcurve (stretch vs Δm_{15}) and that include multi-band information, and of templates trained with sufficient SNe with early time data.

We have compared the early region fits for different stretch population of the SNLS. We find that the stretch-corrected rise-times are consistent within uncertainties for slow and fast decliners. We extend this result to the lowest stretch objects. These findings are independent

of systematics such as the maximum epoch allowed in the early time fits, as well as on the two LC parameterizations assumed. The present study averages over samples which can have obvious difficulties like the low statistics of the low-stretch population. At a low significance of $\sim 1\sigma$, our results also agree with a trend for longer rise-times in fast declining SNe Ia. If these indications are confirmed, then SN Ia explosions differ beyond a single parameter orchestrating the lightcurve of SNe Ia. Secondary parameters in the early rise region would be necessary to fully model the lightcurves and could provide useful insights into SN Ia explosions. Such an indication is also found for the SDSS-II, as in H10.

However, to the precision attained in this study, SNe Ia remain extremely homogeneous all the way to very early times. One single lightcurve parameter, that possibly translates to a unique physical variable, like the transition density of deflagration to detonation in the delayed detonation model, can account not only for the core lightcurves of SNe Ia, but largely for the rise-time as well. The similarity of SN Ia lightcurves (after stretch-correcting) argue for a real common origin, with subluminous SNe Ia at the extreme end of the population.

The fiducial rise-time we find translates into ^{56}Ni masses of $0.05 - 0.90 M_{\odot}$ for all SNe Ia (and $0.05 - 0.35 M_{\odot}$ for low-s SNe Ia). Although our assumed IR contribution to the bolometric luminosity is uncertain, extremely low amounts of radioactive ^{56}Ni seem enough to power a faint SN Ia, less than that the amount found by Filippenko et al. (1992b); Leibundgut et al. (1993). Our SNe with the lowest radioactive nickel yield even rival with peculiar extreme objects such as the ones found by McClelland et al. (2010); Kasliwal et al. (2010); Poznanski et al. (2010), and pose a challenge to explosion models.

Such weak explosions seem unlikely to be the outcome of a runaway of a WD near the Chandrasekhar mass. Sub-Chandrasekhar models have been indeed a natural way of explaining subluminous SNe Ia (e. g. Livne 1990; Woosley & Weaver 1994), and possibly all SNe Ia (Fink et al. 2010; Sim et al. 2010; van Kerkwijk et al. 2010). Located in passive environments that are characteristic of old populations, low-mass WDs seem a promising progenitor of subluminous SNe Ia. With recent rejections of a high fraction of RG donors (Hayden et al. 2010b; Bianco et al. 2011), a double degenerate merger leading to the sub-Chandrasekhar explosion of a low-mass WD with very low ^{56}Ni yield appears increasingly plausible. If SNe Ia share a common explosion and progenitor mechanism, a varying progenitor WD mass could possibly explain the different SN Ia radioactive yield and luminosity, and their environment. More and better simulations need to test the validity of this picture. Pakmor et al. (2010), for example, modelled the merger of two $\sim 0.9 M_{\odot}$ WDs and obtained a subluminous SN Ia explosion with $\sim 0.1 M_{\odot}$ of synthetized ^{56}Ni, in agreement with the bulk of our low-s objects but in disagreement with the expected progenitor masses from the environments. More theoretical development need to complement the abundant current and coming observations of SNe Ia.

Chapter 4

A Simple Photometric Typing Technique for Plateau Supernovae

4.1 Introduction

Core-collapse supernovae (SNe) are the explosive final state of massive stars. They energize the regions of stellar formation and provide the heavy elements necessary to life, by enriching the interstellar medium and affecting the evolution of galaxies. Plateau supernovae are the most frequently occuring class of core-collapse SNe. The ejecta of a massive Hydrogen envelope traps energy from the intial shockwave, slowly releasing it over time and creating a characteristic flat light-curve or "plateau" after maximum, most notably in the longer optical wavelengths and lasting for about 80-150 days. They have been used as distance indicators through theoretical (e.g. Kirshner & Kwan 1974; Baron et al. 2004) and empirical (Hamuy & Pinto 2002; Nugent et al. 2006) methods. Their physics is relatively well understood and progenitors have been detected in pre-explosion images (Smartt et al. 2009, and references therein).

With the advent of technologies in wide-field imaging and automation, current surveys like KAIT (Li et al. 2001a), the Sloan Digital Sky Survey (SDSS-II Frieman et al. 2008) and the Supernova Legacy Survey (SNLS Astier et al. 2006; Perrett et al. 2010) have increased the number of discovered SNe by several hundreds. Furthermore, the photometry of these surveys covers multiple optical bands and has a good cadence providing a quality sampling of the whole light-curve. Upcoming surveys such as the Dark Energy Survey (DES: Bernstein et al. 2009), the Panoramic Survey Telescope (Pan-STARRS)[1] and the Large Synoptic Survey Telescope (LSST: Ivezic et al. 2008) will dramatically increase the number of SNe discovered,

[1] http://pan-starrs.ifa.hawaii.edu/public

rendering pure spectroscopic typing of even a small fraction utterly impractical. This clearly demands consistent and efficient techniques to type the different SNe based solely on photometry.

Photometric SN classification is an area of past and present research. Motivated by their use as standardizable candles for cosmological purposes, the prioritization of SNe Ia for spectroscopic follow-up has resulted in a relative shortage of well studied, high-z core-collapse SNe. Besides the efforts in the SN Ia classification for prioritization (Dahlén & Goobar 2002; Sullivan et al. 2006a) or posterior identification (Riess et al. 2004; Barris & Tonry 2006), Bazin et al. (2011) and Perrett et al. (2011) have analyzed archived data in the SNLS to find SNe Ia that had no spectroscopic confirmation. Similarly, estimation of their photometric redshifts has also been performed for actual datasets (Palanque-Delabrouille et al. 2010; Kessler et al. 2010a) or simulated ones (Gong et al. 2010). These techniques most often use model template fits to the light-curve but also color-color diagrams, as well as host galaxy redshift prior information.

The paucity of data makes investigating methods for classifying core-collapse SNe more difficult, especially when combined with the much wider diversity of light-curve behavior they exhibit, compared with SNe Ia. Among the methods that have been tried are: taking advantage of the color-color evolution (Poznanski et al. 2002), color-magnitude evolution (Johnson & Crotts 2006), Bayesian template fitting (Poznanski et al. 2007), Bayesian classification schemes (Kuznetsova & Connolly 2007) and Fuzzy Set Theory algorithms (Rodney & Tonry 2009). As each method was trained and tested on different samples, it is difficult to directly understand and evaluate the effectiveness of these techniques.

To address this problem, Kessler et al. (2010b, hereafter K10) released a public challenge to type simulated transient (based on the characteristics of the upcoming DES survey) in the redshift range $0 < z < 1.0$ with/without host redshift prior information. This useful exercise featured several participants with different methods and revealed the underestimated, serious difficulty of photometric typing. Among others, some techniques were recently published by the participating authors: boosting and kernel density estimation techniques (Newling et al. 2011) and a semi-supervised learning (Richards et al. 2011).

In this work, we present a simple multi-band SN IIP identification technique based on post-maximum linear fits. We find it useful to focus our efforts on a single class of core-collapse SNe, instead of attempting to simultaneously classify all SN types. SNe IIP should be particularly easy with their characteristic light-curve plateau (see Figure 4.1) and color evolution. The method, which was also used in the public challenge of K10, can be used across different redshifts in current and future supernova surveys. It does not require any spectral template, which for a very diverse population like SNe IIP can be quite complicated to model. This paper is organized as follows: in section 4.2, we introduce the metrics that we will use to quantify

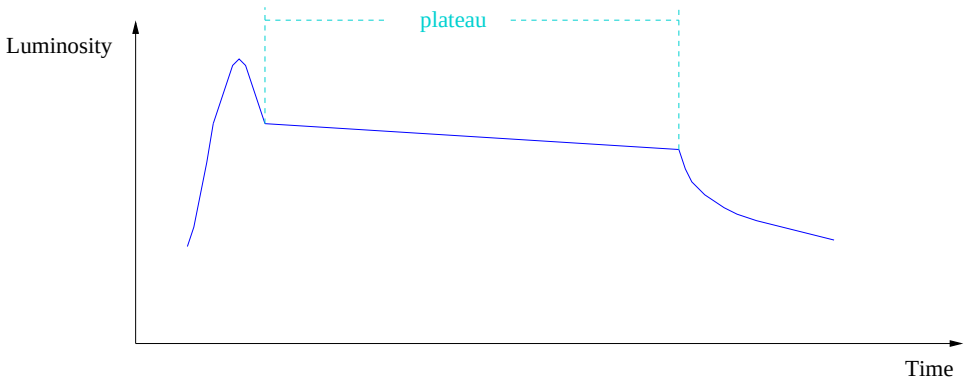

Figure 4.1: Sketch of the characteristic light-curve of a SN IIP.

the performance of the typing of the samples studied here and presented in section 4.3. In section 4.4, we explain our method and we show our results in section 4.5, and finally we conclude in section 4.6.

4.2 Typing evaluation

In order to evaluate the classification, a proper parameter that quantifies the quality of the typing is needed. We use the same figure-of-merit (FoM) as K10, which consists of two components: the efficiency, giving us a percentage of the total number of objects that were actually identified, and the purity, a measure of how clean (and free of contaminants) the typed sample is.

If $N_{\rm IIP}^{\rm true}$ is the number of correctly identified SNe IIP and $N_{\rm IIP}^{\rm tot}$ the total number of SNe IIP, then the SN IIP efficiency is given by:

$$\epsilon_{\rm IIP} = \frac{N_{\rm IIP}^{\rm true}}{N_{\rm IIP}^{\rm tot}} \tag{4.1}$$

If $N_{\rm IIP}^{\rm false}$ is the number of non-IIPs incorrectly tagged as SNe IIP, then the purity[2] is defined as:

$$P_{\rm IIP} = \frac{N_{\rm IIP}^{\rm true}}{N_{\rm IIP}^{\rm true} + N_{\rm IIP}^{\rm false}}, \tag{4.2}$$

The purity is one for a perfectly typed sample free of non-IIPs, and it approaches zero as more of the tagged objects are contaminated by non-IIPs.

The FoM adopted here gives equal weight to the SN IIP efficiency and purity:

[2]In the nomenclature of K10, we are using the "true" purity, i. e. a false-tag weight of one, $W_{\rm IIP}^{\rm true} = 1$

$$\begin{aligned} \mathrm{FoM_{IIP}} &= \epsilon_{\mathrm{IIP}} \times P_{\mathrm{IIP}} \\ &= \frac{1}{N_{\mathrm{IIP}}^{\mathrm{tot}}} \frac{\left(N_{\mathrm{IIP}}^{\mathrm{true}}\right)^2}{N_{\mathrm{IIP}}^{\mathrm{true}} + N_{\mathrm{IIP}}^{\mathrm{false}}} \end{aligned} \tag{4.3}$$

The FoM ranges between 0 and 1 and gives a measure of the quality of the typing. We try to optimize this number in this study, but it is easy to conceive different surveys adopting alternative FoMs depending on their scientific goals.

4.3 Samples

To study the performance of our SN IIP classification technique, we analyze several real and simulated datasets. Table 4.1 summarizes these samples.

Table 4.1: SN samples (real and simulations) used to investigate the simple SN IIP typing technique. Numbers in parenthesis are for the sets with host-z information, when available

SN sample	N_{IIP}	$N_{\mathrm{non-IIP}}$	Redshift*	Source
Low-z	38	336	$z < 0.1$	see Table 4.2
SDSS	34	95	$0 < z < 0.2$	D'Andrea et al. (2010); Holtzman et al. (2008)
SNLS	13	381	$0 < z < 1.1$	–
DES-training (host)	236(218)	1043(1038)	$0 < z < 0.6$	K10
DES-training/post-mortem (host)	436(492)	738(773)	$0 < z < 1.1$	See § 4.4.6
DES-challenge (host)	8637(8643)	9710 (9678)	$0 < z < 1.1$	K10
LSST-training†	233	539	$0 < z < 0.7$	K10
LSST-training/post-mortem	449	304	$0 < z < 1.1$	See § 4.4.6
LSST-challenge	26252	16523	$0 < z < 1.1$	K10

*The redshift range covered by SNe IIP.
†The LSST simulated survey has host photo-z for all SNe.

The nearby sample ($z < 0.1$) is collected from the literature and contains 38 SNe IIP and 336 non-IIP, the vast majority being SNe Ia (see Table 4.2). We also use the first year SDSS-II sample of 34 SNe IIP (D'Andrea et al. 2010) and 95 SNe Ia (Holtzman et al. 2008). The three year SNLS sample consists of 13 SNe IIP and 381 non-IIP. These datasets are heavily biased towards SNe Ia and they do not represent a natural distribution of the different SN types. It is therefore important to use simulated samples that contain a a more physical mix of SN types.

We use the synthetic DES sample of K10 designed for the classification challenge. This constitutes a set of ~ 20000 simulated SNe in the $0.0 < z < 1.1$ range, with a spectroscopic

training sub-sample of ~ 1200 SNe. A similar sample with host redshift information is provided. We investigate both of these samples and show the results for the training sample and the full sample based on the provided training sample, and also on a deeper training sample selected here *after* the challenge was completed ("post-mortem", see section 4.4.6). The latter training sample covers a larger redshift range that is more representative of the full sample.

Furthermore, we analyze the artificial LSST sample provided by K10[3]. This is the "deep" part of their simulations and consists of ~ 26000 objects with redshifts $0.0 < z < 1.1$, and a spectroscopic training sample of ~ 700 SNe. The sample also has simulated photometric redshifts from the host galaxies. Similar to the DES, we perform an additional classification with an improved training sample after completion of the challenge.

The performance of our method varies considerably between SN samples. This is not surprising given the wide range in sample properties such as the bandpasses, the photometric quality (signal-to-noise) and cadence of the light-curve coverage. For some low-z SNe, the light-curve has large gaps without any data, preventing the correct estimation of the start of the plateau, or the plateau fit itself. For very high-z SNe from the simulated surveys, the signal-to-noise can be quite low and the typing becomes more unreliable.

We do not attempt to photometrically type all objects from each sample, but instead apply data selection criterion cuts to remove bad data and optimze the purity. However, note that $N_{\rm IIP}^{tot}$ in our efficiency calculation (Eq. 4.1) reflects the total number of SNe IIP in the sample, irrespective of these cuts, so the FoM is properly penalized for choosing overly severe cuts. In all cases we do not make use of the noisy ($S/N < 3$) blue data of the SDSS ($u_{2.5m}$ and $g_{2.5m}$), and of the simulated DES ($DESg$) and LSST ($LSSTu$ and $LSSTg$). These surveys have in some cases extremely unreliable noisy light-curves in these bands.

Table 4.2: Nearby supernovae used in this study

Objects	Type	Source
SN1968L	SN IIP	Wood & Andrews (1974)
SN1970G	SN IIP	Winzer (1974); Barbon et al. (1973)
SN1973R	SN IIP	Ciatti & Rosino (1977)
SN1986I	SN IIP	Pennypacker et al. (1989)
SN1988A	SN IIP	Benetti et al. (1991); Turatto et al. (1993)
SN1988H,SN1989C	SN IIP	Turatto et al. (1993)
SN1990E	SN IIP	Schmidt et al. (1993); Benetti et al. (1994)
SN1990K	SN IIP	Cappellaro et al. (1995)
SN1991G	SN IIP	Blanton et al. (1995)
SN1992am	SN IIP	Schmidt et al. (1994b)
SN1992ba	SN IIP	Pastorello (2003)
SN1992H	SN IIP	Clocchiatti et al. (1996)
SN1994N,SN199eu,SN2001dc	SN IIP	Pastorello et al. (2004)

[3]All these sets can be found at `http://sdssdp62.fnal.gov/sdsssn/SIMGEN_PUBLIC`

Table 4.2 – **Continued**

Objects	Type	Source
4 SNe	SN IIP	Pastorello (2003)
SN1997D	SN IIP	Benetti et al. (2001)
SN1998A	SN IIP	Pastorello et al. (2005)
SN1999br	SN IIP	Pastorello et al. (2004)
SN1999em	SN IIP	Hamuy et al. (2001); Leonard et al. (2002b); Elmhamdi et al. (2003)
SN1999gi	SN IIP	Leonard et al. (2002a)
SN2000cb	SN IIP	Kleiser et al. (2011)
SN2001X	SN IIP	Tsvetkov (2006a)
SN2002hh	SN IIP	Pozzo et al. (2006); Tsvetkov et al. (2007)
SN2003gd	SN IIP	Hendry et al. (2005)
SN2003hn	SN IIP	Krisciunas et al. (2009a)
SN2004A	SN IIP	Hendry et al. (2006); Tsvetkov (2008)
SN2004dj	SN IIP	Chugai et al. (2005); Vinkó et al. (2006); Zhang et al. (2006); Tsvetkov et al. (2008)
SN2004ek	SN IIP	Tsvetkov (2008)
SN2004et	SN IIP	Misra et al. (2007); Sahu et al. (2006)
SN2005ay	SN IIP	Tsvetkov et al. (2006)
SN2005cs	SN IIP	Tsvetkov et al. (2006); Brown et al. (2007); Dessart et al. (2008); Pastorello et al. (2009b)
SN2006bp	SN IIP	Dessart et al. (2008)
SN2008bk	SN IIP	Van Dyk et al. (2010)
SN2008gz	SN IIP	Roy et al. (2011)
SN2009md	SN IIP	Fraser et al. (2010)
SN1990S	SN IIn	Hamuy et al. (1993)
SN1993G	SN IIL	Tsvetkov (1994)
SN1994Y	SN IIn	Ho et al. (2001)
SN1995G	SN IIn	Pastorello (2003)
SN1997bs	SN IIn?impostor?	Van Dyk et al. (2000)
SN1998bw	SN Ic	McKenzie & Schaefer (1999); Sollerman et al. (2000); Patat et al. (2001)
SN1998S	SN IIL	Liu et al. (2000)
SN1999el	SN IIn	Di Carlo et al. (2002)
SN1999ga	SN IIL	Pastorello et al. (2009a)
SN2000er,SN2002ao	SN Ibn	Pastorello et al. (2008b)
SN2001B	SN Ib	Tsvetkov (2006a)
SN2002ap	SN Ic	Gal-Yam et al. (2002a); Yoshii et al. (2003); Foley et al. (2003)
SN2003bg	SN IIb	Hamuy et al. (2009)
SN2002bj	SN IIn?.Ia?	Poznanski et al. (2010)
SN2003jd	SN Ic	Valenti et al. (2008)
SN2003lw	SN Ic	Malesani et al. (2004)
SN2004aw	SN Ic	Taubenberger et al. (2006)
SN2004A,SN2004gk	SN Ibc	Elmhamdi et al. (2010)
SN2005bf	SN Ib	Folatelli et al. (2006)
SN2005la	SN IIb	Pastorello et al. (2008a)
SN2006aj	SN Ic	Sollerman et al. (2006); Pian et al. (2006)
SN2006gi	SN Ib	Elmhamdi et al. (2010)
SN2006gy	SN IIn	Agnoletto et al. (2009)
SN2006jc	SN Ibn	Pastorello et al. (2007a, 2008b); Anupama et al. (2009)
SN2007bg	SN Ic	Young et al. (2010)
SN2007bi	SN Ic?PI?	Young et al. (2010); Gal-Yam et al. (2009)
SN2007gr	SN Ic	Hunter et al. (2009)
SN2007rt	SN IIn	Trundle et al. (2009)

Table 4.2 – **Continued**

Objects	Type	Source
SN2008es	SN IIL	Miller et al. (2009)
SN2008am	SN IIn	Chatzopoulos et al. (2011)
SN2008ax	SN IIb	Pastorello et al. (2008c); Roming et al. (2009); Tsvetkov et al. (2009)
SN2008D	SN Ib	Modjaz et al. (2009)
SN2008S	SN IIn?impostor?	Smith et al. (2009)
SN2008iy	SN IIn	Miller et al. (2010)
SN2009bb	SNIc	Pignata et al. (2011)
SN2009jf	SN Ib	Sahu et al. (2011)
SN2010ah	SN Ic	Corsi et al. (2011)
SN2010jl	SN IIn	Stoll et al. (2010)
SN2010gx	SN Ic?	Pastorello et al. (2010)
SN2010X	SN Ic?.Ia?	Kasliwal et al. (2010)
SN1980N,SN1981d	SN Ia	Hamuy et al. (1991)
SN1981B	SN Ia	Buta & Turner (1983); Barbon et al. (1982)
SN1986G	SN Ia	Phillips et al. (1987)
29 SNe	SN Ia	Hamuy et al. (1996b)
SN1990N,SN1991T	SN Ia	Lira et al. (1998)
SN1991bg	SN Ia	Turatto et al. (1996); Filippenko et al. (1992b)
SN1991M,SN1991T,	SN Ia	Ford et al. (1993)
18 SNe	SN Ia	Altavilla et al. (2004)
21 SNe	SN Ia	Riess et al. (1999a)
SN1994D	SN Ia	Richmond et al. (1995); Meikle et al. (1996)
SN1995D	SN Ia	Sadakane et al. (1996); Riess et al. (1999a)
44 SNe	SN Ia	Jha et al. (2006)
SN1997cn	SN Ia	Turatto et al. (1998)
SN1998aq	SN Ia	Riess et al. (2005)
SN19998bu	SN Ia	Suntzeff et al. (1999)
SN1999aa,SN1999cp	SN Ia	Krisciunas et al. (2000)
8 SNe	SN Ia	Kowalski et al. (2008)
SN1999aw	SN Ia	Strolger et al. (2002)
SN1999by	SN Ia	Garnavich et al. (2004)
SN1999cc,SN1999cl,SN2000cf	SN Ia	Krisciunas et al. (2004c)
5 SNe	SN Ia	Krisciunas et al. (2001)
SN1999ee	SN Ia	Stritzinger et al. (2002); Krisciunas et al. (2004a)
SN2000bh,SN2000ca,SN2001ba	SN Ia	Krisciunas et al. (2004a)
SN2000cx	SN Ia	Li et al. (2001b)
SN2000E	SN Ia	Valentini et al. (2003); Tsvetkov (2006a)
185 SNe	SN Ia	Hicken et al. (2009)
7 SNe	SN Ia	Krisciunas et al. (2004b)
SN2001el	SN Ia	Krisciunas et al. (2003)
SN2002bf	SN Ia	Leonard et al. (2005)
SN2002cx	SN Ia	Phillips et al. (2007)
SN2002dj	SN Ia	Pignata et al. (2008)
SN2002dr	SN Ia	Pignata et al. (2004)
SN2003cg	SN Ia	Elias-Rosa et al. (2006)
SN2003du	SN Ia	Anupama et al. (2005); Stanishev et al. (2007)
SN2003hx	SN Ia	Misra et al. (2008)
SN2003gs	SN Ia	Krisciunas et al. (2009b)
35 SNe	SN Ia	Contreras et al. (2010)
SN2004eo	SN Ia	Pastorello et al. (2007b)
SN2004fu	SN Ia	Tsvetkov (2006b)
SN2004S	SN Ia	Krisciunas et al. (2007)
SN2005am	SN Ia	Li et al. (2006a)
SN2005bl	SN Ia	Taubenberger et al. (2008)

Table 4.2 – **Continued**

Objects	Type	Source
SN2005cf	SN Ia	Wang et al. (2009b)
SN2005hk	SN Ia	Phillips et al. (2007)
SN2006gz	SN Ia	Hicken et al. (2007)
SN2007qd	SN Ia	McClelland et al. (2010)

4.4 Method

The characteristic plateau of SNe IIP stands out as an excellent feature for an easy identification based solely on photometry. Although seemingly straightforward, one needs good sampling of the light-curve and an automated method that can easily and securely type a large number of candidates. We use a simple linear fit (in magnitudes) to multi-band photometry and then use the distributions of the different fit parameters to assign continuous probabilities of being a SN IIP.

4.4.1 Maximum epoch

First, in order to do a proper linear fit to find a plateau, we need an estimate of the beginning epoch of the plateau. Such a phase happens right after maximum brightness or, in some cases, a couple of days after maximum. As a first approach we will use the time of maximum brightness.

The latter is estimated in two steps. First, we get the date of the brightest data point in each band. We make sure that the signal-to-noise ratio of the selected data points is high enough ($S/N > 5$). This signal-to-noise condition is particularly important for the noisy, bluer bands of the SDSS and simulated DES/LSST samples. The closest estimate of maximum SN light is given by the first (earliest) of the maxima in the different bands.

This method evidently requires good sampling and pre-maximum data to ensure proper maximum estimation, although an offset of some days will not affect the post-maximum fit. The low-z dataset is most affected by this simple technique due to a lack of pre-maximum data and of dense time sampling. Requiring at least one pre-maximum data point in the light-curve ensures a better maximum estimate, as will be shown later. In general however, this simple method is good enough to estimate a first-order maximum for most transients in the different samples considered.

4.4.2 Simple linear post-maximum fit

We now proceed to fit all data past maximum in each band up to a final date, τ_f, to a line in magnitudes, or simple power of 10 in flux units[4]:

$$f = \alpha 10^{m\tau} \tag{4.4}$$

The fit slopes, m, differ among SN types, particularly between SNe IIP (see Figure 4.2) and other SNe (see Figure 4.3). SNe IIP are expected to have the shallowest negative slopes, or even positive slopes in some cases, whereas Type I SNe generally should decline very steeply. Other SNe II types may have a small plateau but of a shorter duration than SNe IIP.

For this to work, the range of the fit is extremely important. If we fit a line to data past the declining region, where the fluxes are close to zero, we might incorrectly obtain a shallow slope. Thus, in general, the fits of bluer bands will extend only to a small portion of the post-maximum light-curve ($\sim 20 - 30$ days) whereas longer wavelengths fits will cover a longer span ($\gtrsim 40 - 60$ days). The exact final fit epoch for each band depends on the survey and is studied in § 4.4.4.

Besides the linear fit parameters of Equation 4.4, we add another parameter: the interpolated flux at the end of the fitted region in each band (normalized to maximum flux). This gives an additional constraint that the shallow linear behavior found by the fit actually corresponds to a plateau and not to the late radioactive decay, where the relative fluxes are much lower.

These linear fits are not meant to represent a good model to the data; they are just a simple way to classify the objects. As such, the quality of the fit is irrelevant and we are only interested in the parameter space obtained, as shown in next section.

4.4.3 Multi-band fit parameters and probability distributions

The range spanned by the fit slopes in the different bands is the primary tool to differentiate SNe. As can be seen in Figure 4.4(a) for example, SNe IIP have shallower slopes than other SN types for the R-band of the nearby sample. SNe Ia clearly decline fastest, followed by SNe Ibc and other SNe II. SNe IIn have the closest slopes to SNe IIP and are the major source of contamination.

The distributions of the fluxes at the end of the fitted region relative to maximum are another useful discriminator. Figure 4.5(a) shows the interpolated fluxes at the end of the fitted region, day 40 after r-band maximum in this case, for the spectroscopic SNLS sample. These

[4]The measured flux slopes are in (dex $\times$ time) but can be converted to (mag $\times$ time) multiplying by 2.5

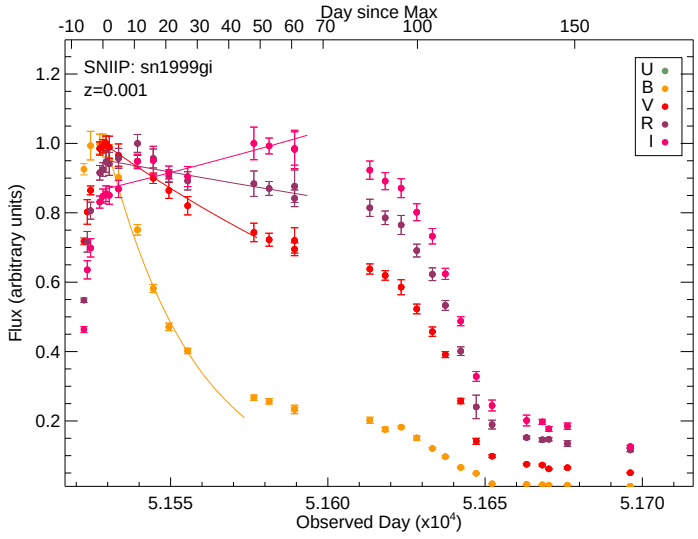

(a) SN IIP: SN1999gi

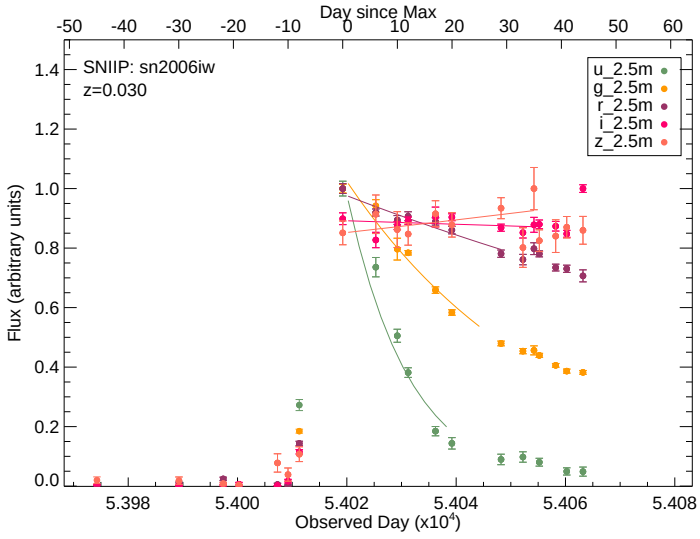

(b) SN IIP: SN2006iw (SDSS)

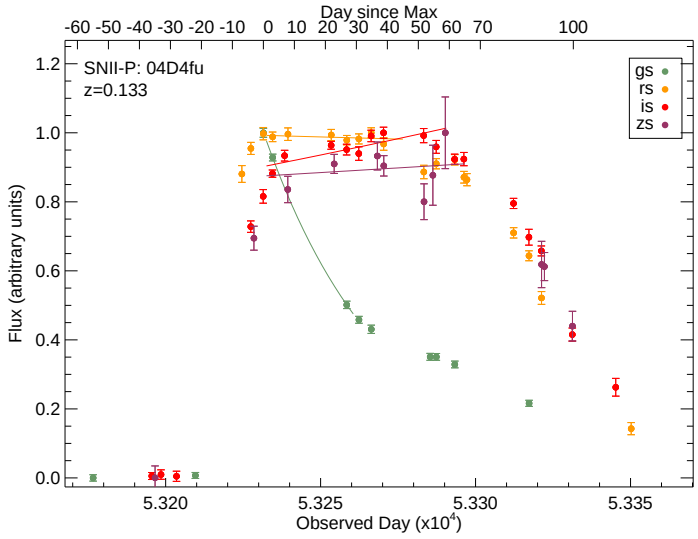

(c) SN IIP: 04D4fu (SNLS)

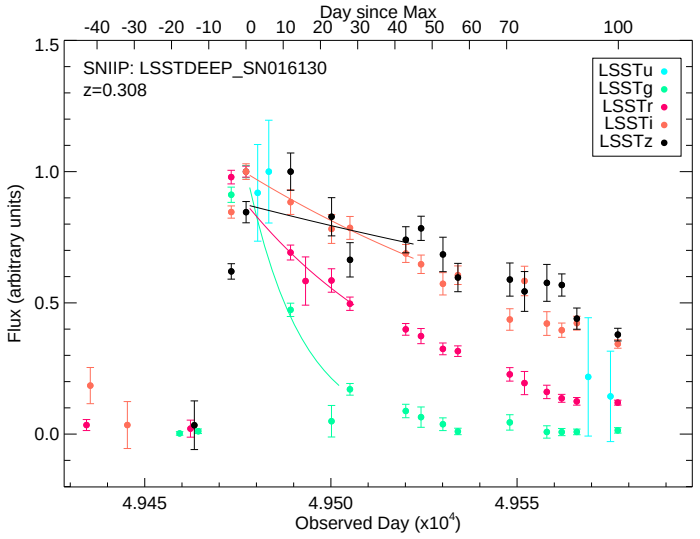

(d) SN IIP: SN016130 (LSST)

Figure 4.2: Examples of linear fits (like Eq. 4.4) to the post-maximum region in multiple bands of SN IIP light-curves from the low-s, SDSS-II, SNLS and simulated LSST samples. The colored points represent data in the different bandpasses, and the lines the corresponding fits.

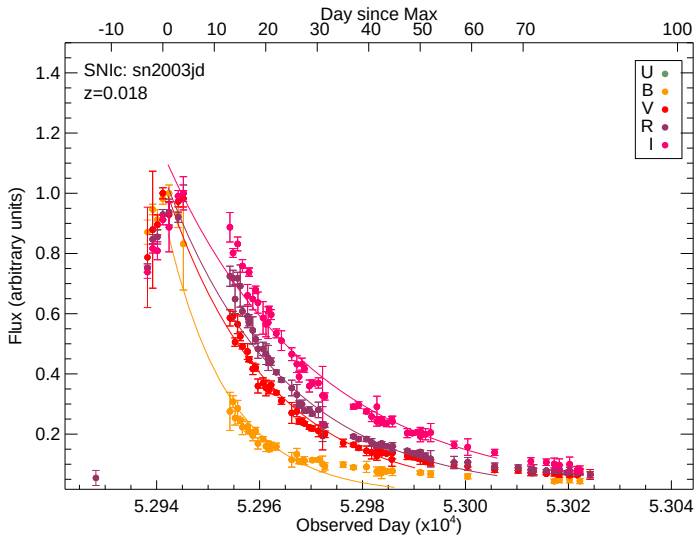

(a) SN Ic: SN2003jd

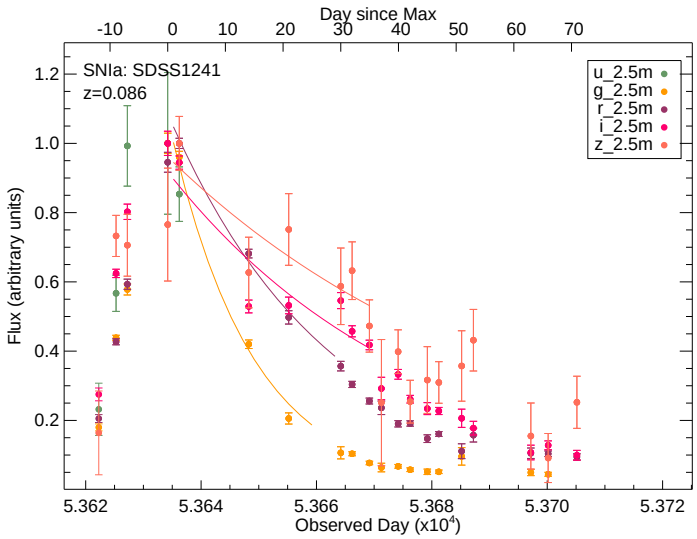

(b) SN Ia: SDSS1241 (SDSS)

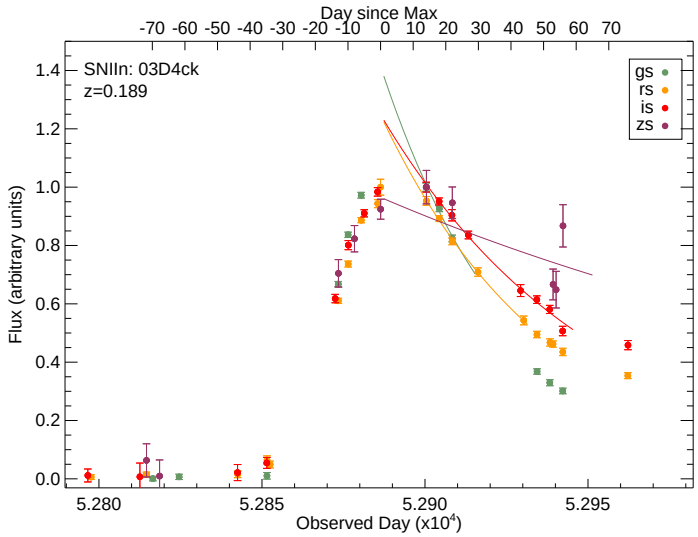

(c) SN IIn: 03D4ck (SNLS)

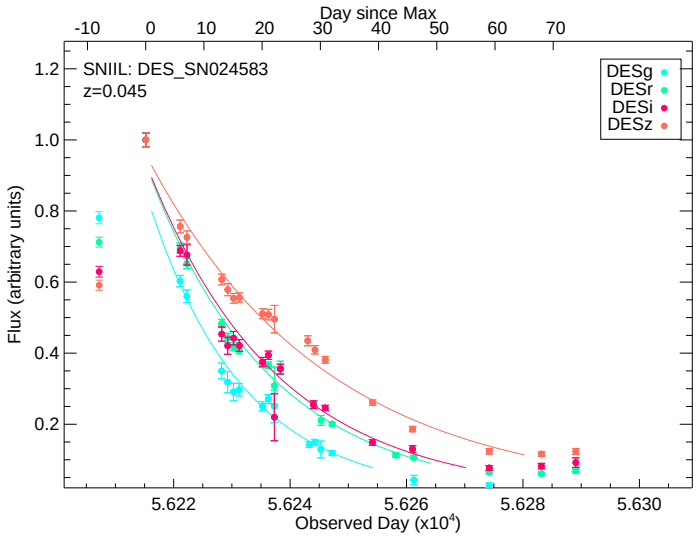

(d) SN IIL: 024583 (DES)

Figure 4.3: Examples of linear fits (like Eq. 4.4) to the post-maximum region in multiple bands for different non-IIP supernovae from the low-z, SDSS-II, SNLS and simulated DES samples. The colored points represent data in the different bandpasses, and the lines the corresponding fits.

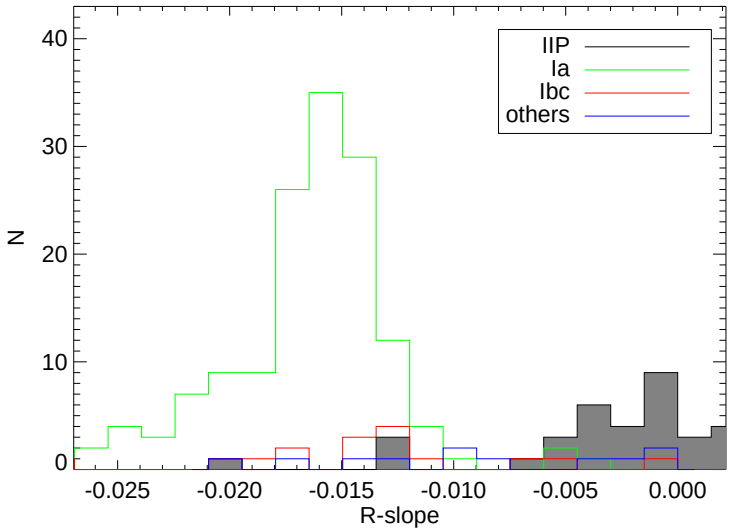

(a) R-slope

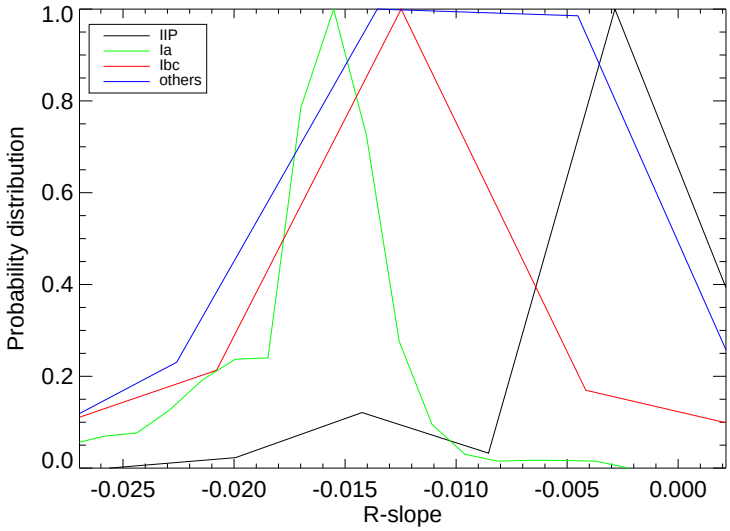

(b) R-slope distributions

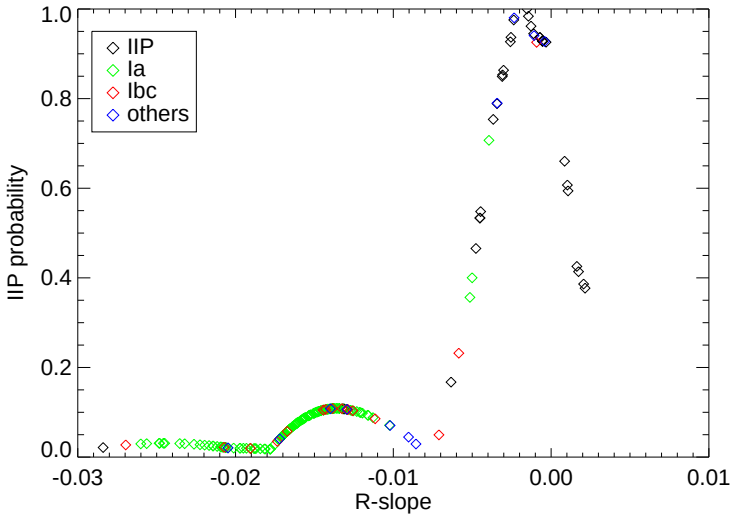

(c) R-slope SN IIP probabilities

Figure 4.4: (a) Fitted R-slope for different SN types of the low-z sample, (b) corresponding probability distributions per SN type normalized to peak, and (c) respective SN IIP probabilities, $p_{\rm IIP}$, for each SN based on the IIP probability distribution of (b).

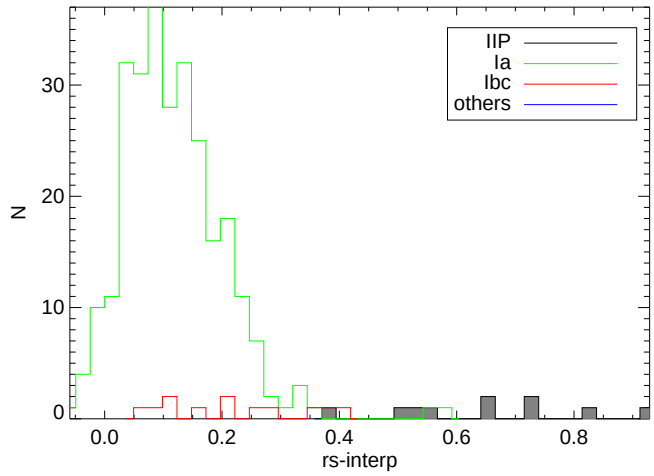

(a) rs-flux

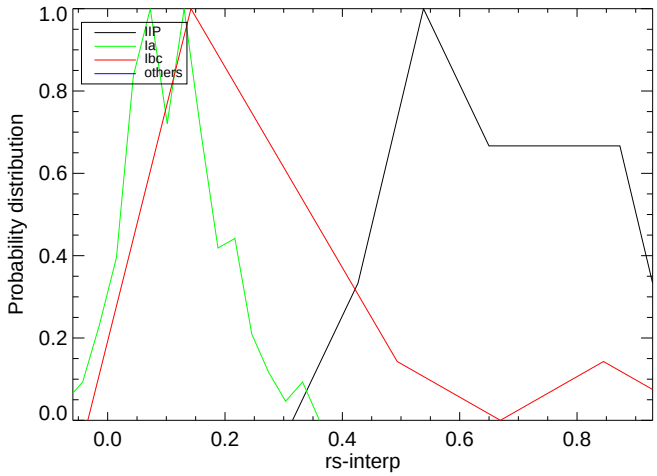

(b) rs-flux distributions

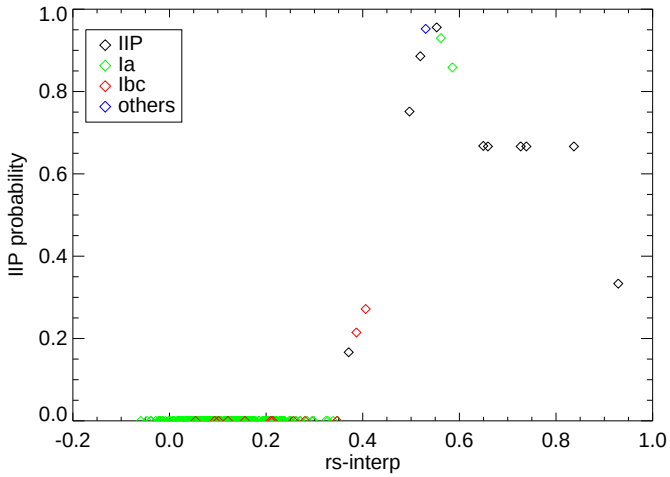

(c) rs-flux SN IIP probabilities

Figure 4.5: (a) Interpolated rs-flux at end of fitted region for different SN types of the SNLS spectroscopic sample, (b) corresponding probability distributions per SN type normalized to peak, and (c) respective SN IIP probabilities, p_{IIP}, for each SN based on the IIP probability distribution of (b).

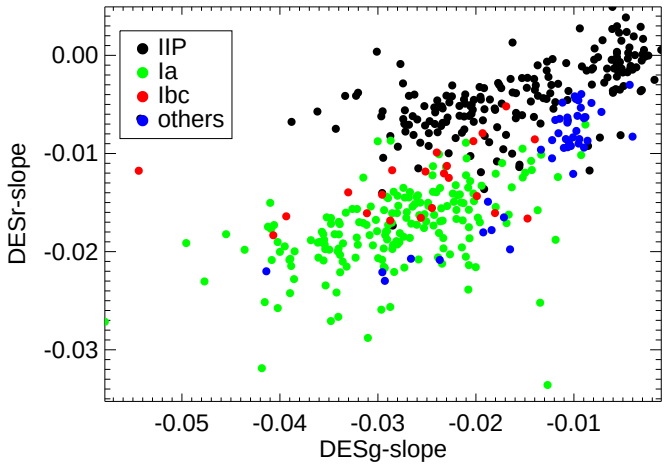

(a) r-slope vs g-slope

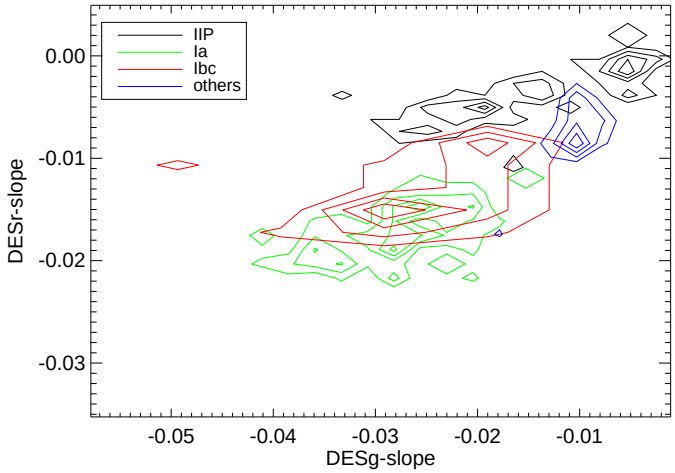

(b) r-slope vs g-slope contours

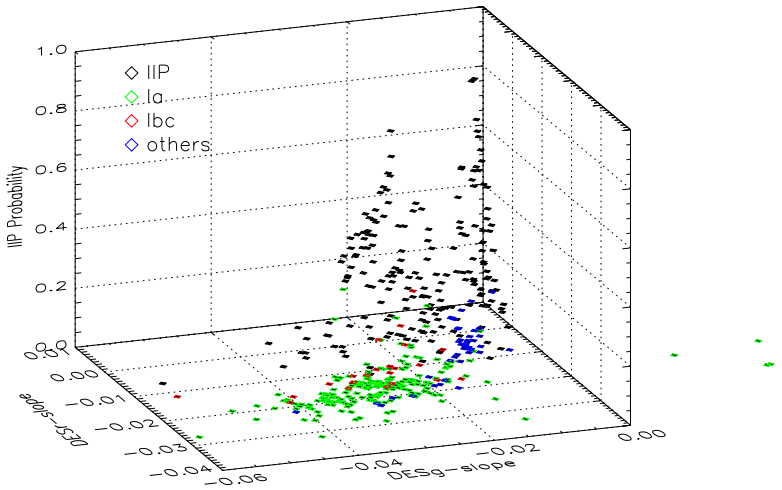

(c) r-slope vs g-slope SN IIP probabilities

Figure 4.6: (a) Fitted r-slope vs g-slope for different SN types of the simulated DES training sample, (b) corresponding contours of probability distribution per SN type normalized to peak, and (c) respective SN IIP probabilities, $p_{\rm IIP}$, for each SN based on the IIP probablity distribution of (b).

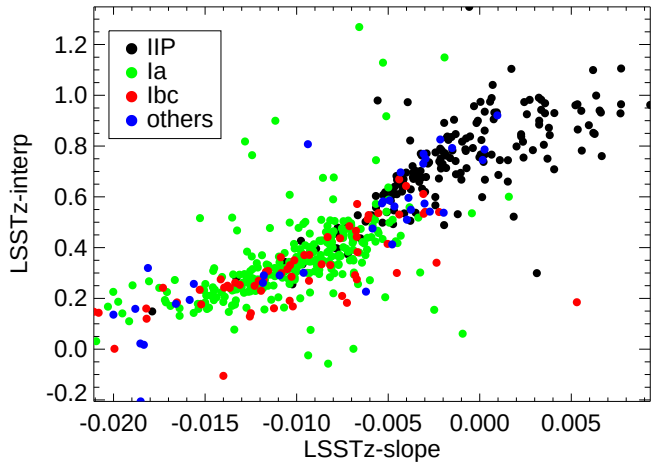

(a) z-flux vs z-slope

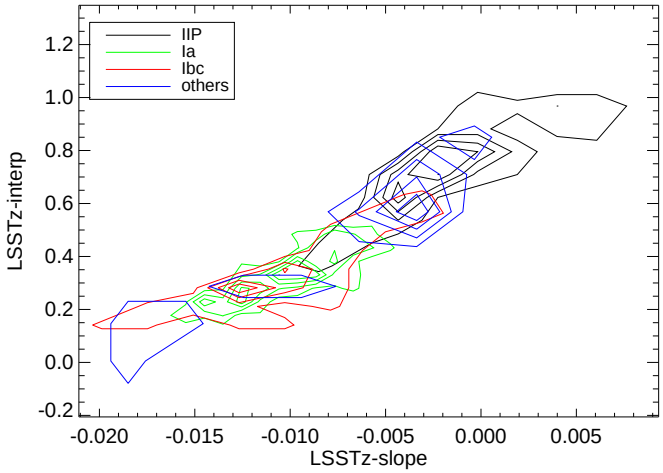

(b) z-flux vs z-slope contours

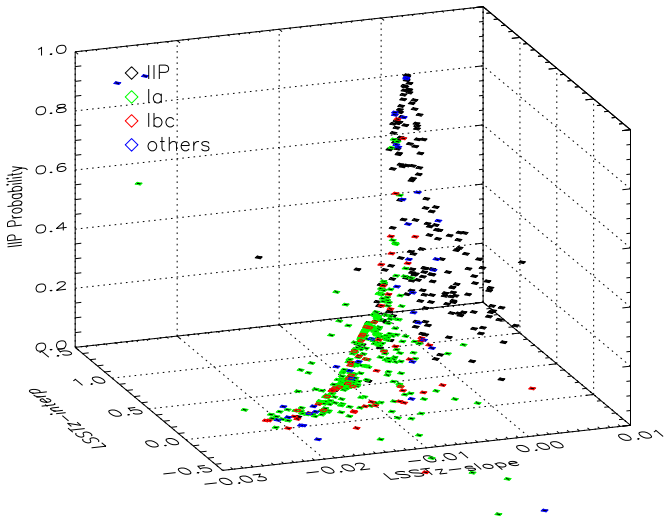

(c) z-flux vs z-slope SN IIP probabilities

Figure 4.7: (a) z-flux, interpolated at the end of the fit region, vs fitted z-slope for the different SN types of the simulated LSST training sample, (b) corresponding contours of probability distributions per SN type, and (c) respective SN IIP probabilities, $p_{\rm IIP}$, for each SN based on the IIP probability distribution of (b)

are higher for SNe IIP, for which the hydrogen envelope is still powering the optical display. Together with a flat plateau slope, these two parameters can differentiate SNe IIP and ensure that a shallow slope is not due to the earlier radioactive decline at the end of the light-curve of some SNe.

Even more enlightening is the use of multi-band slope-slope and slope-flux spaces to select SNe IIP. Parameter spaces of different band combinations take advantage of the distinguishing color evolution of various SNe. Figures 4.6(a) and 4.7(a) show that SNe IIP in the simulated DES and LSST training samples stand out from other SNe in particular regions of high slopes and large post-maximum fluxes. Multiple parameter spaces like these can discriminate SNe IIP, although overlapping objects still exist.

The SN classification could be based on the visual determination of particular SN IIP regions in the different parameter spaces. This, however, would be a difficult and time-consuming human component that does not ensure the most successful classification. With many parameter spaces and a lot of overlapping SNe from different types, we instead assign to each SN a continuous probability of being of each SN type. In order to do this, we use 1D and 2D kernel density estimators for our training set divided in SN types for each parameter space under consideration. The kernel density estimators provide probability distributions, from which a probability for each object is drawn. Figures 4.4(b) and 4.5(b) show the resulting 1D probability distributions, normalized to maximum, for the previous R-band slope of the low-z set and for the r-band flux of the SNLS. It is obvious from this procedure that a better typing will be achieved with a more complete training sample that contains enough SNe of multiple types (see $ 4.4.6). For the 2D cases, Figures 4.6(b) and 4.7(b) show the contours of the probability distributions of slope-slope and slope-flux spaces for the training samples of the DES and LSST, which represent a better suited database to study photometric typing.

Each SN is then assigned a "IIP probability" per parameter space (a value between 0 and 1) by interpolating the probablity distribution with the SN parameters. Figures 4.4(c) and 4.5(c) show an example of the obtained IIP probabilities for the 1D distributions shown earlier, and Figures 4.6(c) and 4.7(c) for the 2D spaces. Similarly, we calculate for each SN a probability of being of the other types considered.

In this way, we obtain for each object a probability of being a SN IIP, $p^i_{\rm IIP}$, and probabilities of being other SN types, like $p^i_{\rm Ia}$, $p^i_{\rm Ibc}$, $p^i_{\rm IIL,IIn}$, where i denotes each parameter space. All these probabilities are put together into a single matrix, $\mathbf{P}$, of size $m \times n$, with n the number of SNe considered and m the number of probabilities. In order to constrain the importance of each of these probabilities, we want to find a vector of weights, $\mathbf{w}$, of size m for each probability, that quantifies the importance of each space for the typing. We therefore solve following equation for $\mathbf{w}$:

$$\mathbf{c} = \mathbf{w} \times \mathbf{P}, \tag{4.5}$$

where c is a vector of n size. For the training set it is filled with 1 for SNe IIP and -1 non-IIP. The resulting vector of weights $\mathbf{w}$ can be then used for any SN to get a final SN IIP probability c_{SN} via the same equation.

Finally, a SN IIP is tagged if $\mathbf{c}_{\rm SN} > 0$ (see Figure 4.8). This is the standard approach used in this study. However, one can require a tighter constraint like $\mathbf{c}_{\rm SN} > 0.5$ if an increase in purity (Eq. 4.2), in detriment of the efficiency (Eq. 4.1), is preferred.

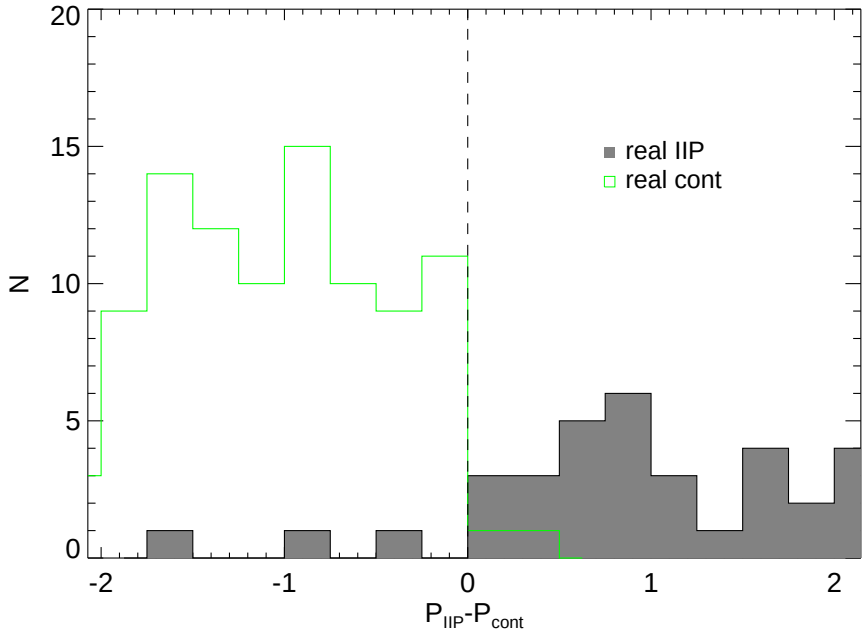

Figure 4.8: Difference of final probabilities of being a SN IIP or a non-IIP for all SNe of the SDSS-II sample. The filled histogram represents real spectroscopic SNe IIP and the green histrogram are the contaminants (here SNe Ia). A SN IIP is tagged if $P_{\rm IIP} - P_{\rm cont} > 0$.

4.4.4 Variation of fitting conditions

There are several factors in this method that can considerably affect the typing quality. Two major elements considered in this section are: a) the post-maximum time range allowed in the fit, represented by the initial τ_i^b and final τ_f^b epochs, for each bandpass filter b; and b) the amount of data required for the fit. Here, we explore these variables and find the optimal ones for each survey by maximizing the FoM.

Fit duration

For simplicity, we always assume $\tau_i^b = 0$, i. e. the initial fitting epoch always corresponds to the epoch of maximum flux. This assumption is expected to be quite accurate except for just a couple of days in longer wavelength bands, for which the plateau phase might start later. We investigate different combinations of τ_f^b, the final fitting epoch, ranging from 20 to 100 days after maximum. Generally τ_f also happens later for redder filters. For each combination, we calculate the FoM (Eq. 4.3) and find the values for which it is optimized. We find that a good typing is achieved by fitting longer periods for longer wavelengths and shorter periods for shorter ones, as it is expected due to the SN IIP color evolution. The day ranges used for all surveys are shown in Table 4.3.

Data requirements

Besides the initial signal-to-noise cull required for the bluer bands of the SDSS, simulated DES and LSST (see section 4.3), we also investigate different number of data points required in the fit. Normally a minimum of 2 data points per band is needed to fit a line. However, for data with long absence of points, like for the low-z sample, the fit might be driven by only the initial part of the assumed plateau and no posterior data, or vice-versa. We can avoid misidentifications of SNe IIP by requiring data more evenly sampled in the fit, like at least one epoch in the first half of the fit range and at least another point in the second half. By doing this, we might affect the recovery efficiency but we will ensure a purer sample. Several combinations of data requirements were investigated but we found the best FoM results for two cases: a) one data point in each, the first and second, half of the fitted region, or b) three data points in the whole range fitted. The final data requirements per SN sample are also shown in Table 4.3.

The results for the duration of the fit and the number of data required in the fit were found by investigating a variety of combinations of these in the different bands. Figure 4.9 shows how the FoM is affected by the choice of these parameters for a combined low-z, SDSS and SNLS dataset. Each x-value corresponds to a particular set of combinations, $x = 0$ is for example a typing study requiring one data point in each, the first and second half, of a $0 - 20$ days fit range in rest-frame for all survey bands. The case $x = 14$, where the maximum FoM is found (for no redshift information), corresponds to three data points in three evenly spaced sections of a $0 - 50$ day range in each band. With redshift information, the best FoM occurs at $x = 28$, where 2 data points are required in the range of $0 - 20$ days for the $u_{2.5m}/us$- and $g_{2.5m}/gs$ -bands, and 2 data points in the range $0 - 40$ days for $r_{2.5m}/rs$- and $i_{2.5m}/is$ -bands.

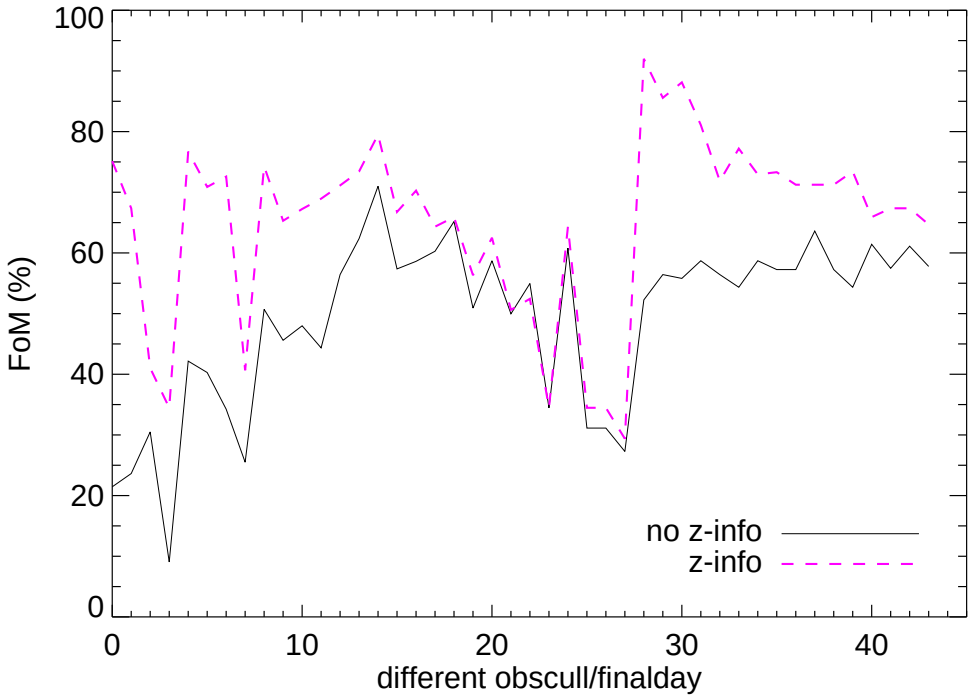

Figure 4.9: Figure of Merit (FoM) as a function of different combinations of required data and duration of the fit in the different bands. The solid/dashed lines represent studies for a combined low-z, SDSS and SNLS sample with/without redshift information.

Table 4.3: Duration and data requirement of fitted region for each SN sample (real and simulated). Numbers in parenthesis are for the sets with spec-z or host-z information, when available

SAMPLE	Data$^{\diamond}$	Filter 1	Final day*	Filter 2	Final day*	Filter 3	Final day*	Filter 4	Final day*	Filter 5	Final day†
Low-z (with z_{sp})	2h(2h)	U	30(25)	B	45(40)	V	50(50)	R	65(60)	I	65(60)
SDSS (with z_{sp})	3t(3t)	$u_{2.5m}$	20(25)	$g_{2.5m}$	25(30)	$r_{2.5m}$	30(35)	$i_{2.5m}$	35(45)	$z_{2.5m}$	35(45)
SNLS (with z_{sp})	2h(3t)	gs	30(20)	rs	45(25)	is	60(30)	zs	65(35)	–	–
DES (with $z_{ph}^{\rm host}$)	2h(3t)	$DESg$	40(40)	$DESr$	50(45)	$DESi$	55(60)	$DESz$	65(65)	–	–
DES-post-mortem (with $z_{ph}^{\rm host}$)	3t(3t)	$DESg$	35(30)	$DESr$	50(45)	$DESi$	60(55)	$DESz$	75(65)	–	–
LSST (with $z_{ph}^{\rm host}$)	1h(1h)	$LSSTu$	20(20)	$LSSTg$	25(30)	$LSSTr$	30(35)	$LSSTi$	45(45)	$LSSTz$	45(45)
LSST-post-mortem (with $z_{ph}^{\rm host}$)	3t(3t)	$LSSTu$	40(20)	$LSSTg$	50(25)	$LSSTr$	60(45)	$LSSTi$	70(60)	$LSSTz$	70(60)

$\diamond$The data required is either: a) two data points, one in the first half of the fitted region ("2h"), or b) three data points in the full fitted region ("3t")

$*$The final day after maximum brightness

†The day for filter 5 is not separately fitted, but the same day as filter 4 is used.

4.4.5 Redshift information

In our fitting method, the redshift knowledge allows us to improve the fits by correcting the SN epochs to rest-frame, so that the right portion of the light-curve is allowed in the fit. Although the final epochs, τ_f^b, of the fits are optimized for each survey (see previous section), in samples with large redshift ranges, the use of the same final epoch across different redshifts will lead to biases in the fit parameters. A redshift prior, spectroscopic or photometric, should reduce this effect by correcting all epochs by a $(1+z)$ factor. We investigate the inclusion of spectroscopic redshifts for the low-z, SDSS-II, SNLS and host photometric redshifts for the DES and LSST simulated samples.

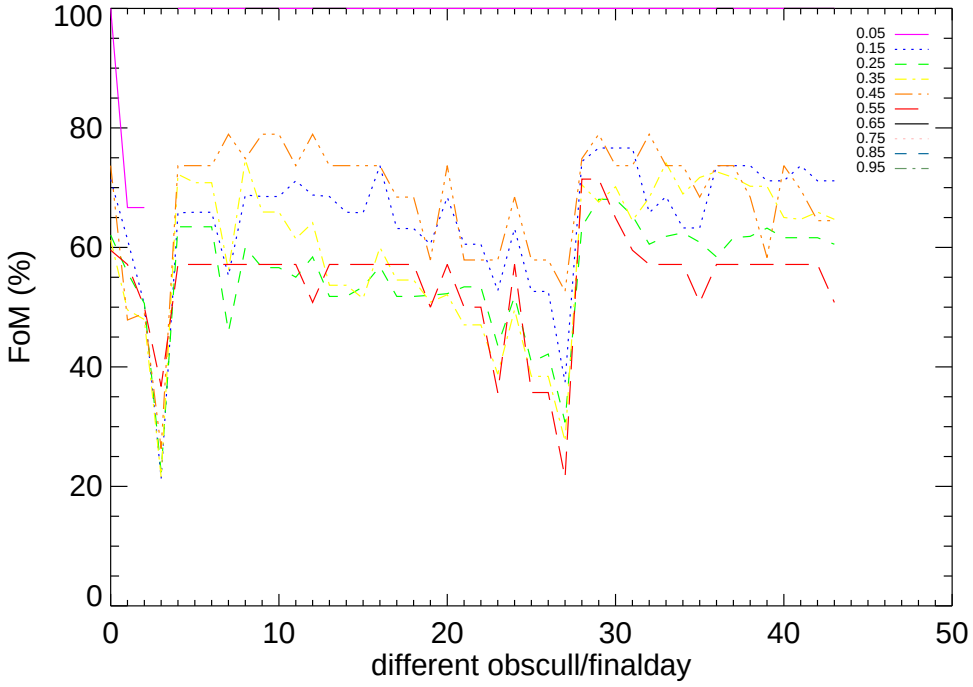

Figure 4.10: Figure of Merit (FoM) as a function of different combinations of required data and duration of the fit. The different lines represent studies in different 0.1 redshift bins of the DES simulated data set with host-z information.

Furthermore, in the case where the light-curves of SNe IIP, or other types, evolve with redshift due to intrinsic variation, or observational biases, by dividing the training sample into redshift bins, we can include those effects in the typing technique. This binned typing trains each z-bin separately and finds independent optimal slope-slope and slope-flux distributions for each one. Thus, two SNe with the same fit slopes and fluxes but at different redshifts might have different SN IIP probabilities. For this method to be possible, one needs a good training sample with enough SNe covering all redshifts. We implement it uniquely for the DES and LSST simulated samples, where there are enough SNe in each bin.

Additionally, when redshift information is available, the search for optimal fitting conditions, like the fit duration and data requirements presented in last section, can be separated for different redshift bins. The procedure is shown in Figure 4.10 for the simulated DES survey with host-z information. Each line shows a different 0.1 redshift region up to $z = 1.0$. One can see that the FoM is not always optimized for the same combination. The resulting fit durations differ as a function of redshift, as shown in Figure 4.11. This is partly due to the extension of the relevant light-curve portions in the observer frame at higher redshift, but also to a different sampling of the light-curve at different redshifts depending on the survey characteristics.

The typing with redshift information (and binned training) only improves the FoM by a few percent. The results with no redshift information are remarkably similar (see Table 4.5 and Figures 4.13 and 4.14).

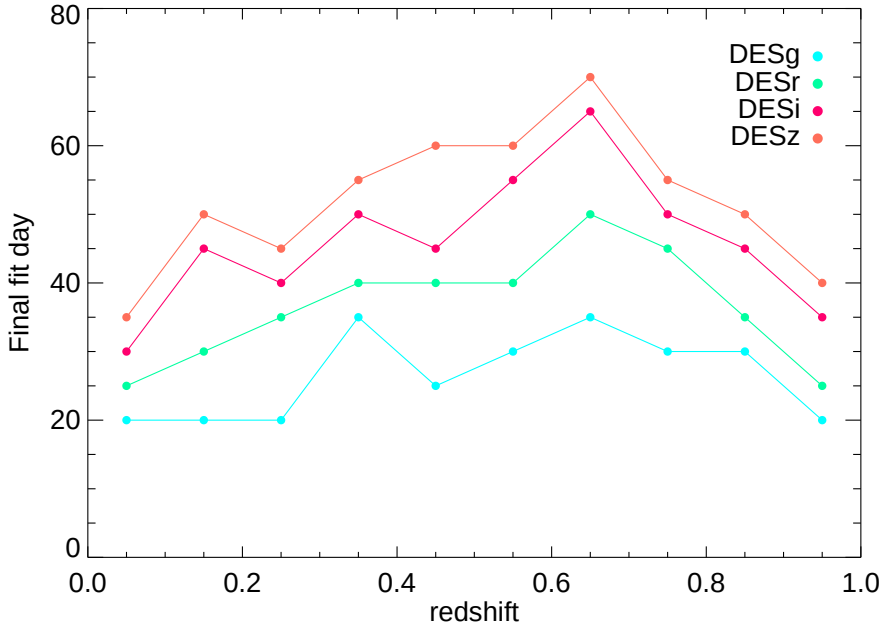

Figure 4.11: Fit range per band for different redshift bins of the simulated DES sample

4.4.6 Training set

In this section we explore the importance of the training setd provided by K10 for the DES and LSST typing, and provide other ones that are more representative of the full population.

The original spectroscopic training sets of the simulated samples were based on limiting magnitudes (e. g. 21.5 mag in the $DESr$-band for a 4m telescope and 23.5 mag in the $DESi$-band for a 8m telescope, see K10) that lead to a heavy bias in the spectroscopic redshift distribution compared to the full sample. The SNe IIP of the training sets go only to $z \sim 0.6 - 0.7$,

while for the entire sample they extend all the way to $z \sim 1.1$ (see Table 4.1). More than 50% of the plateau supernovae are in a regime that is not probed by the training sample. These SNe have quite different, noisier and less sampled light-curves, which greatly decreases the typing efficiency at higher-z. Moreover, the ratio of SNe Ia to other SN types is over-represented in the training sets. All these biases lead to a training set that is not representative of the real dataset and will affect negatively the performance of the classification. This issue can clearly be seen in the results of the SN challenge, for which most of the methods presented did much worse when run on the training sets themselves. Here, we find that the spectroscopic sets have FoMs of 78% (DES) and 64% (LSST), dropping down to 31% (DES) and 21% (LSST) for the entire sample (see Table 4.5).

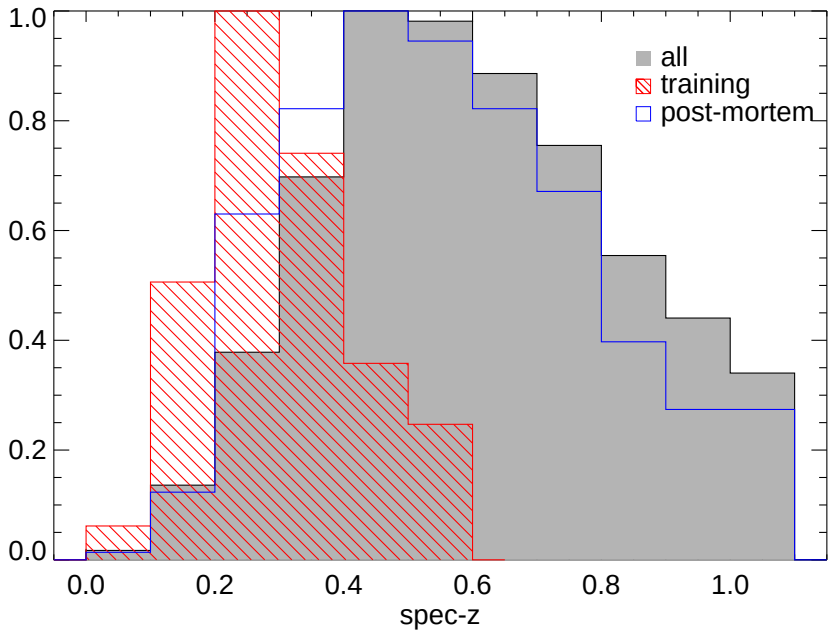

Figure 4.12: Redshift distribution of the entire simulated DES sample normalized to peak (gray shaded), the provided training sample (red diagonal), and the post-mortem training sample (blue empty)

We therefore attempt using a different training subset to classify all SNe. As proposed by Richards et al. (2011), by increasing the deepness of the survey (e. g. to 23.5 mag for the $DESr$-band) and randomly picking up SNe below this limit, higher-z regimes are covered and a better representation of the sample is achieved (see Figure 4.12 for the DES sample). We decrease the efficiency parameters for spectroscopic observation (Equation 2 and Table 3 of K10) to have a similar number of spectroscopic objects than the original one, as shown in Table 4.1. We name the typing of the full sample based on this new training sample, the "post-

mortem" DES/LSST samples. The final efficiencies and FoMs are much improved: 63% (DES) and 58% (LSST) and are shown in Figures 4.13 and 4.14. The purities drop slightly due to a lower number of contaminant (non-IIP) objects in the post-mortem training sample compared to the original sample.

4.5 Results

Our final efficiencies, purities and FoMs are summarized in Table 4.4 for all surveys. We note that these were obtained in order to optimize the FoM, regardless of the separate efficiencies and purities. Nevertheless, we find that the purities for all real and simulated samples are higher than $\sim 80\%$. This shows that this technique is a robust SN IIP photometric typing independent of the redshift range and applicable for a variety of surveys.

The efficiencies calculated here represent a percentage of the *full* samples, before light-curve selection cuts and other culls. For the real datasets, they are normally higher than 80% but go as low as 70% for the low-z sample due to the scarcely sampled light-curves that do not pass the data requirements for the fit (see section 4.4.4). On the other hand, the complete simulated samples have very low efficiencies, lower than 40%, pulling also the FoMs down. Two important factors affect the efficiency of the simulated samples: a) a training sample that does not span to high redshifts, and b) very noisy and poorly sampled data, especially at high redshift, that either is culled out, or that affects the maximum epoch estimate or the post-maximum fit.

We address the first concern by selecting a different training sample of the same size but deeper in brightness (see section 4.4.6). The obtained efficiencies increase by 30-40%. We show the results as a function of redshift for both simulated samples in Figures 4.13 and 4.14. The full sample trained with the original spectroscopic subset (dashed lines) decrease with redshift very fast. The post-mortem analysis (solid lines), on the other hand, remain constant with redshift. We therefore agree with the findings of Newling et al. (2011) and Richards et al. (2011) that a better training sample, more representative of the full set, is needed for accurate typing. Similarly to Newling et al. (2011), we find that our technique performs very well without any redshift information benefiting only a small percentage from the inclusion of a redshift analysis.

We cannot do much to directly address the second concern of some poor quality light-curves in the simulated data. However, to quantify the effect of these in the final efficiencies and FoMs, we can calculate the efficiencies respect to the culled sample instead of the full sample. By requiring a new "culled sample" consisting of only SNe with enough data points in the fitted region (as in section 4.4.4), and with high signal-to-noise for the simulated surveys

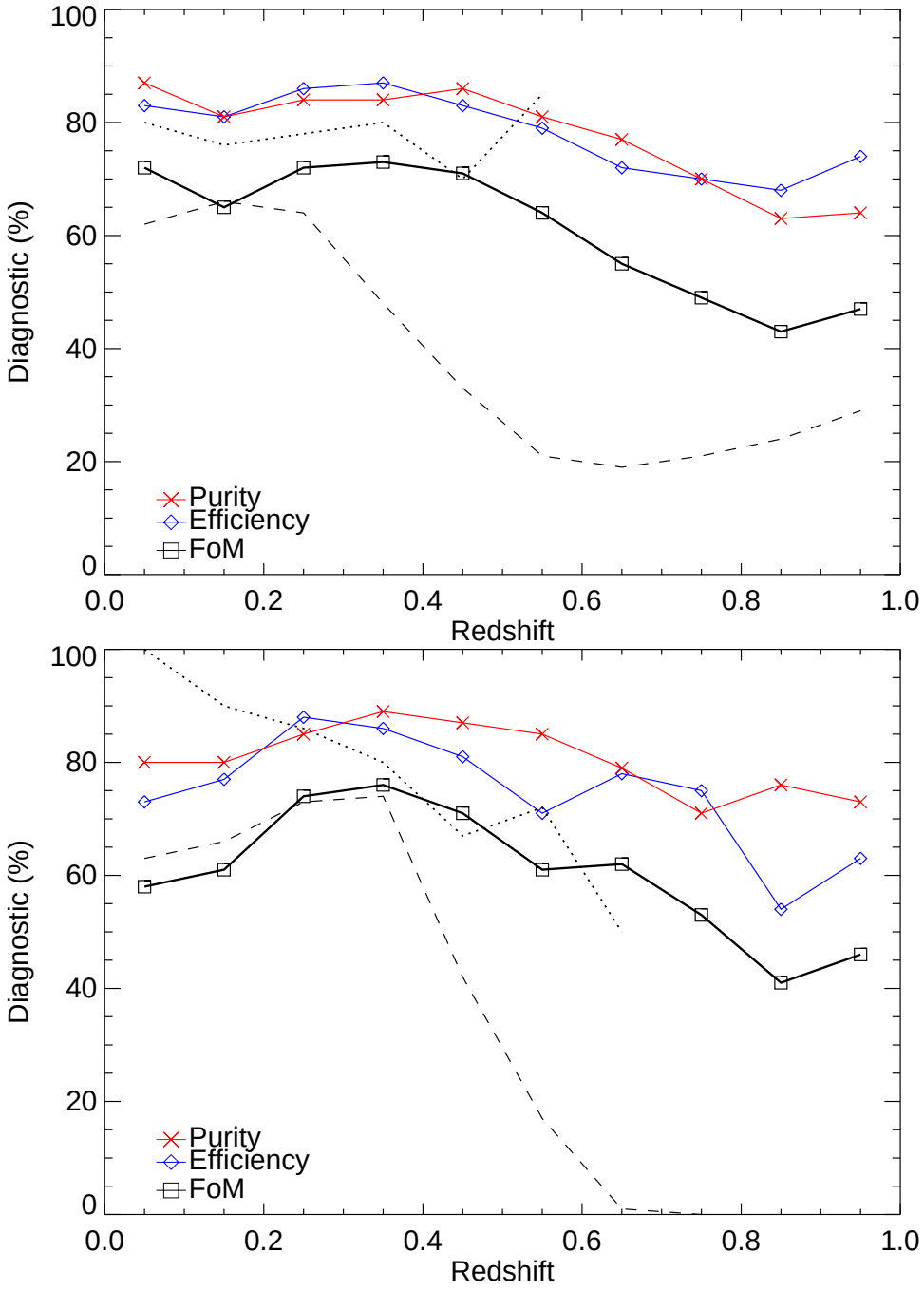

Figure 4.13: Figure of Merit (FoM) (black squares and lines), efficiency (blue diamonds and lines) and purity (red crosses and lines) as a function of redshift for the DES sample trained with the post-mortem set without prior redshift information (*upper*) and with host photometric redshift information (*lower*). The dashed line is the FoM for the DES challenge (based on the original training sample) and dotted line for the FoM of just the original DES training set.

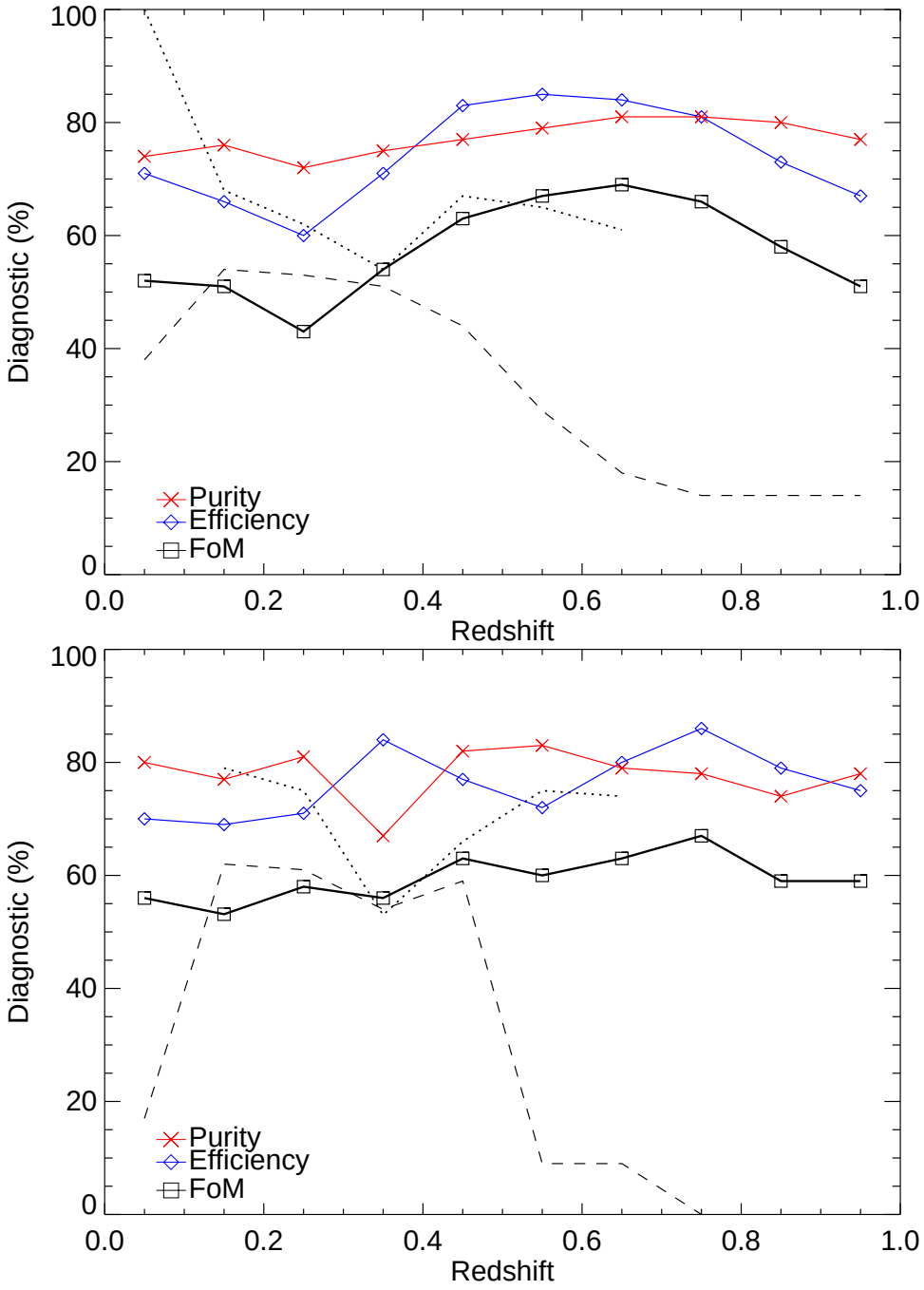

Figure 4.14: Figure of Merit (FoM) (black squares and lines), efficiency (blue diamonds and lines) and purity (red crosses and lines) as a function of redshift for the LSST sample trained with the post-mortem set, without prior redshift information (*upper*) and with host photometric redshift information (*lower*). The dashed line is the FoM for the LSST challenge (based on the original training sample) and dotted line for the FoM of just the original LSST training set.

($S/N > 3$), we obtain the results quoted in the last column of Table 4.5. These are clearly higher, especially for the low-z and simulated samples, for which the efficiencies were particularly low. By doing this, the decrease in the number of tagged SNe IIP tagged is $8 - 25\%$. To ensure a better estimate of the day of maximum brightness, we can include the requirement of at least one pre-maximum data. For the low-z sample, the efficiency increases to 94% in this case, but the decrease in the number of tagged SNe IIP is much larger than 60%. This shows the importance of quality data to obtain higher efficiencies.

4.6 Conclusions

The technique presented here, albeit simple, has great power to select SNe IIP across a wide range of redshifts and surveys. It is based on simple linear fits in magnitudes to multi-band photometry and the analysis of the fitted parameter spaces. Without the need of redshift knowledge, it also avoids the cumbersome use of templates and K-corrections, and any evolutionary effects related to them.

The method is quite robust at separating SNe IIP from other SNe with purities higher than 80% for all real and simulated datasets considered. The highest source of misidentification are SNe IIn, which may also have shallow decline rates after maximum brightness. The SN IIP efficiencies are higher than 60% for all redshifts as long as proper training samples, representative of the full sample, are used. They can be further increased with high-quality well-sampled photometry. Additional redshift information, such as host photo-z, provides an increase in the FoM of a few percent.

The method introduced here is easily implemented for current and coming transient surveys. As the number of SNe multiply, and the cadence becomes shorter, the technique provides a fast and secure way of photometrically classify plateau supernovae.

Table 4.4: Efficiencies, purities and FoMs for each SN sample (real and simulated). Numbers in parenthesis are for the sets with spec-z or host-z information, when available

SAMPLE	$N_{\rm IIP}$	$N_{\rm IIP}^{\rm true}$	$N_{\rm cont}$	$N_{\rm IIP}^{\rm false}$	Efficiency	Purity	FoM	Culled-FoM
Low-z (with z_{sp})	38	35(35)	336	2(1)	0.92(0.92)	0.96(0.97)	**0.88(0.89)**	**0.92(0.93)**
SDSS (with z_{sp})	34	34(34)	95	0(0)	1.00(1.00)	1.00(1.00)	**1.0(1.0)**	**1.0(1.0)**
SNLS (with z_{sp})	12	12(12)	381	0	1.00(1.00)	1.00(1.00)	**1.00(1.00)**	**1.00(1.00)**
Low-z+SDSS+SNLS (with z_{sp})	46	33(33)	629	9(1)	0.91(0.91)	0.79(0.96)	**0.72(0.87)**	**0.79(0.87)**
DES-training (with $z_{ph}^{\rm host}$)	236(218)	198(201)	1043(1038)	8(15)	0.84(0.92)	0.96(0.93)	**0.81(0.85)**	**0.91(0.92)**
DES-challenge (with $z_{ph}^{\rm host}$)	8637(8643)	3196(3112)	9678(9710)	655(424)	0.37(0.36)	0.83(0.88)	**0.31(0.32)**	**0.42(0.43)**
DES-post-mortem (with $z_{ph}^{\rm host}$)	8637(8643)	6737(6828)	9678(9710)	1580(1499)	0.78(0.79)	0.81(0.82)	**0.63(0.65)**	**0.72(0.79)**
LSST-training (with $z_{ph}^{\rm host}$)	233	166(178)	539	19(21)	0.71(0.76)	0.90(0.90)	**0.64(0.68)**	**0.79(0.79)**
LSST-challenge (with $z_{ph}^{\rm host}$)	26252	6891(8663)	16523	1513(1528)	0.26(0.33)	0.82(0.85)	**0.21(0.28)**	**0.33(0.35)**
LSST-post-mortem (with $z_{ph}^{\rm host}$)	26252	19540(19479)	16523	5511(5178)	0.74(0.74)	0.78(0.79)	**0.58(0.59)**	**0.70(0.71)**

Chapter 5

Summary and Outlook

The importance of supernovae should not be underestimated. Supernovae are fundamental for life (you would not be reading this without them) and they are a key feature in the life cycle of stars. The mechanisms involved in the explosion are a probe of fundamental physics, where the four forces of nature play an essential role. The frequency of their occurrence throughout the history of the universe and the high energy released have made them a favorite explanation of unanswered questions in astronomy such as energy input in collapsing molecular clouds for star formation or AGN feedback. Despite several efforts, pivotal problems in explaining their nature remain. This thesis contributes to the understanding of these explosive events.

5.1 Type Ia supernovae

Believed to come from low-mass stars that end their lives as exploding white dwarfs in a binary system, type Ia supernovae have been essential for cosmology for more than a decade. However, despite several efforts, the nature of the companion star donating mass, and the physics of the explosion are still a mystery and a source of systematic uncertainty in the determination of the equation of state of dark energy.

The faintest of SN Ia explosions, "subluminous" objects, are several magnitudes dimmer than typical SNe Ia; they are very short-lived and have extreme red colors. They have been hard to include in a common comprehensive progenitor and explosion scenario, and they had to be left out of cosmological studies, despite contributing to $\sim 18\%$ of the nearby SN Ia rate. This thesis has addressed some fundamental questions of SNe Ia, particularly subluminous SNe Ia.

We have searched for subluminous SNe Ia in the SNLS at redshifts higher than $z > 0.1$, where they remained previously unobserved. We found a fraction of 18 low-stretch SNe Ia up to $z = 0.6$ showing that they constitute a natural continuation of the population even at high

redshift. They have similar photometric properties than the local sample and they are also found in sites of low star formation. The measured rate as a function of redshift is consistent with a constant or decreasing fraction with redshift, compared to the increasing normal SN Ia rate. This confirms that the SN Ia population mix evolves with redshift. Subluminous SNe Ia do not follow the cosmic star formation history (even less than normal SNe Ia) and probably come from a population of lower mass progenitors (or higher metallicity) than other SNe Ia.

The search for evolution of SN Ia properties is extremely important for cosmological analyses. Numerous studies show that the evolutionary bias is low. We find an interesting population of bluer low-stretch SN Ia candidates at $z \gtrsim 0.7$. This set has a definite different color distribution that is abnormal for those light-curve widths, but they are found at the limiting magnitude of the SNLS. Several attempts were made to discard these objects, as SN Ibc contaminants, or through larger photometric uncertainties, but their origin remains unknown. If their properties turn out to be real, they could either represent a new class of transients with faint and fast-evolving light-curves and passive hosts, or they are a yet unknown potential evolutionary state of SNe Ia.

This thesis also presented the rise-time study of a large variety of SN Ia light-curves, particularly the subluminous SNe Ia previously found. Using the well-sampled data of the SNLS but also the published data of the SDSS and some other nearby SNe Ia, we K-corrected all data points to rest-frame B-band and overlaid them all together to study the rise-time behavior. By grouping the SNe Ia by stretch, we investigate possible differences in the early portion of the light-curve. We find that all SNe Ia, from low- to high-stretch, including subluminous ones, when stretch-corrected, are well represented by a quadratic rise to maximum brightness lasting approximately 17.00 days for the template we use. At a 1σ level, the wide variety of SN Ia explosions all agree with this behavior.

Different rise-times among SN Ia populations would have important consequences that could hint towards additional parameters shaping the explosions, particularly in the outer layers (e. g. Höflich et al. 2010; Fink et al. 2010). Although we observe a possible trend of longer rise-times for lower stretch objects, after stretch-correction, the different samples are consistent within the errors. We find no need for a separate independent component to model the early rise of the light-curve. To the level reached by the data, secondary parameterizations besides stretch do not significantly improve the light-curve modeling, not even a two-stretch parameterization as found in other studies. This shows once again that SNe Ia are an extremely homogenous sample throughout the entire light-curve. This is remarkable considering the ample range of luminosities and colors covered by all SNe Ia. It argues for a common explosion mechanism and keeps cosmologists tranquil.

Lastly, I would like to point out an important evolution in the SN Ia paradigm since the

start of this thesis. For many years, the scientific community recognized the value of the double degenerate scenario, but it was often overshadowed by the single degenerate mechanism to SNe Ia with arguments of theoretical robustness. It was seen as unlikely to drive a thermonuclear runaway via the merger of two WDs. Nowadays, there still are theoretical drawbacks for the DD scenario, although advances are being made, but the viewpoint is shifting thanks to the multiple observational evidences that argue against the SD path as the main source for SNe Ia.

The consistent lack of hydrogen in the spectra, the missing observed X-ray emission from their accreting progenitor systems, the confirmed existence of a number of super-Chandrasekhar explosions, the lack of signature of companions in the early portion of the light-curves, and the discrepant delay-time distributions inferred from the SN Ia (and SN Ia remnant) rate evolution in different environments, strongly question the SD viability for most SNe Ia.

The need for another channel propels the DD scenario. Despite its theoretical counterarguments, this mechanism is in harmony with most of the mentioned observations. It would also naturally explain the relation between environments and SN Ia properties: brighter and more energetic SNe Ia would come from more massive progenitors, more common in star-forming regions while fainter and less energetic SNe Ia are the result of less massive progenitors happening in more evolved passive environments. Furthermore, recent theoretical studies have revived the possibility of sub-Chandrasekhar explosions. The fraction of WD mergers whose total mass is below the Chandrasekhar limit can easily explain the total rate of SNe Ia, the only empirical evidence missed by the regular DD scenario.

This picture of SN Ia progenitors is especially suited for subluminous SNe Ia. As this work has shown, their early-type environments all the way to high redshift and the DTD fits to their rate strongly suggest a low mass origin. Being ten times fainter and with very low ^{56}Ni masses synthesized, they are hard to reconcile with Chandrasekhar mass explosions. As a matter of fact, successful subluminous explosions have been produced via sub-Chandrasekhar deflagrations or through WD mergers. From the subluminous SN Ia perspective, there is no better progenitor scenario than the merger of two WDs in a binary of low total mass producing a weak sub-Chandrasekhar explosion (although the predicted fraction might be low, see Meng et al. 2011).

If SNe Ia have so similar light-curves (after stretch-correcting) and spectra suggesting a real common origin, and subluminous are the extreme end of the population (Doull & Baron 2011), it is quite tempting to sustain that their progenitors are the lowest mass end of a continuous WD mass distribution that could extend all the way to the progenitors of super-Chandrasekhar SNe Ia at the other end. Admittedly, common explosion physics producing such a huge range of output properties have been difficult to model and require an incredible effort that only

recent and future simulating techniques and computational power will be able to solve. On the other hand, recurring to different progenitors scenarios for such homogeneous events seems increasingly improbable.

The next years of SN Ia science will certainly continue to see a rapid evolution in our understanding of the underlying physics. New surveys at low and high redshift open up exciting possibilities to soon reveal their true nature. The Palomar Transient Factory (PTF; Law et al. 2009; Rau et al. 2009) for instance can study the nature of subluminous SNe Ia in more detail and even find fainter and/or rare unseen objects (Sullivan et al. 2011b) that could provide the missing pieces of the SN Ia puzzle. Comprehensive surveys like the Catalina Real-Time Transient Survey (CRTS; Drake et al. 2009), CHASE (Pignata et al. 2009), Pan-STARRS (Tonry & Pan-STARRS Team 2005) and future Dark Energy Survey (DES; Bernstein et al. 2009), Skymapper (Schmidt et al. 2005) and the Large Synoptic Survey (LSST; Ivezic et al. 2008) will study SN Ia environments across different redshifts and their rate evolution for increasingly accurate determinations of the delay-times. Better cadence since the early times after explosion will further constrain progenitor radii from the interaction in the ejecta seen in the light-curve rise portion, possibly ruling out main-sequence companions as has been done for red giant companions. Finally, the future improvement of SN Ia science will contribute to precision cosmology with better-understood systematics (besides the increase in the number of objects studied). The elusive nature of the dark energy may be apprehended once we also nail the nature of SNe Ia.

5.2 Plateau supernovae

Plateau supernovae are the most common of all supernovae. They are core-collapse SNe from progenitors of initial masses between $8 - 17\mathrm{M}_{\odot}$. Their optical light-curve is easily recognizable with a characteristic plateau after maximum brightness. The study of core-collapse supernovae is in a more infant state than SNe Ia. The prioritization of SNe Ia for cosmology and the –in principle– better understood progenitors and explosions of CC SNe has left them somewhat straggled. Nevertheless, due to their high rate and the rolling technologies of current (and coming) surveys, many unanalyzed SN IIP light-curves are stored in the databases. Quality photometry allows very interesting scientific studies but we need proper classification algorithms, hopefully automated for the huge coming transient searches.

In this thesis, we have introduced a simple and effective photometric typing technique for SNe IIP. It uses linear magnitude fits to multi-band post-maximum data and post-maximum fluxes to find appropriate regions of high SN IIP probability to select candidates. We tested the technique with current low-z and high-z data, and with simulated coming surveys. We find

the method to be very accurate at discriminating SNe IIP; the tagged samples are always more than 80% pure. The fraction of SNe IIP typed respect to the entire set varies a lot depending on the survey. We find that these IIP efficiencies can be improved with better spectroscopic training samples that are more characteristic of the entire samples. Good data, evenly sampled across all epochs, particularly prior to maximum and during the plateau phase ensures a higher fraction of selected SNe IIP.

Preliminary studies of our sIImP method employed on the SNLS database reveal a photometric SN IIP dataset of ~ 350 objects with host photo-z's up to $z \sim 0.7$. This exceeds by far the number of published plateau supernovae and reaches unprecedented redshifts. Multiple interesting scientific studies can be performed with this dataset.

A first interesting analysis is a measurement of the SNLS IIP rate as a function of redshift. Previous measurements at high-z grouped all core-collapse SNe together (Dahlen et al. 2004; Bazin et al. 2009; Graur et al. 2011), which involves interesting research topics like an observed missing fraction (compared to the massive star formation rate) due possibly to obscuration or weak SNe (Horiuchi et al. 2011). Measuring the SN IIP rate individually, however, has also a very important scientific value. Being directly related to the star formation history of the universe, the normalization of the rate would give us the IMF fraction of massive stars that lead to such explosions, providing thereby a direct measure of the progenitor mass range. With the current non-detection of progenitors with $M_{\rm ZAMS} > 17{\rm M}_{\odot}$, an independent upper mass limit would test these results. This study is a natural high-priority follow-up that will benefit from the tools developed for the SN Ia rate measurement.

Considerable effort has been dedicated to characterize and understand the light-curves of SNe IIP, particularly the plateau phase (e. g. Nadyozhin 2003) but also the early times (Cowen et al. 2010). Theoretical and hydrodynamical models try to relate SN physics such as explosion energy, ^{56}Ni mass produced, progenitor mass and radius, with observational properties like plateau duration and luminosity, and expansion velocities (e. .g Tominaga et al. 2009; Utrobin & Chugai 2009; Dessart & Hillier 2011; Bersten et al. 2011). This led to the recognition of SNe IIP as distance indicators, potentially even in the UV (Gal-Yam et al. 2008). Kasen & Woosley (2009) have even suggested a 20% accuracy in distance estimation based solely on photometric SN IIP parameters. The large photometric dataset of the SNLS opens up the opportunity to study a variety of aspects of SN IIP light-curves, their relation to physics and their standardization capabilities. This dataset is the exact high-z counterpart to nearby SN IIP studies (e. g. Poznanski et al. 2009; D'Andrea et al. 2010) that is needed to understand possible evolution and their viability as cosmological rulers. Again, we will benefit from the developments in the study of the rise-time of SN Ia light-curves.

If SNe Ia have turned to be one of the favorite transients studied by astronomers in the

past decades, type IIP and other core-collapse supernovae are on the way of becoming as, or even more exciting. Large numbers will be discovered by future surveys, even if it is as a side product of large SN Ia searches. With reliable typing techniques and good quality data, we might be able to fully understand the final stages of massive stars, how they explode, when they occur and if they always have an optical display.

Plateau supernovae might become a new robust independent cosmological probe. With their better-understood progenitors and atmosphere physics, as well as their abundance (particularly at higher redshift where the cosmic star formation increases), they will offer a unique cosmological tool for future surveys such as the aforementioned LSST, the proposed Joint Dark Energy Mission (JDEM), the James Webb Space Telescope (JWST) and future large-class telescopes.

Bibliography

Agnoletto, I. et al. 2009, ApJ, 691, 1348

Aguirre, A. 1999, ApJ, 525, 583

Aldering, G., Knop, R., & Nugent, P. 2000, AJ, 119, 2110

Aldering, G. et al. 2006, ApJ, 650, 510

Altavilla, G. et al. 2004, MNRAS, 349, 1344

Anderson, J. P. & James, P. A. 2008, MNRAS, 390, 1527

—. 2009, MNRAS, 399, 559

Anupama, G. C., Sahu, D. K., & Jose, J. 2005, A&A, 429, 667

Anupama, G. C. et al. 2009, MNRAS, 392, 894

Arnett, W. D. 1969, Ap&SS, 5, 180

—. 1982, ApJ, 253, 785

Arnett, W. D., Branch, D., & Wheeler, J. C. 1985, Nature, 314, 337

Astier, P. et al. 2006, A&A, 447, 31

Aubourg, É. et al. 2008, A&A, 492, 631

Baade, W. & Zwicky, F. 1934, Proceedings of the National Academy of Science, 20, 254

Bailey, S. et al. 2009, A&A, 500, L17

Balland, C. et al. 2009, A&A, 507, 85

Barbon, R., Buondí, V., Cappellaro, E., & Turatto, M. 1999, A&AS, 139, 531

Barbon, R., Ciatti, F., & Rosino, L. 1973, A&A, 29, 57

—. 1982, A&A, 116, 35

Baron, E. et al. 2004, ApJ, 616, L91

Barris, B. J. & Tonry, J. L. 2006, ApJ, 637, 427

Bartunov, O. S., Tsvetkov, D. Y., & Filimonova, I. V. 1994, PASP, 106, 1276

Bazin, G. et al. 2009, A&A, 499, 653

Bazin, J. et al. 2011, in preparation

Benetti, S., Cappellaro, E., Danziger, I. J., Turatto, M., Patat, F., & della Valle, M. 1998, MNRAS, 294, 448

Benetti, S., Cappellaro, E., & Turatto, M. 1991, A&A, 247, 410

Benetti, S. et al. 1994, A&A, 285, 147

—. 2001, MNRAS, 322, 361

Bernstein, J. P., Kessler, R., Kuhlmann, S., & Spinka, H. 2009, ArXiv:0906.2955

Bersten, M. C., Benvenuto, O., & Hamuy, M. 2011, ApJ, 729, 61

Bethe, H. A., Brown, G. E., Applegate, J., & Lattimer, J. M. 1979, Nuclear Physics A, 324, 487

Bethe, H. A. & Wilson, J. R. 1985, ApJ, 295, 14

Bianco, F. B. et al. 2011, ArXiv e-prints

Bildsten, L., Shen, K. J., Weinberg, N. N., & Nelemans, G. 2007, ApJ, 662, L95

Bionta, R. M., Blewitt, G., Bratton, C. B., Casper, D., & Ciocio, A. 1987, Physical Review Letters, 58, 1494

Blanton, E. L. et al. 1995, AJ, 110, 2868

Blondin, J. M., Mezzacappa, A., & DeMarino, C. 2003, ApJ, 584, 971

Bogomazov, A. I. & Tutukov, A. V. 2011, ArXiv e-prints

Boissier, S. & Prantzos, N. 2009, A&A, 503, 137

Botticella, M. T. et al. 2008, A&A, 479, 49

Boulade, O. et al. 2003, in Society of Photo-Optical Instrumentation Engineers (SPIE) Conference Series, Vol. 4841, Society of Photo-Optical Instrumentation Engineers (SPIE) Conference Series, ed. M. Iye & A. F. M. Moorwood, 72–81

Branch, D. 1992, ApJ, 392, 35

Branch, D., Chau Dang, L., Hall, N., Ketchum, W., Melakayil, M., Parrent, J., Troxel, M. A., Casebeer, D., Jeffery, D. J., & Baron, E. 2006, ArXiv Astrophysics e-prints

Branch, D. et al. 2002, ApJ, 566, 1005

Brandt, T. D., Tojeiro, R., Aubourg, É., Heavens, A., Jimenez, R., & Strauss, M. A. 2010, AJ, 140, 804

Bravo, E. & García-Senz, D. 2008, A&A, 478, 843

Bravo, E. et al. 2010, ArXiv e-prints

Bronder, T. J. et al. 2008, A&A, 477, 717

Brown, P. J. et al. 2007, ApJ, 659, 1488

Bruenn, S. W. 1985, ApJS, 58, 771

Buras, R., Rampp, M., Janka, H.-T., & Kifonidis, K. 2003, Physical Review Letters, 90, 241101

Burrows, A. 1988, ApJ, 334, 891

—. 1990, Annual Review of Nuclear and Particle Science, 40, 181

—. 2000, Nature, 403, 727

Burrows, A. & Goshy, J. 1993, ApJ, 416, L75+

Burrows, A. & Lattimer, J. M. 1986, ApJ, 307, 178

Burrows, A., Livne, E., Dessart, L., Ott, C. D., & Murphy, J. 2006, ApJ, 640, 878

Buta, R. J. & Turner, A. 1983, PASP, 95, 72

Candia, P. et al. 2003, PASP, 115, 277

Cappellaro, E., Evans, R., & Turatto, M. 1999, A&A, 351, 459

Cappellaro, E. et al. 1995, A&A, 293, 723

Chandrasekhar, S. 1931, ApJ, 74, 81

Chatzopoulos, E. et al. 2011, ArXiv e-prints:1101.3581

Chugai, N. N. et al. 2005, Astronomy Letters, 31, 792

Ciatti, F. & Rosino, L. 1977, A&A, 56, 59

Clark, J. S., Muno, M. P., Negueruela, I., Dougherty, S. M., Crowther, P. A., Goodwin, S. P., & de Grijs, R. 2008, A&A, 477, 147

Clocchiatti, A. et al. 1996, AJ, 111, 1286

Colgate, S. A. & McKee, C. 1969, ApJ, 157, 623

Conley, A. et al. 2006, AJ, 132, 1707

—. 2008, ApJ, 681, 482

—. 2011, ApJS, 192, 1

Contardo, G., Leibundgut, B., & Vacca, W. D. 2000, A&A, 359, 876

Contreras, C. et al. 2010, AJ, 139, 519

Corasaniti, P. S. 2006, MNRAS, 372, 191

Cordes, J. M., Romani, R. W., & Lundgren, S. C. 1993, Nature, 362, 133

Corsi, A. et al. 2011, ArXiv e-prints

Cowen, D. F., Franckowiak, A., & Kowalski, M. 2010, Astroparticle Physics, 33, 19

Crockett, R. M. et al. 2007, MNRAS, 381, 835

Crowther, P. A. 2007, ARA&A, 45, 177

Crowther, P. A., Dessart, L., Hillier, D. J., Abbott, J. B., & Fullerton, A. W. 2002, A&A, 392, 653

Dahlen, T. & Fransson, C. 1999, A&A, 350, 349

Dahlén, T. & Goobar, A. 2002, PASP, 114, 284

Dahlen, T., Strolger, L.-G., & Riess. 2008, AJ, 681, 462

Dahlen, T. et al. 2004, ApJ, 613, 189

Dan, M., Rosswog, S., Guillochon, J., & Ramirez-Ruiz, E. 2011, ArXiv e-prints

D'Andrea, C. B. et al. 2010, ApJ, 708, 661

Davis, M. et al. 2003, in Presented at the Society of Photo-Optical Instrumentation Engineers (SPIE) Conference, Vol. 4834, Society of Photo-Optical Instrumentation Engineers (SPIE) Conference Series, ed. P. Guhathakurta, 161–172

Dessart, L. & Hillier, D. J. 2011, MNRAS, 410, 1739

Dessart, L. et al. 2008, ApJ, 675, 644

Di Carlo, E. et al. 2002, ApJ, 573, 144

Di Stefano, R. 2010a, ApJ, 712, 728

—. 2010b, ApJ, 719, 474

Dilday, B. et al. 2008, ApJ, 682, 262

—. 2010, ApJ, 713, 1026

Domínguez, I., Höflich, P., & Straniero, O. 2001, ApJ, 557, 279

Doull, B. & Baron, E. 2011, ArXiv e-prints

Drake, A. J. et al. 2009, ApJ, 696, 870

Drenkhahn, G. & Spruit, H. C. 2002, A&A, 391, 1141

Eldridge, J. J. & Tout, C. A. 2004, MNRAS, 353, 87

Elias-Rosa, N. et al. 2006, MNRAS, 369, 1880

Ellis, R. S. et al. 2008, ApJ, 674, 51

Elmhamdi, A. et al. 2003, MNRAS, 338, 939

—. 2010, ArXiv e-print: 1001.0945

Ewan, G. T. 1992, Nuclear Instruments and Methods in Physics Research A, 314, 373

Filippenko, A. V. 1997, ARA&A, 35, 309

Filippenko, A. V., Porter, A. C., & Sargent, W. L. W. 1990, AJ, 100, 1575

Filippenko, A. V. et al. 1992a, ApJ, 384, L15

—. 1992b, AJ, 104, 1543

Fink, M. et al. 2010, ArXiv e-prints

Foglizzo, T. & Tagger, M. 2000, A&A, 363, 174

Folatelli, G. et al. 2006, ApJ, 641, 1039

—. 2010, AJ, 139, 120

Foley, R. J. et al. 2003, PASP, 115, 1220

—. 2009, AJ, 137, 3731

Ford, C. H. et al. 1993, AJ, 106, 1101

Fraser, M. et al. 2010, ArXiv e-prints

Freedman, W. L. et al. 2009, ApJ, 704, 1036

Freeman, P. E., Newman, J. A., Lee, A. B., Richards, J. W., & Schafer, C. M. 2009, MNRAS, 398, 2012

Frieman, J. A. et al. 2008, AJ, 135, 338

Fryer, C. L. 1999, ApJ, 522, 413

Gal-Yam, A. & Maoz, D. 2004, MNRAS, 347, 942

Gal-Yam, A., Maoz, D., & Sharon, K. 2002a, MNRAS, 332, 37

Gal-Yam, A., Ofek, E. O., & Shemmer, O. 2002b, MNRAS, 332, L73

Gal-Yam, A. et al. 2008, ApJ, 685, L117

—. 2009, Nature, 462, 624

Galama, T. J. et al. 1998, Nature, 395, 670

Gallagher, J. S., Garnavich, P. M., Berlind, P., Challis, P., Jha, S., & Kirshner, R. P. 2005, ApJ, 634, 210

Gallagher, J. S. et al. 2008, ApJ, 685, 752

Gamezo, V. N., Khokhlov, A. M., & Oran, E. S. 2005, ApJ, 623, 337

Garnavich, P. M. et al. 2004, ApJ, 613, 1120

Gehrels, N. 1986, ApJ, 303, 336

Gilfanov, M. & Bogdán, Á. 2010, Nature, 463, 924

Goldhaber, G. et al. 2001, ApJ, 558, 359

Gong, Y., Cooray, A., & Chen, X. 2010, ApJ, 709, 1420

González-Gaitán, S. et al. 2011, ApJ, 727, 107

Goobar, A. 2008, ApJ, 686, L103

Graur, O. et al. 2011, ArXiv e-prints

Greggio, L. 2005, A&A, 441, 1055

Guy, J. et al. 2007, A&A, 466, 11

—. 2010, A&A, 523, A7+

Habergham, S. M., Anderson, J. P., & James, P. A. 2010, ApJ, 717, 342

Hachisu, I., Kato, M., & Nomoto, K. 1996, ApJ, 470, L97+

Hachisu, I., Kato, M., Saio, H., & Nomoto, K. 2011, ArXiv e-prints

Hakobyan, A. A., Mamon, G. A., Petrosian, A. R., Kunth, D., & Turatto, M. 2009, A&A, 508, 1259

Hamuy, M. 2003, ApJ, 582, 905

Hamuy, M., Phillips, M. M., Maza, J., Suntzeff, N. B., Schommer, R. A., & Aviles, R. 1995, AJ, 109, 1

Hamuy, M., Phillips, M. M., Suntzeff, N. B., Maza, J., González, L. E., Roth, M., Krisciunas, K., Morrell, N., Green, E. M., Persson, S. E., & McCarthy, P. J. 2003, Nature, 424, 651

Hamuy, M., Phillips, M. M., Suntzeff, N. B., Schommer, R. A., Maza, J., & Aviles, R. 1996a, AJ, 112, 2391

Hamuy, M. & Pinto, P. A. 2002, ApJ, 566, L63

Hamuy, M., Trager, S. C., Pinto, P. A., Phillips, M. M., Schommer, R. A., Ivanov, V., & Suntzeff, N. B. 2000, AJ, 120, 1479

Hamuy, M. et al. 1991, AJ, 102, 208

—. 1993, AJ, 106, 2392

—. 1996b, AJ, 112, 2408

—. 1996c, AJ, 112, 2398

—. 2001, ApJ, 558, 615

—. 2009, ApJ, 703, 1612

Hayden, B. T. et al. 2010a, ArXiv e-prints

—. 2010b, ArXiv:1001.3428

Heger, A., Fryer, C. L., Woosley, S. E., Langer, N., & Hartmann, D. H. 2003, ApJ, 591, 288

Heger, A. & Langer, N. 2000, ApJ, 544, 1016

Hendry, M. A. et al. 2005, MNRAS, 359, 906

—. 2006, MNRAS, 369, 1303

Herant, M., Benz, W., Hix, W. R., Fryer, C. L., & Colgate, S. A. 1994, ApJ, 435, 339

Hicken, M. et al. 2007, ApJ, 669, L17

—. 2009, ApJ, 700, 331

Hirata, K., Kajita, T., Koshiba, M., Nakahata, M., & Oyama, Y. 1987, Physical Review Letters, 58, 1490

Hirschi, R., Meynet, G., & Maeder, A. 2004, A&A, 425, 649

Ho, W. C. G. et al. 2001, PASP, 113, 1349

Hoeflich, P. & Khokhlov, A. 1996, ApJ, 457, 500

Hoeflich, P., Mueller, E., & Khokhlov, A. 1993, A&A, 268, 570

Höflich, P. et al. 2002, ApJ, 568, 791

—. 2010, ApJ, 710, 444

Holtzman, J. A. et al. 2008, AJ, 136, 2306

Holz, D. E. & Linder, E. V. 2005, ApJ, 631, 678

Hopkins, A. M. & Beacom, J. F. 2006, ApJ, 651, 142

Horiuchi, S., Beacom, J. F., Kochanek, C. S., Prieto, J. L., Stanek, K. Z., & Thompson, T. A. 2011, ArXiv e-prints

Howell, D. A. 2001, ApJ, 554, L193

—. 2010, ArXiv e-prints

Howell, D. A., Sullivan, M., Conley, A., & Carlberg, R. 2007, ApJ, 667, L37

Howell, D. A. et al. 2005, ApJ, 634, 1190

—. 2006, Nature, 443, 308

—. 2009, ApJ, 691, 661

Hoyle, F. & Fowler, W. A. 1960, ApJ, 132, 565

Hsiao, E. Y., Conley, A., Howell, D. A., Sullivan, M., Pritchet, C. J., Carlberg, R. G., Nugent, P. E., & Phillips, M. M. 2007, ApJ, 663, 1187

Hunter, D. J. et al. 2009, A&A, 508, 371

Iben, I. & Tutukov, A. V. 1984, ApJS, 54, 335

Isern, J., Canal, R., & Labay, J. 1991, ApJ, 372, L83

Ivezic, Z. et al. 2008, Serbian Astronomical Journal, 176, 1

James, F. & Roos, M. 1975, Comput. Phys. Commun., 10, 343

Janka, H. ., Buras, R., Kitaura Joyanes, F. S., Marek, A., & Rampp, M. 2004, ArXiv Astrophysics e-prints

Janka, H.-T. 2001, A&A, 368, 527

Jeffery, D. J., Leibundgut, B., Kirshner, R. P., Benetti, S., Branch, D., & Sonneborn, G. 1992, ApJ, 397, 304

Jha, S., Riess, A. G., & Kirshner, R. P. 2007, ApJ, 659, 122

Jha, S. et al. 2006, AJ, 131, 527

Johnson, B. D. & Crotts, A. P. S. 2006, AJ, 132, 756

Johnson, H. M. & MacLeod, J. M. 1963, PASP, 75, 123

Jönsson, J. et al. 2010, MNRAS, 405, 535

—. 2011, in preparation

Justham, S. 2011, ApJ, 730, L34+

Kasen, D. 2010, ApJ, 708, 1025

Kasen, D., Röpke, F. K., & Woosley, S. E. 2009, Nature, 460, 869

Kasen, D. & Woosley, S. E. 2009, ApJ, 703, 2205

Kasliwal, M. M. et al. 2008, ApJ, 683, L29

—. 2010, ApJ, 723, L98

Kawabata, K. S. et al. 2010, Nature, 465, 326

Kelly, P. L. et al. 2008, ApJ, 687, 1201

—. 2010, ApJ, 715, 743

Kessler, R. et al. 2009, ApJS, 185, 32

—. 2010a, ApJ, 717, 40

—. 2010b, ArXiv e-prints

Khokhlov, A., Mueller, E., & Hoeflich, P. 1993, A&A, 270, 223

Khokhlov, A. M. 1991, A&A, 245, 114

Kirshner, R. P. & Kwan, J. 1974, ApJ, 193, 27

Kleiser, I. K. W. et al. 2011, ArXiv e-prints

Koshiba, M. 1992, Phys. Rep., 220, 229

Kowalski, M. et al. 2008, ApJ, 686, 749

Krisciunas, K. et al. 2000, ApJ, 539, 658

—. 2001, AJ, 122, 1616

—. 2003, AJ, 125, 166

—. 2004a, AJ, 127, 1664

—. 2004b, AJ, 128, 3034

—. 2004c, AJ, 131, 1639

—. 2007, AJ, 133, 58

—. 2009a, AJ, 137, 34

—. 2009b, AJ, 138, 1584

Kuhlen, M., Woosley, S. E., & Glatzmaier, G. A. 2006, ApJ, 640, 407

Kuznetsova, N. V. & Connolly, B. M. 2007, ApJ, 659, 530

Lair, J. C., Leising, M. D., Milne, P. A., & Williams, G. G. 2006, AJ, 132, 2024

Lampeitl, H. et al. 2010, ApJ, 722, 566

Landolt, A. U. 1992, AJ, 104, 340

Law, N. M. et al. 2009, PASP, 121, 1395

Le Borgne, D. & Rocca-Volmerange, B. 2002, A&A, 386, 446

Le Fèvre, O. et al. 2005, A&A, 439, 845

Leibundgut, B. & Suntzeff, N. B. 2003, in Lecture Notes in Physics, Berlin Springer Verlag, Vol. 598, Supernovae and Gamma-Ray Bursters, ed. K. Weiler, 77–90

Leibundgut, B. et al. 1993, AJ, 105, 301

Leonard, D. C. 2007, ApJ, 670, 1275

Leonard, D. C., Gal-Yam, A., Fox, D. B., Cameron, P. B., Johansson, E. M., Kraus, A. L., Mignant, D. L., & van Dam, M. A. 2008, PASP, 120, 1259

Leonard, D. C., Li, W., Filippenko, A. V., Foley, R. J., & Chornock, R. 2005, ApJ, 632, 450

Leonard, D. C. et al. 2002a, AJ, 124, 2490

—. 2002b, PASP, 114, 35

Li, L.-X. 2008, MNRAS, 388, 1487

Li, W., Filippenko, A. V., Treffers, R. R., Riess, A. G., Hu, J., & Qiu, Y. 2001a, ApJ, 546, 734

Li, W., Jha, S., Filippenko, A. V., Bloom, J. S., Pooley, D., Foley, R. J., & Perley, D. A. 2006a, PASP, 118, 37

Li, W., Van Dyk, S. D., Filippenko, A. V., Cuillandre, J.-C., Jha, S., Bloom, J. S., Riess, A. G., & Livio, M. 2006b, ApJ, 641, 1060

Li, W. et al. 2001b, PASP, 113, 1178

—. 2003, PASP, 115, 453

—. 2010a, accepted to MNRAS

—. 2010b, accepted to MNRAS

Liebendörfer, M., Mezzacappa, A., & Thielemann, F.-K. 2001, Phys.Rev.D, 63, 104003

Lilly, S. J. et al. 2007, ApJS, 172, 70

Lira, P. et al. 1998, AJ, 115, 234

Liu, Q. et al. 2000, A&AS, 144, 219

Livne, E. 1990, ApJ, 354, L53

Livne, E., Asida, S. M., & Höflich, P. 2005, ApJ, 632, 443

Lorén-Aguilar, P., Isern, J., & García-Berro, E. 2009, A&A, 500, 1193

Lyne, A. G. & Lorimer, D. R. 1994, Nature, 369, 127

Lyutikov, M. & Blackman, E. G. 2001, MNRAS, 321, 177

MacFadyen, A. I. & Woosley, S. E. 1999, ApJ, 524, 262

Maeda, K. et al. 2010, ApJ, 712, 624

—. 2011, MNRAS, 413, 3075

Maeder, A. & Meynet, G. 2004, A&A, 422, 225

Maguire, K., Kotak, R., Smartt, S. J., Pastorello, A., Hamuy, M., & Bufano, F. 2010, MNRAS, 403, L11

Malesani, D. et al. 2004, ApJ, 609, L5

Mannucci, F., Della Valle, M., & Panagia, N. 2006, MNRAS, 370, 773

Mannucci, F., Della Valle, M., Panagia, N., Cappellaro, E., Cresci, G., Maiolino, R., Petrosian, A., & Turatto, M. 2005, A&A, 433, 807

Maoz, D. & Badenes, C. 2010, MNRAS, 407, 1314

Maoz, D., Mannucci, F., Li, W., Filippenko, A. V., Valle, M. D., & Panagia, N. 2011, MNRAS, 412, 1508

Maoz, D., Sharon, K., & Gal-Yam, A. 2010, ApJ, 722, 1879

Massey, P. 2003, ARA&A, 41, 15

Matheson, T., Filippenko, A. V., Li, W., Leonard, D. C., & Shields, J. C. 2001, AJ, 121, 1648

Matteucci, F., Panagia, N., Pipino, A., Mannucci, F., Recchi, S., & Della Valle, M. 2006, MNRAS, 372, 265

Mattila, S., Smartt, S. J., Eldridge, J. J., Maund, J. R., Crockett, R. M., & Danziger, I. J. 2008, ApJ, 688, L91

Maund, J. R. & Smartt, S. J. 2005, MNRAS, 360, 288

Mayle, R. & Wilson, J. R. 1988, ApJ, 334, 909

Maza, J. & van den Bergh, S. 1976, ApJ, 204, 519

Mazzali, P. A., Röpke, F. K., Benetti, S., & Hillebrandt, W. 2007, Science, 315, 825

Mazzali, P. A. et al. 2005, ApJ, 623, L37

—. 2006, ApJ, 645, 1323

McClelland, C. M. et al. 2010, ApJ, 720, 704

McKenzie, E. H. & Schaefer, B. E. 1999, PASP, 111, 964

Meikle, W. P. S. et al. 1996, MNRAS, 281, 263

Ménard, B., Kilbinger, M., & Scranton, R. 2010, MNRAS, 406, 1815

Meng, X. C., Chen, W. C., Yang, W. M., & Li, Z. M. 2011, A&A, 525, A129+

Mennekens, N., Vanbeveren, D., De Greve, J. P., & De Donder, E. 2010, A&A, 515, A89+

Mezzacappa, A., Liebendörfer, M., Messer, O. E., Hix, W. R., Thielemann, F.-K., & Bruenn, S. W. 2001, Physical Review Letters, 86, 1935

Millard, J. et al. 1999, ApJ, 527, 746

Miller, A. A. et al. 2009, ApJ, 690, 1303

—. 2010, MNRAS, 404, 305

Minkowski, R. 1941, PASP, 53, 224

Misra, K., Sahu, D. K., Anupama, G. C., & Pandey, K. 2008, MNRAS, 389, 706

Misra, K. et al. 2007, MNRAS, 381, 280

Modjaz, M. 2011, Astronomische Nachrichten, 332, 434

Modjaz, M., Kewley, L., Bloom, J. S., Filippenko, A. V., Perley, D., & Silverman, J. M. 2011, ApJ, 731, L4+

Modjaz, M., Li, W., Filippenko, A. V., King, J. Y., Leonard, D. C., Matheson, T., Treffers, R. R., & Riess, A. G. 2001, PASP, 113, 308

Modjaz, M. et al. 2009, ApJ, 702, 226

Myra, E. S. & Bludman, S. A. 1989, ApJ, 340, 384

Nadyozhin, D. K. 2003, MNRAS, 346, 97

Neill, J. D. et al. 2006, AJ, 132, 1126

—. 2009, ApJ, 707, 1449

—. 2011, ApJ, 727, 15

Newling, J. et al. 2011, MNRAS, 545

Nomoto, K. 1982, ApJ, 253, 798

Nomoto, K. & Iben, I. 1985, ApJ, 297, 531

Nomoto, K., Thielemann, F.-K., & Yokoi, K. 1984, ApJ, 286, 644

Nomoto, K., Yamaoka, H., Shigeyama, T., Kumagai, S., & Tsujimoto, T. 1994, in Supernovae, ed. S. A. Bludman, R. Mochkovitch, & J. Zinn-Justin, 199–+

Nugent, P., Baron, E., Branch, D., Fisher, A., & Hauschildt, P. H. 1997, ApJ, 485, 812

Nugent, P., Branch, D., Baron, E., Fisher, A., Vaughan, T., & Hauschildt, P. H. 1995, Physical Review Letters, 75, 394

Nugent, P., Kim, A., & Perlmutter, S. 2002, PASP, 114, 803

Nugent, P. et al. 2006, ApJ, 645, 841

Olivares, F. 2008, ArXiv e-prints

Pain, R. et al. 1996, ApJ, 473, 356

—. 2002, ApJ, 577, 120

Pakmor, R., Kromer, M., Röpke, F. K., Sim, S. A., Ruiter, A. J., & Hillebrandt, W. 2010, Nature, 463, 61

Palanque-Delabrouille, N. et al. 2010, astro-ph/1005.1890

Panagia, N., Van Dyk, S. D., Weiler, K. W., Sramek, R. A., Stockdale, C. J., & Murata, K. P. 2006, ApJ, 646, 369

Pastorello, A. 2003, PhD thesis, Universitta degli Studi di Padova. Dipartimento di Astronomia

Pastorello, A. et al. 2004, MNRAS, 347, 74

—. 2005, MNRAS, 360, 950

—. 2007a, Nature, 447, 829

—. 2007b, MNRAS, 377, 1531

—. 2007c, MNRAS, 376, 1301

—. 2008a, MNRAS, 389, 131

—. 2008b, MNRAS, 389, 113

—. 2008c, MNRAS, 389, 955

—. 2009a, A&A, 500, 1013

—. 2009b, MNRAS, 394, 2266

—. 2010, ApJ, 724, L16

Patat, F. et al. 2001, ApJ, 555, 900

Pennypacker, C. R. et al. 1989, AJ, 97, 186

Perets, H. B. et al. 2010, Nature, 465, 322

Perlmutter, S. et al. 1997, ApJ, 483, 565

—. 1999, ApJ, 517, 565

Perrett, K. et al. 2010, AJ, 140, 518

—. 2011, in preparation

Phillips, M. M. 1993, ApJ, 413, L105

Phillips, M. M., Lira, P., Suntzeff, N. B., Schommer, R. A., Hamuy, M., & Maza, J. . 1999, AJ, 118, 1766

Phillips, M. M. et al. 1987, PASP, 99, 592

—. 1992, AJ, 103, 1632

—. 2007, PASP, 119, 360

Pian, E. et al. 2006, Nature, 442, 1011

Pignata, G., Maza, J., Hamuy, M., Antezana, R., & Gonzales, L. 2009, in Revista Mexicana de Astronomia y Astrofisica, vol. 27, Vol. 35, Revista Mexicana de Astronomia y Astrofisica Conference Series, 317–+

Pignata, G. et al. 2004, MNRAS, 355, 178

—. 2008, MNRAS, 388, 971

—. 2011, ApJ, 728, 14

Podsiadlowski, P., Joss, P. C., & Hsu, J. J. L. 1992, ApJ, 391, 246

Podsiadlowski, P., Langer, N., Poelarends, A. J. T., Rappaport, S., Heger, A., & Pfahl, E. 2004a, ApJ, 612, 1044

Podsiadlowski, P., Mazzali, P. A., Nomoto, K., Lazzati, D., & Cappellaro, E. 2004b, ApJ, 607, L17

Portegies Zwart, S. F., McMillan, S. L. W., & Gieles, M. 2010, ARA&A, 48, 431

Poznanski, D., Gal-Yam, A., Maoz, D., Filippenko, A. V., Leonard, D. C., & Matheson, T. 2002, PASP, 114, 833

Poznanski, D., Maoz, D., & Gal-Yam, A. 2007, AJ, 134, 1285

Poznanski, D. et al. 2009, ApJ, 694, 1067

—. 2010, Science, 327, 58

Pozzo, M. et al. 2006, MNRAS, 368, 1169

Prieto, J. L., Sellgren, K., Thompson, T. A., & Kochanek, C. S. 2009, ApJ, 705, 1425

Prieto, J. L. et al. 2008, ApJ, 673, 999

Pritchet, C. J., Howell, D. A., & Sullivan, M. 2008, ApJ, 683, L25

Rappaport, S., Di Stefano, R., & Smith, J. D. 1994, ApJ, 426, 692

Raskin, C., Scannapieco, E., Rhoads, J., & Della Valle, M. 2009a, ApJ, 707, 74

Raskin, C., Timmes, F. X., Scannapieco, E., Diehl, S., & Fryer, C. 2009b, MNRAS, 399, L156

Rau, A. et al. 2009, PASP, 121, 1334

Richards, J. W., Homrighausen, D., Freeman, P. E., Schafer, C. M., & Poznanski, D. 2011, ArXiv e-prints

Richardson, D., Branch, D., Casebeer, D., Millard, J., Thomas, R. C., & Baron, E. 2002, AJ, 123, 745

Richmond, M. W. et al. 1995, AJ, 109, 2121

Riess, A. G., Press, W. H., & Kirshner, R. P. 1996, ApJ, 473, 88

Riess, A. G. et al. 1998, AJ, 116, 1009

—. 1999a, AJ, 117, 707

—. 1999b, AJ, 118, 2675

—. 2004, ApJ, 607, 665

—. 2005, ApJ, 627, 579

Rodney, S. A. & Tonry, J. L. 2009, ApJ, 707, 1064

Roepke, F. K. et al. 2010, ArXiv e-prints

Roming, P. W. A. et al. 2009, ApJ, 704, L118

Rosswog, S., Kasen, D., Guillochon, J., & Ramirez-Ruiz, E. 2009, ApJ, 705, L128

Roy, R. et al. 2011, ArXiv e-prints

Ruiz-Lapuente, P., Cappellaro, E., Turatto, M., Gouiffes, C., Danziger, I. J., della Valle, M., & Lucy, L. B. 1992, ApJ, 387, L33

Sadakane, K. et al. 1996, PASJ, 48, 51

Sahu, D. K., Gurugubelli, U. K., Anupama, G. C., & Nomoto, K. 2011, ArXiv e-prints

Sahu, D. K. et al. 2006, MNRAS, 372, 1315

Saio, H. & Nomoto, K. 1985, A&A, 150, L21

Salpeter, E. E. 1955, ApJ, 121, 161

Scalzo, R. A. et al. 2010, ApJ, 713, 1073

Scannapieco, E. & Bildsten, L. 2005, ApJ, 629, L85

Schawinski, K. 2009, MNRAS, 397, 717

Schlegel, D. J., Finkbeiner, D. P., & Davis, M. 1998, ApJ, 500, 525

Schlegel, E. M. 1990, MNRAS, 244, 269

Schmidt, B. P., Keller, S. C., Francis, P. J., & Bessell, M. S. 2005, in Bulletin of the American Astronomical Society, Vol. 37, American Astronomical Society Meeting Abstracts #206, 457–+

Schmidt, B. P. et al. 1993, AJ, 105, 2236

—. 1994a, ApJ, 432, 42

—. 1994b, AJ, 107, 1444

Schwarz, G. E. 1978, Annals of Statistics, 6, 461

Shen, K. J., Kasen, D., Weinberg, N. N., Bildsten, L., & Scannapieco, E. 2010, ApJ, 715, 767

Shigeyama, T. et al. 1992, ApJ, 386, L13

Sim, S. A., Röpke, F. K., Hillebrandt, W., Kromer, M., Pakmor, R., Fink, M., Ruiter, A. J., & Seitenzahl, I. R. 2010, ApJ, 714, L52

Smartt, S. J. 2009, ARA&A, 47, 63

Smartt, S. J., Eldridge, J. J., Crockett, R. M., & Maund, J. R. 2009, MNRAS, 395, 1409

Smartt, S. J., Maund, J. R., Hendry, M. A., Tout, C. A., Gilmore, G. F., Mattila, S., & Benn, C. R. 2004, Science, 303, 499

Smith, J. A. et al. 2002, AJ, 123, 2121

Smith, N. et al. 2009, ApJ, 697, L49

Sollerman, J., Cumming, R. J., & Lundqvist, P. 1998, ApJ, 493, 933

Sollerman, J. et al. 2000, ApJ, 537, L127

Sollerman, J. et al. 2006, A&A, 454, 503

Spyromilio, J., Meikle, W. P. S., Allen, D. A., & Graham, J. R. 1992, MNRAS, 258, 53P

Stanishev, V. et al. 2007, A&A, 469, 45

Stoll, R., Prieto, J. L., Stanek, K. Z., Pogge, R. W., Szczygiel, D. M., Pojmanski, G., Antognini, J., & Yan, H. 2010, ArXiv e-prints

Stritzinger, M., Mazzali, P. A., Sollerman, J., & Benetti, S. 2006, A&A, 460, 793

Stritzinger, M. et al. 2002, AJ, 124, 2100

Strolger, L., Dahlen, T., & Riess, A. G. 2010, ApJ, 713, 32

Strolger, L. et al. 2002, AJ, 124, 2905

Strolger, L.-G. et al. 2004, ApJ, 613, 200

Strovink, M. 2007, ApJ, 671, 1084

Sullivan, M. et al. 2006a, AJ, 131, 960

—. 2006b, ApJ, 648, 868

—. 2009, ApJ, 693, L76

—. 2010, MNRAS, 406, 782

—. 2011a, ArXiv e-prints

—. 2011b, ApJ, 732, 118

Suntzeff, N. B. et al. 1999, AJ, 117, 1175

Taubenberger, S. et al. 2006, MNRAS, 371, 1459

—. 2008, MNRAS, 385, 75

Taylor, J. 1997, Introduction to Error Analysis, the Study of Uncertainties in Physical Measurements, 2nd Edition, ed. Taylor, J. (University Science Books)

Timmes, F. X., Brown, E. F., & Truran, J. W. 2003, ApJ, 590, L83

Tominaga, N., Blinnikov, S., Baklanov, P., Morokuma, T., Nomoto, K., & Suzuki, T. 2009, ApJ, 705, L10

Tonry, J. & Pan-STARRS Team. 2005, in Bulletin of the American Astronomical Society, Vol. 37, American Astronomical Society Meeting Abstracts, 121.01–+

Totani, T., Morokuma, T., Oda, T., Doi, M., & Yasuda, N. 2008, PASJ, 60, 1327

Tremonti, C. A. et al. 2004, ApJ, 613, 898

Tripp, R. 1998, A&A, 331, 815

Trundle, C. et al. 2009, A&A, 504, 945

Truran, J. W., Arnett, W. D., & Cameron, A. G. W. 1967, Canadian Journal of Physics, 45, 2315

Tsvetkov, D. Y. 1994, Astronomy Letters, 20, 374

—. 2006a, Peremennye Zvezdy, 26, 3

—. 2006b, Peremennye Zvezdy, 26, 4

—. 2008, Peremennye Zvezdy, 28, 3

Tsvetkov, D. Y., Blinnikov, S. I., & Pavlyuk, N. N. 2001, ArXiv Astrophysics e-prints

Tsvetkov, D. Y., Goranskij, V., & Pavlyuk, N. 2008, Peremennye Zvezdy, 28, 8

Tsvetkov, D. Y. et al. 2006, A&A, 460, 769

—. 2007, Peremennye Zvezdy, 27, 5

—. 2009, Peremennye Zvezdy, 29, 2

Turatto, M., Benetti, S., Cappellaro, E., Danziger, I. J., Della Valle, M., Gouiffes, C., Mazzali, P. A., & Patat, F. 1996, MNRAS, 283, 1

Turatto, M., Piemonte, A., Benetti, S., Cappellaro, E., Mazzali, P. A., Danziger, I. J., & Patat, F. 1998, AJ, 116, 2431

Turatto, M. et al. 1993, MNRAS, 265, 471

—. 2000, ApJ, 534, L57

Tutukov, A. V. & Yungelson, L. R. 1994, MNRAS, 268, 871

Utrobin, V. P. & Chugai, N. N. 2009, A&A, 506, 829

Valenti, S. et al. 2008, MNRAS, 383, 1485

Valentini, G. et al. 2003, ApJ, 595, 779

van Dyk, S. D., Hamuy, M., & Filippenko, A. V. 1996, AJ, 111, 2017

Van Dyk, S. D., Li, W., & Filippenko, A. V. 2003, PASP, 115, 1289

Van Dyk, S. D. et al. 2000, PASP, 112, 1532

—. 2010, astro-ph/1011.5873

van Kerkwijk, M. H., Chang, P., & Justham, S. 2010, ApJ, 722, L157

Vinkó, J. et al. 2006, MNRAS, 369, 1780

Walker, E. S. et al. 2010, accepted to MNRAS

Wang, L. 2005, ApJ, 635, L33

Wang, L., Wheeler, J. C., & Höflich, P. 1997, ApJ, 476, L27+

Wang, X. et al. 2009a, ApJ, 699, L139

—. 2009b, ApJ, 697, 380

Webbink, R. F. 1984, ApJ, 277, 355

Wheeler, J. C., Yi, I., Höflich, P., & Wang, L. 2000, ApJ, 537, 810

Whelan, J. & Iben, I. J. 1973, ApJ, 186, 1007

Wilson, J. R., Mayle, R., Woosley, S. E., & Weaver, T. 1986, Annals of the New York Academy of Sciences, 470, 267

Wilson, J. R. & Mayle, R. W. 1988, Phys. Rep., 163, 63

Winzer, J. E. 1974, JRASC, 68, 36

Wood, R. & Andrews, P. J. 1974, MNRAS, 167, 13

Wood-Vasey, W. M. et al. 2008, ApJ, 689, 377

Wooden, D. H., Rank, D. M., Bregman, J. D., Witteborn, F. C., Tielens, A. G. G. M., Cohen, M., Pinto, P. A., & Axelrod, T. S. 1993, ApJS, 88, 477

Woosley, S. E. 1993, ApJ, 405, 273

Woosley, S. E. & Bloom, J. S. 2006, ARA&A, 44, 507

Woosley, S. E., Heger, A., & Weaver, T. A. 2002, Reviews of Modern Physics, 74, 1015

Woosley, S. E., Langer, N., & Weaver, T. A. 1993, ApJ, 411, 823

Woosley, S. E. & Weaver, T. A. 1986, ARA&A, 24, 205

—. 1994, ApJ, 423, 371

Yamaoka, H. et al. 1992, ApJ, 393, L55

Yasuda, N. & Fukugita, M. 2010, AJ, 139, 39

Yoon, S.-C. & Langer, N. 2005, A&A, 435, 967

Yoon, S.-C., Podsiadlowski, P., & Rosswog, S. 2007, MNRAS, 380, 933

Yoshii, Y. et al. 2003, ApJ, 592, 467

Young, D. R. et al. 2010, A&A, 512, A70+

Yu, B., Yang, G.-L., & Lu, T. 2009, ArXiv e-prints

Yuan, F. et al. 2010, ApJ, 715, 1338

Yüksel, H., Kistler, M. D., Beacom, J. F., & Hopkins, A. M. 2008, ApJ, 683, L5

Yungelson, L. R. & Livio, M. 2000, ApJ, 528, 108

Zhang, T. et al. 2006, AJ, 131, 2245